USGS
science for a changing world

Modeling the Dynamics of Lahars that Originate as Landslides on the West Side of Mount Rainier, Washington

Open-File Report 2021–1118

U.S. Department of the Interior
U.S. Geological Survey

Cover. Photograph showing the city of Orting, Washington, in the foreground and the northwest flank of Mount Rainier in the distance. Orting is one of many communities that are located in lahar-prone areas surrounding Mount Rainier. U.S. Geological Survey photograph by Ed Ruttledge, January 18, 2014.

Modeling the Dynamics of Lahars that Originate as Landslides on the West Side of Mount Rainier, Washington

By David L. George, Richard M. Iverson, and Charles M. Cannon

Open-File Report 2021–1118

U.S. Department of the Interior
U.S. Geological Survey

U.S. Geological Survey, Reston, Virginia: 2022

For more information on the USGS—the Federal source for science about the Earth, its natural and living resources, natural hazards, and the environment—visit https://www.usgs.gov or call 1–888–ASK–USGS.

For an overview of USGS information products, including maps, imagery, and publications, visit https://store.usgs.gov.

Suggested citation:
George, D.L., Iverson, R.M., and Cannon, C.M., 2022, Modeling the dynamics of lahars that originate as landslides on the west side of Mount Rainier, Washington: U.S. Geological Survey Open-File Report 2021–1118, 54 p., https://doi.org/10.3133/ofr20211118.

ISSN 2331-1258 (online)

Contents

Abstract 1
Introduction 1
Prehistoric Lahars at Mount Rainier 4
    The Osceola Mudflow and Paradise Lahar 4
    Round Pass and Electron Mudflows 4
The D-Claw Numerical Model 6
Mount Rainier Base Topography and Landslide Source Areas 8
    Digital Elevation Models 8
    Source Areas and Failure Surfaces 8
    Hypothetical Lahars Originating on the West Side of Mount Rainier 11
Simulation Results 11
    Hypothetical Worst-Case Scenarios 11
        S-260-HM Landslide and Lahar Inundation of the Puyallup River Valley 11
        T-260-HM Landslide and Lahar Inundation of the Nisqually River and Alder Lake 12
    Lahars of Smaller Volume and Lower Mobility 29
        Low-Mobility 260 Mm^3 Lahars 29
        High-Mobility 52 Mm^3 Lahars 29
        Low-Mobility 52 Mm^3 Lahars 29
    Lahar Speeds, Depths, and Discharges at Selected Locations 37
        S-260-HM Simulation 37
        T-260-HM Simulation 38
        Comparison of Lahars at Selected Locations 38
Discussion 52
Final Remarks 52
Acknowledgments 53
References Cited 53

Figures

1. Shaded relief map of Mount Rainier, Washington, and the surrounding area....2
2. Oblique Google Earth view of Mount Rainier's west flank and the Puyallup and Nisqually River valleys....3
3. Oblique shaded relief view of Mount Rainier's upper west side showing major topographic features....3
4. Shaded relief map of Mount Rainier indicating the relative slope stability of different areas by their factor of safety....4
5. Shaded relief map of Mount Rainier and the surrounding area showing Holocene lahar paths....5
6. Oblique shaded relief views of Mount Rainier's upper west side showing hypothetical source models for 260 million cubic meter landslides....9
7. Shaded relief map of Mount Rainier showing the locations of river basin divides and glaciers below the Sunset Amphitheater and the Tahoma Glacier headwall....10
8. Shaded relief maps showing landslide and lahar flow depths of the S-260-HM simulation just before the onset of slope failure and at the simulation's final computed time....13
9. Close-up oblique views of Mount Rainier's west side showing landslide and lahar flow depths of the S-260-HM simulation at selected times during the first 2 minutes of lahar motion....14
10. Shaded relief maps showing landslide and lahar flow depths of the S-260-HM simulation at selected times during the first 30 minutes of lahar motion....15
11. Shaded relief maps showing landslide and lahar flow depths of the S-260-HM simulation at selected times during the first 8 hours of lahar motion....16
12. Shaded relief maps showing lahar flow depths of the S-260-HM simulation at selected times, focused on the valley bottom surrounding Orting....17
13. Map showing maximum depths of lahar inundation in Orting and the surrounding valley....18
14. Shaded relief maps showing lahar flow depths of the S-260-HM simulation at selected times ≥1 hour, focused on the Puyallup River valley between Orting and the Port of Tacoma....19
15. Shaded relief maps showing landslide and lahar flow depths of the T-260-HM simulation just before the onset of slope failure and at the simulation's final computed time....20
16. Close-up oblique views of Mount Rainier's west side showing landslide and lahar flow depths of the T-260-HM simulation at selected times during the first 2 minutes of lahar motion....21
17. Shaded relief maps showing landslide and lahar flow depths of the T-260-HM simulation at selected times during the first 30 minutes of lahar motion....22
18. Shaded relief maps showing landslide and lahar flow depths of the T-260-HM simulation at selected times during the first 2 hours of lahar motion....23
19. Photograph showing Alder Dam, a 100-meter-high concrete dam on the Nisqually River, 40 kilometers downstream from Mount Rainier's summit....24
20. Oblique views of the T-260-HM simulation at selected times showing the lahar approaching and entering Alder Lake reservoir....25
21. Shaded relief maps showing solid volume fractions of the T-260-HM simulation at selected times as the lahar enters Alder Lake reservoir and mixes with lake water....26

22. Shaded relief maps showing surface elevations of the T-260-HM simulation at selected times as the lahar enters Alder Lake reservoir and causes water levels to rise 27
23. Oblique views of the T-260-HM simulation at selected times showing water surface elevations relative to the undisturbed lake surface elevation as a swell of lahar-displaced water approaches and eventually overtops Alder Dam....28
24. Shaded relief maps showing landslide and lahar flow depths of the S-260-LM simulation at selected times 30
25. Shaded relief maps showing landslide and lahar flow depths of the T-260-LM simulation at selected times 31
26. Close-up oblique views of Mount Rainier's upper west side showing landslide and lahar flow depths of the small-volume, high-mobility lahar simulations S-52-HM and T-52-HM before and 20 seconds after the onset of slope failure 32
27. Shaded relief maps showing landslide and lahar flow depths of the S-52-HM simulation at selected times for the full spatial extent of the simulation and focused on the valley bottom surrounding Orting 33
28. Shaded relief maps showing landslide and lahar flow depths of the T-52-HM simulation at selected times for the full spatial extent of the simulation and focused on the valley bottom surrounding Orting 34
29. Shaded relief maps showing landslide and lahar flow depths of the S-52-LM simulation at selected times 35
30. Shaded relief maps showing landslide and lahar flow depths of the T-52-LM simulation at selected times 36
31. Shaded relief map of Mount Rainier and the surrounding area showing the location of time series output gauges and cross-flow transects....39
32. Graphs of time series output for the S-260-HM simulation lahar showing total flow discharge and total flow volume in the Puyallup and Nisqually River valleys 40
33. Graphs of time series output for the S-260-HM simulation showing the evolution of lahar flow dynamics at gauges 1–3 in the Puyallup River and Mowich River valleys 41
34. Graph of time series output for the S-260-HM simulation showing the evolution of lahar flow dynamics at gauges 5–7, located near the communities of Orting, Sumner, and Puyallup in the Puyallup River valley 42
35. Graphs of time series output for the T-260-HM simulation lahar showing total flow discharge and total flow volume in the Puyallup and Nisqually River valleys 43
36. Graphs of time series output for the T-260-HM simulation showing the evolution of lahar flow dynamics at gauge 4, located on the Nisqually River upstream of Alder Lake, near Ashford....44
37. Graph of time series output for the T-260-HM simulation showing the water surface elevation in meters (m) at gauge 8, located in Alder Lake just upstream from Alder Dam 45
38. Graphs of time series output for the T-260-HM simulation lahar comparing the total discharge and total volume of flow through transect Γ_{Alder} at the head of Alder Lake to the total discharge and total volume of flow through transects $\Gamma_{AboveDam}$ and $\Gamma_{BelowDam}$, located just above and below Alder Dam....46
39. Graphs of time series output for the T-260-HM simulation lahar showing total flow discharge and total flow volume above and below Alder Dam 47
40. Graphs of time series output for the two worst-case scenario simulations T-260-HM and S-260-HM showing total flow discharge and total flow volume of the simulated lahars in the Puyallup River valley at gauge 3 48

41. Graphs of time series output for the two worst-case scenario simulations T-260-HM and S-260-HM showing total flow discharge and total flow volume of the simulated lahars in the Nisqually River valley at gauge 4 49
42. Graphs of time series output for the four high-mobility lahar simulations showing comparisons of lahar flow dynamics at gauge 3 on the Puyallup River 50
43. Graphs of time series output for the four high-mobility lahar simulations showing comparisons of lahar flow dynamics at gauge 5 near Orting 51

Tables

1. Material parameters of lahars used in D-Claw model simulations 6
2. Parameters of different grid levels of adaptive mesh refinement 7
3. Source locations, volumes, and initial source material permeabilities for the eight landslide-generated lahar scenarios considered in this report 10
4. Gauge locations for time series output 37
5. Cross-flow transect locations for time series output 37

Conversion Factors

International System of Units to U.S. customary units

Multiply	By	To obtain
	Length	
meter (m)	3.281	foot (ft)
kilometer (km)	0.6214	mile (mi)
meter (m)	1.094	yard (yd)
	Area	
square meter (m^2)	0.0002471	acre
square kilometer (km^2)	247.1	acre
square centimeter (cm^2)	0.001076	square foot (ft^2)
square meter (m^2)	10.76	square foot (ft^2)
square centimeter (cm^2)	0.1550	square inch (ft^2)
square kilometer (km^2)	0.3861	square mile (mi^2)
	Volume	
cubic meter (m^3)	6.290	barrel (petroleum, 1 barrel = 42 gal)
cubic meter (m^3)	35.31	cubic foot (ft^3)
cubic meter (m^3)	1.308	cubic yard (yd^3)
cubic meter (m^3)	0.0008107	acre-foot (acre-ft)

Abbreviations

3D	three dimensional
AMR	adaptive mesh refinement
DEM	digital elevation model
GPS	Global Positioning System
HM	high-mobility
LM	low-mobility
NED	National Elevation Dataset

Modeling the Dynamics of Lahars that Originate as Landslides on the West Side of Mount Rainier, Washington

By David L. George, Richard M. Iverson, and Charles M. Cannon

Abstract

Large lahars pose substantial threats to people and property downstream from Mount Rainier volcano in Washington State. Geologic evidence indicates that these threats exist even during the absence of volcanic activity and that the threats are highest in the densely populated Puyallup and Nisqually River valleys on the west side of the volcano. However, the precise character of these threats can be difficult to anticipate.

To help predict depths and rates of possible lahar inundation in the area, this report presents the results of simulations of hypothetical future lahars that originate high on the west side of Mount Rainier and travel downstream into the Puyallup and Nisqually River valleys. Many of the results portrayed as still images in the figures of this report are also available as animated files that can be accessed at the web address provided in the figure captions. We simulated eight scenarios, including worst-case scenarios in which the simulated lahars are similar in size and mobility to the approximately 260 million cubic meter (Mm^3; 340 million cubic yard) Electron Mudflow lahar that descended from Mount Rainier and inundated the Puyallup River valley about 500 years ago. The other six scenarios place the worst-case scenarios in perspective by simulating lahars that originate from the same source areas but have smaller volumes or lesser mobilities.

We perform our simulations using an open-source software package that we developed called D-Claw. The numerical model composing the kernel of D-Claw solves a system of five hyperbolic partial differential equations that describe the depth-averaged dynamics of static or flowing grain-fluid mixtures interacting with three-dimensional topography. In D-Claw, the volume fraction occupied by solid grains is a dependent variable that can freely evolve, enabling simulation of landslide liquefaction and of lahar interaction with static bodies of water. The latter feature facilitates a seamless simulation of a lahar in the Nisqually River valley entering Alder Lake reservoir.

In the event of an approximately 260 Mm^3 high-mobility lahar originating on the west side of Mount Rainier, our results point to two areas of pronounced hazard. One area, comprising the densely populated lowlands of Orting, Washington, and environs, could be inundated by lahars originating from either the Sunset Amphitheater or Tahoma Glacier headwall areas. In the worst-case scenario we consider for the Orting lowlands, which involves a 260 Mm^3 high-mobility lahar originating from a landslide in the Sunset Amphitheater, a flow front approximately 4 meters deep and traveling about 4 meters per second reaches the Orting lowlands about 1 hour after the onset of slope failure. After passing through the Orting lowlands, the simulated lahar slows down and comes to rest in the valleys surrounding Sumner and Puyallup. A second area of pronounced hazard is the stretch of the Nisqually River valley beginning in Mount Rainier National Park and extending downstream to Alder Lake reservoir and Alder Dam. This area would be substantially affected in the worst-case scenario that involves a 260 Mm^3 high-mobility lahar originating from the Tahoma Glacier headwall area—the locality identified by a previous study as the sector of Mount Rainier most prone to large-scale gravitational collapse. The simulated lahar passes through the area of Ashford, Washington, within about 20 minutes of the onset of slope failure and reaches the head of Alder Lake within about 50 minutes. The lahar ultimately displaces enough reservoir water to cause overtopping of the 100 meter (330 foot) tall Alder Dam, but consequences of such dam overtopping are not addressed in this report.

Introduction

Lahars pose substantial geologic hazards in river valleys that head on the sides of Mount Rainier volcano in Washington State (figs. 1 and 2). The scope of the hazards has been established through geologic studies of the deposits of large prehistoric lahars that have inundated most of these valleys (Crandell and Waldron, 1956; Crandell, 1971; Scott and others, 1995; Vallance and Scott, 1997; Hoblitt and others, 1998). Mapping of the deposits has also provided the foundation for a statistically based assessment of areas that might be inundated by future lahars that originate on Mount Rainier, using a computer code called LAHARZ (Iverson and others, 1998; Schilling, 1998). However, the LAHARZ method of hazard assessment has limitations. It provides no information about lahar travel times or the sensitive dependence of lahar behavior on source-area locations and downstream terrain features, including infrastructure such as dams, reservoirs, and roads. These limitations can be overcome—at least in part—by advanced computational modeling of lahar dynamics.

Base modified from U.S. Geological Survey National Elevation Dataset, 1/3 arc-second resolution and 1:24,000 scale
The National Map vector digital data, various dates
City boundaries (darker shaded areas) from Washington Department of Transportation, 2017
Universal Transverse Mercator Zone 10 projection, North American Datum of 1983

Figure 1. Shaded relief map of Mount Rainier, Washington, and the surrounding area, including the Puyallup and Nisqually River valleys and part of the Puget Sound. Hypothetical landslide initiation area indicates the source area of lahars modeled in this report.

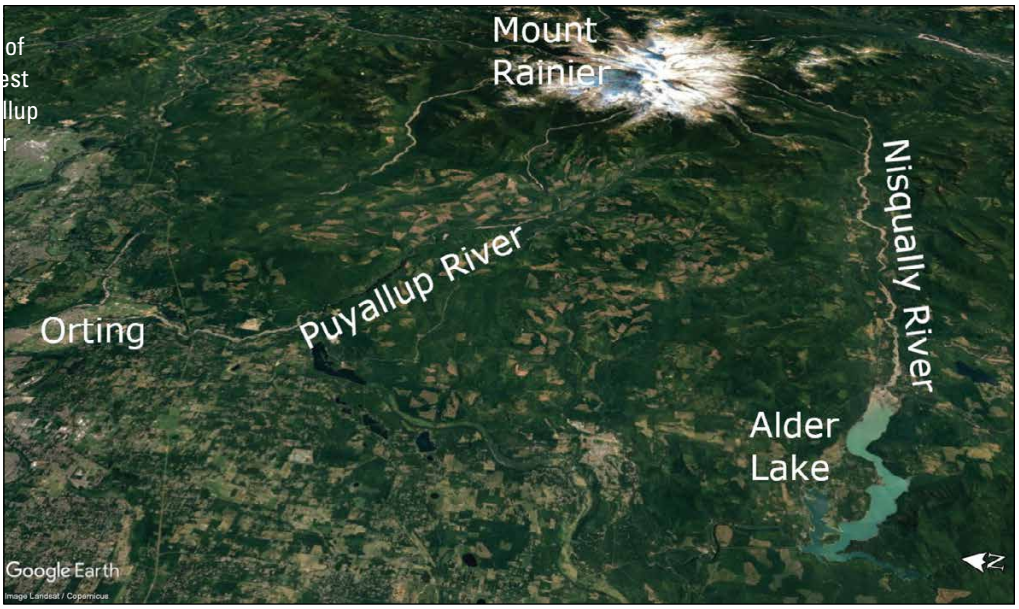

Figure 2. Oblique Google Earth view of Mount Rainier's west flank and the Puyallup and Nisqually River valleys.

This report summarizes the results of high-resolution computational modeling of the dynamics of prospective large lahars that originate as landslides high on the west side of Mount Rainier. This sector of Mount Rainier encompasses the Sunset Amphitheater and Tahoma Glacier headwall (fig. 3), and it has been identified as the part of the volcano that is most susceptible to large-scale gravitational failure because of its steep terrain and weak rock (fig. 4; Reid and others, 2001; Finn and others, 2001). Lahars that originate from this area can follow diverse paths as they interact with complex terrain, but, ultimately, they funnel into the lowland valleys of the Puyallup and Nisqually Rivers (fig. 1). The model results presented in this report consider eight scenarios in which large landslides on Mount Rainier transform into lahars that descend into these valleys. The results provide information about lahar travel times as well as information about inundation patterns, depths, and lahar interactions with crucial infrastructure such as Alder Lake reservoir.

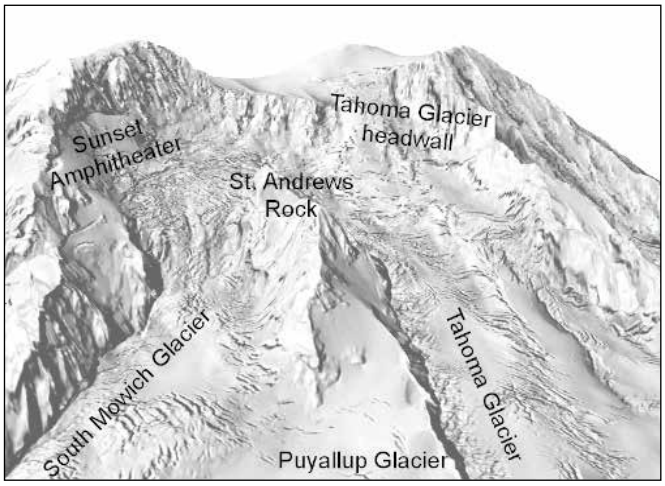

Figure 3. Oblique shaded relief view of Mount Rainier's upper west side showing major topographic features.

Lahars that begin as landslides can occur without warning—that is, without any precursory activity detectable by seismometers or other instruments. A recent example of such an unheralded lahar occurred on August 6, 2010, at Mount Meager volcano, in an uninhabited area approximately 150 kilometers (km) north of Vancouver, British Columbia (Guthrie and others, 2012). The lahar began as a landslide that displaced approximately 50 million cubic meters (Mm^3; 65 million cubic yards) of rock and ice from the volcano's south side (Roberti and others, 2017). Liquefaction of part of the moving landslide then produced a lahar that reached maximum speeds estimated to be greater than 80 meters per second (m/s) (~180 miles per hour [mi/hr]) (Allstadt, 2013). Less than 10 minutes after its onset, the lahar had probably begun to inundate a broad swath of the Lillooet River floodplain approximately 12 km (7.5 miles [mi]) away (Moretti and others, 2015). The potential effects of analogous events at Mount Rainier, where densely populated areas are in the lahar path, are considered in this report.

This report does not provide a forecast of anticipated events at Mount Rainier, but rather an assessment of potential downslope and downstream dynamics given presupposed initial slope failures and lahar attributes. The hypothetical landslide sources derived in this study, though qualitatively informed by geologic and mechanical considerations of Mount Rainier's edifice, are not deemed imminent or likely, and cannot be assessed probabilistically. Any probabilistic forecast based on potential landslide source geometries, occurring naturally and failing spontaneously or by unforeseen triggers, would be questionable given the large number of uncertainties involved.

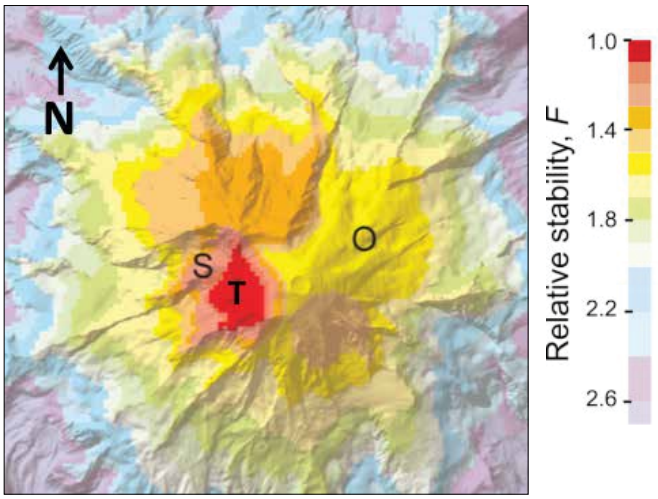

Figure 4. Shaded relief map of Mount Rainier (modified from Reid and others, 2001) indicating the relative slope stability of different areas by their factor of safety, *F*. Low factors of safety denote the most unstable areas, which are shaded red. We considered hypothetical landslide source volumes on the western face of Mount Rainier within the Sunset Amphitheater (S) and Tahoma Glacier headwall (T). The source region of the 5,600-year-old Osceola Mudflow is indicated with an "O."

Prehistoric Lahars at Mount Rainier

We provide here a brief account of several notable lahars that occurred within the last 6,000 years to provide context for our simulated scenarios. These lahars resulted from edifice failures (in other words, gravity-driven collapses of weak rock) or large debris avalanches originating near Mount Rainier's summit. Lahars may also be generated from water or sediment-laden flows that transform into debris flows when entrainment of additional sediment occurs, but these types of lahars are not the focus of this study. A more comprehensive geologic overview of Mount Rainier lahars can be obtained from prior reports on the subject, including, for example, Crandell and Waldron (1956), Crandell (1971), Scott and others (1995), Vallance and Scott (1997), and Hoblitt and others (1998).

The Osceola Mudflow and Paradise Lahar

About 5,600 years ago, the enormous Osceola Mudflow buried the river valleys and Puget Sound lowlands north of Mount Rainier—in some places to depths exceeding 100 m—under extensive deposits that today cover more than 200 square kilometers (km^2). With a volume of about 3.8 cubic kilometers (km^3), the Osceola Mudflow is one of the world's largest known lahars (Crandell, 1971; Scott and others, 1995; Vallance and Scott, 1997). The lahar traveled along the White River drainage (fig. 5) and likely originated from a collapse of the east-northeast side of Mount Rainier coinciding with eruptive activity. In addition to its exceptionally large volume, the Osceola Mudflow had a high clay content (Vallance and Scott, 1997), which probably enhanced its mobility.

Contemporaneous with the Osceola Mudflow, with likely related origins, the smaller (50–100 Mm^3) Paradise lahar traveled into the Nisqually River valley, southwest of Mount Rainier's summit (fig. 5) (Vallance and Scott, 1997). Although the lahar buried valleys to exceptionally large depths (~300 m), it attenuated quickly on the low-gradient Nisqually River valley floor, leaving observed deposits no farther downstream than Ashford. The lahar most likely traveled farther toward Alder Lake, but no deposits are preserved there, and its distal extent is uncertain. Both the Osceola Mudflow and Paradise lahars had origins in hydrothermally altered rock, and both had relatively high clay contents. However, the Paradise lahar likely originated from less altered rock and had lower clay content, possibly contributing to its lesser intrinsic mobility and rapid attenuation (Vallance and Scott, 1997).

The eruptive activity and debris avalanches associated with the Osceola Mudflow and Paradise lahar removed Mount Rainier's summit and much of the hydrothermally altered core of the volcano, excavating a large crater near the east summit (Crandell, 1971; Vallance and Scott, 1997; Finn and others, 2001; Reid and others, 2001; Sisson and Vallance, 2009). The summit has since been replaced with a new cone and the crater filled by younger lava flows. This has contributed to a scientific consensus that the east summit of Mount Rainier is unlikely to produce large edifice failures or debris avalanches capable of generating large lahars like those considered in this report (Finn and others, 2001; Reid and others, 2001; Sisson and Vallance, 2009).

Round Pass and Electron Mudflows

The largest volumes of hydrothermally altered rock remaining on Mount Rainier are located on its west side (Finn and others, 2001; Reid and others, 2001; Sisson and Vallance, 2009). Moreover, large edifice failures and subsequent lahars have originated from the west side of the volcano and travelled into the Puyallup River valley to the west-northwest and Nisqually River valley to the west-southwest. The Round Pass Mudflow, which occurred about 2,600 years ago, originated from a collapse of hydrothermally altered rock near Sunset Amphitheater and the Tahoma Glacier headwall below the west summit of the volcano (fig. 3), producing lahars in both the Puyallup River and Nisqually River valleys (Scott and others, 1995). The Nisqually River branch appears to have attenuated quickly downstream of the Tahoma Creek tributary, leaving distal deposits near its mouth. The Puyallup River branch of the lahar appears to have been more mobile, leaving deposits greater than 30 km downstream from its source. Like the lahars described above, the Round Pass Mudflow coincided with eruptive activity that most likely contributed to its generation (Sisson and Vallance, 2009).

The most recent large lahar at Mount Rainier, the Electron Mudflow, occurred about 500 years ago and had a

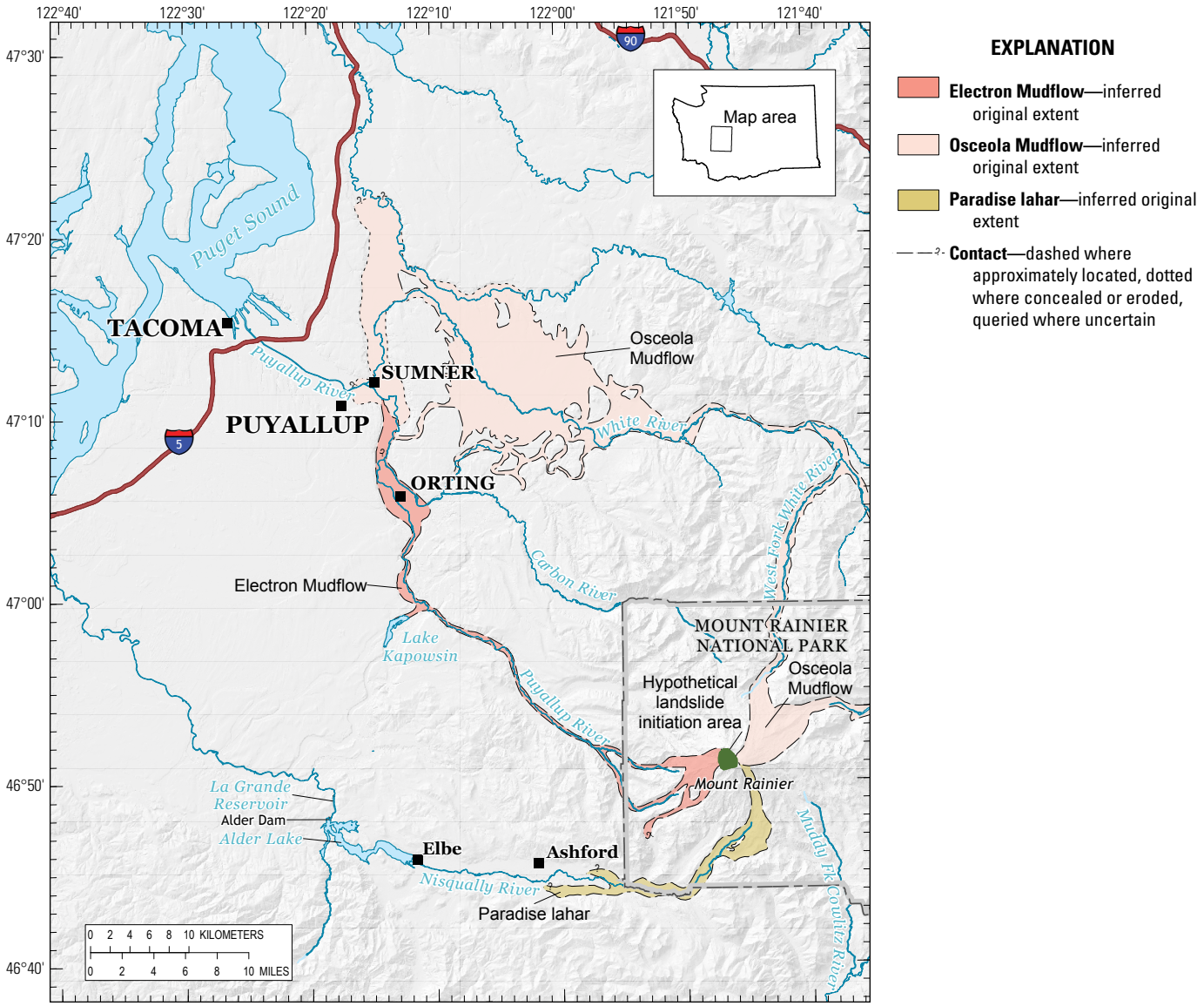

Base modified from U.S. Geological Survey National Elevation Dataset, 1/3 arc-second resolution and 1:24,000 scale
The National Map vector digital data, various dates
Universal Transverse Mercator Zone 10 projection, North American Datum of 1983

Figure 5. Shaded relief map of Mount Rainier and the surrounding area showing Holocene lahar paths as delineated by Crandell (1971). The Osceola Mudflow deposits are shown as a light pink area along the White River and Puget Sound lowlands. The Electron Mudflow deposits are shown as a dark pink area located in the Puyallup River valley. The Paradise lahar deposits are shown in the Nisqually River valley, upstream of the community of Elbe and Alder Lake. Hypothetical landslide initiation area indicates the source area of lahars modeled in this report.

volume of approximately 260 Mm^3 (Crandell, 1971; Scott and others, 1995). In the Puyallup River valley, it traveled more than 50 km downstream from Mount Rainier's summit and passed through the section of valley now occupied by the town of Orting (figs. 1 and 5). No geologic evidence discovered to date has linked the Electron Mudflow with eruptive activity (Sisson and Vallance, 2009). Therefore, the Electron Mudflow has been described as an unheralded lahar because no volcanic unrest is known to have preceded its sudden generation. The lahar likely resulted from gravity-driven collapse of a steep slope high on Mount Rainier's west side near the Sunset Amphitheater, an origin similar to that of the 50 Mm^3 Mount Meager, British Columbia, lahar of August 2010. The Electron Mudflow, however, was more than five times larger than the Mount Meager lahar. Although similar in volume to the Round Pass Mudflow, the Electron Mudflow appears to have been more mobile in the Puyallup River valley, leaving deposits as far downstream as Sumner (Scott and others, 1995).

The D-Claw Numerical Model

We perform our lahar computations using D-Claw, a depth-averaged numerical model we developed to simulate the behavior of debris flows, landslides, and lahars that comprise evolving mixtures of sediment and water (Iverson and George, 2014; George and Iverson, 2014). D-Claw has a mathematical structure that allows it to simulate dry rock avalanches and water floods, as well as transitions between flows that are composed predominantly of sediment or water. D-Claw has previously been used to simulate hazardous geologic events such as the 2014 landslide in Oso, Washington, and the 2015 Tyndall Glacier landslide and resulting tsunami in Taan Fiord, Alaska (Iverson and others, 2015; Iverson and George, 2016; George and others, 2017).

D-Claw is built on a foundation established by the open-source software package Clawpack (Mandli and others, 2016). Clawpack utilizes adaptive finite-volume numerical methods for solving general wave-propagation problems in diverse physical applications that are typically governed by hyperbolic conservation laws—partial differential equations derived by considering conservation of mass, momentum, and energy and satisfying mathematical stability properties (LeVeque, 2002). For computation of flow over irregular topography, D-Claw utilizes specialized algorithms that were first developed for simulations of tsunami propagation and inundation (George, 2006, 2008; LeVeque and others, 2011), and later extended to simulation of riverine water floods (George, 2011). The collection of algorithms tailored to simulate these shallow-water flows are a subset of Clawpack, called GeoClaw (Berger and others, 2011). D-Claw augments GeoClaw by utilizing more general governing equations derived for flows of grain-fluid mixtures such as landslides, debris flows, and lahars (George and Iverson, 2014; Iverson and George, 2014).

A key feature of D-Claw that enables it to simulate a wide variety of grain-fluid-mixture flows is its explicit computation of evolving values of the solid volume fraction (that is, the volumetric sediment concentration), denoted by a unitless variable, m. The physical, mathematical, and numerical basis of this computation are described in detail in previous reports (see, for example, George and Iverson, 2014; Iverson and George, 2014). Here we tabulate the model parameters used by our simulations (table 1) and provide a qualitative summary that emphasizes the influence of two important model parameters in the evolution of m and its effect on landslide liquefaction that leads to the generation of lahars. One of these parameters characterizes the tendency for landslide debris to contract or expand as it begins to move, and the other characterizes the tendency of a liquefied state to persist in moving debris.

As slow shearing of debris occurs early during slope failure, the debris' solid volume fraction evolves from its initial value, m_0, toward the value, m_{crit}, a quasi-static equilibrium (or critical-state) value, a quantity fundamental in the study of granular mechanics and sediment liquefaction (Jefferies and Been, 2016). Maximum values of m_0 apply in dense, hard rock masses ($m_0 \approx 0.9$), whereas typical values of m_0 in loose volcanic debris and hydrothermally altered volcanic rock commonly range from 0.4 to 0.8. As the moving debris increases in speed and becomes more agitated, the value of m evolves toward a dynamic equilibrium value that is smaller than m_{crit}. The value of m can also change if moving debris encounters and mixes with other materials, such as bodies of water in which $m_0=0$. Our simulations account for the effects of lahar interactions with standing water in lakes, but they do not account for the effects of lahar interactions with flowing river water. Instead we assume that the lahar volume, speed, and degree of liquefaction dominate the effects of pre-event streamflow. However, lahar interaction with river water is a topic for further investigation (see Pierson and Scott, 1985).

Table 1. Material parameters of lahars used in D-Claw model simulations.

[kg, kilogram; m^2, square meter; m^3, cubic meter; N, Newton; s, second]

Parameter	Symbol	Units	Value
Initial solid-volume fraction	m_0	none	[1]0.62
Quasi-static critical-state solid-volume fraction	m_{crit}	none	0.64
Initial hydraulic permeability of mixture	k_0	m^2	[2]10^{-11} or 10^{-9}
Intergranular-fluid viscosity of muddy water	μ	$N \cdot s/m^2$	0.005
Initial mixture compressibility[3]	α_0	m^2/N	8×10^{-7}
Solid-grain density	ρ_s	kg/m^3	2,700
Intergranular-fluid density of muddy water	ρ_f	kg/m^3	1,100
Coulomb friction angle of grains in contact with the bed	φ_b	degrees	38
Lateral pressure coefficient	κ	none	1

[1]For initial water in Alder Lake, $m_0=0$.

[2]The lesser permeability value ($k_0=10^{-11}$) is similar to that of sampled Osceola Mudflow deposits (Major and others, 1997) and was used for our high-mobility lahar simulations; the higher permeability value ($k_0=10^{-9}$) was used for our low-mobility lahar simulations.

[3]Compressibility values in D-Claw depend on the ambient stress state of the debris, which in turn depends on burial depth (Iverson and George, 2014). Here we list a value applicable at a depth of 10 m in static debris subject to lithostatic normal stress and hydrostatic pore-fluid pressure.

Detailed information about values of m_0 and m_{crit} in prospective landslide source areas high on the west side of Mount Rainier is lacking; in lieu of such information, each of the D-Claw simulations herein uses values of m_0 and m_{crit} like those used in best-fit simulations of the 2014 Oso, Washington, landslide (Iverson and George, 2016). Thus, our simulations for Mount Rainier use the value m_0=0.62 for all landslide source areas, irrespective of whether the materials consist predominantly of granular rock fragments, intact rock, or snow and ice (table 1). The simulations also use the value m_{crit}=0.64, and they consequently assume that the value $m_0 - m_{crit} = -0.02$ applies. This small negative value indicates that the landslide debris contracts slightly as the onset of slope failure begins, and that contraction promotes the onset of landslide liquefaction. Prior experience with D-Claw simulations shows that the use of $m_0 - m_{crit}$ values greater or less than −0.02 produces different model results, but those results differ greatly only if $m_0 - m_{crit}$ changes sign (Iverson and George, 2016). When $m_0 - m_{crit} > 0$ applies, little or no liquefaction occurs during slope failure, and D-Claw consequently simulates slow-moving landslides. Slow-moving landslides could occur on Mount Rainier, but they pose little down-valley hazard and are not addressed in this report.

The other parameter that greatly influences D-Claw simulation results is the hydraulic diffusivity of the debris. This property controls the rate at which high pore-fluid pressure dissipates and liquefaction ceases. More precisely, the hydraulic diffusivity, along with the local debris thickness, h, establishes the time required for relaxation of disequilibrium fluid pressure generated by evolution of m. As high fluid pressure relaxes toward a hydrostatic equilibrium pressure, the debris matrix becomes stronger and more resistant to motion. In D-Claw, the hydraulic diffusivity is expressed as

$$\text{Hydraulic diffusivity} = \frac{k}{\mu\alpha}, \tag{1}$$

where

k is the hydraulic permeability of the granular fraction of the debris;

μ is the dynamic viscosity of the fluid fraction of the debris; and

α is the bulk compressibility of the grain-fluid mixture.

The values of k and α evolve slightly in response to the evolution of m during D-Claw computations, but their initial static values are given by k_0 and α_0. Our Mount Rainier lahar simulations use values of k_0, α_0, and μ that are listed in table 1. For the highly mobile lahars considered below, these values yield $\frac{k_0}{\mu\alpha_0} = 2.5\times10^{-3}\,\mathrm{m^2/s}$, which implies that disequilibrium pore-fluid pressure in debris with a thickness of h= 10 m relaxes over a characteristic time $h^2\frac{\mu\alpha_0}{k_0} \approx 11$ hours. This long relaxation time implies that most debris in the large mobile lahars we model remains almost fully liquefied as it travels tens or even hundreds of kilometers downstream. For comparison, we also model lahars that have a higher hydraulic permeability, k_0, and thus a lesser ultimate mobility resulting from a much shorter relaxation timescale (~7 minutes) of the excess pore-fluid pressure.

Another important feature of D-Claw is its use of adaptive mesh refinement (AMR), a computational method that automatically and dynamically generates grid levels—multiple geographically evolving patches of grids with different resolutions—in order to adapt to evolving features in the computed flow (Berger and Oliger, 1984; Berger and Colella, 1989). This method has been specialized and tailored for modeling flows that inundate variable three-dimensional (3D) topography (Berger and others, 2011; George, 2011; LeVeque and others, 2011). The substantially enhanced computational efficiency and accuracy conferred by this technique (see, for example, George, 2011; LeVeque and others, 2011) facilitate the use of optimal grid resolutions, which vary drastically both spatially and temporally for lahars descending complex flow paths. For instance, where there is no landslide or lahar material at any given time, very coarse grids are desirable for computational efficiency. As the flow path extends, higher levels of grids—with finer spatial and temporal resolution—track and resolve the flow. Where the flow is highly dynamic or spatially variable (as it is near sharp features of topography such as cliffs), even higher levels of resolution can be employed to attain better numerical accuracy.

By continued evaluation of refinement (and de-refinement or coarsening) criteria throughout a simulation, AMR allots computational resources based on when and where they are needed. This approach makes possible the use of modern sub-meter light detection and ranging (lidar) topography only where it is needed within a very large domain. By doing so, AMR dramatically affects the simulation results where there are important yet small-scale topographic features at isolated locations (for example, dams, levees, buildings, and so on), which require fine-scale grid resolutions that would be prohibitively expensive computationally if applied to the entire domain. Table 2 lists the spatial resolution for adaptive grid levels used for the simulations described in this report. The

Table 2. Parameters of different grid levels of adaptive mesh refinement.

[--, no refinement; m, meter]

Level	Refinement ratio[1]	Spatial resolution	Spatial location
Level 1	--	1,024 m	Simulation domain[2]
Level 2	8	128 m	Varies with flow extent[3]
Level 3	8	16 m	Varies with flow extent[3]
Level 4	[4]4 (or 16)	[4]4 m (or 1 m)	Regions of interest[5]

[1]Refers to the integer subdivision (in each direction) of a lower level grid cell into higher level grid cells.

[2]Level 1 is the coarsest grid level used for the entire simulation domain.

[3]All flow material is refined to level 3, superseding the coarser level-2 resolution.

[4]Two alternative refinement schemes were used. Graphical results were produced using the 4-m resolution.

[5]Orting area and Alder Lake.

values in table 2 imply that a single level-1 grid cell contains $8^2 \cdot 8^2 \cdot 16^2$=1,048,576 1-m grid cells (or $8^2 \cdot 8^2 \cdot 4^2$=65,536 4-m grid cells) if refinement to level 4 occurs.

Mount Rainier Base Topography and Landslide Source Areas

D-claw computations presented in this report assume that the basal topographic surface is rigid (in other words, non-erodible) and impermeable. The simulated landslide or lahar material rests, flows, and forms deposits on top of this surface. Although D-Claw is capable of computing entrainment of erodible bed material, that feature is omitted in this study owing to a lack of suitable physical and geologic constraints. However, it is well known that lahars may increase in volume owing to entrainment of bed material along their flow paths (see for example, Scott and others, 1995; Vallance and Scott, 1997).

The single, globally defined, basal topographic surface utilized in D-Claw is automatically generated by synthesizing gridded elevation data for a prescribed basal landslide slip surface and surrounding terrain. The elevation data are required to be in the form of logically rectangular grids, or digital elevation models (DEMs). D-Claw's algorithms construct a single unique topographic surface from overlapping DEMs of different resolutions and coverage (George, 2006; LeVeque and others, 2011). The landslide basal slip surfaces are numerically constructed as described below in the "Source Areas and Failure Surfaces" section. The validity of D-Claw results is dependent on the accuracy and resolution of the utilized DEMs. However, the DEM resolution should not be confused with the D-Claw computational resolution described above for the adaptive multilevel grids. The computational resolution is determined only by input parameters set prior to runtime, the selection of which may be influenced by, but not strictly dependent on, the DEM resolution(s).

Digital Elevation Models

The digital elevation models utilized in this study contain ground-surface elevations for the valleys of rivers draining the west side of Mount Rainier. Elevations are mostly from the 1/9th arc-second (approximately 3 m) resolution U.S. Geological Survey National Elevation Dataset (NED). The NED data were produced from lidar surveys conducted from 2000 to 2011, which had reported vertical uncertainties of less than 0.5 m. The NED data were projected to the Universal Transverse Mercator zone 10 coordinate system and mosaicked to form a single elevation grid of the study area.

In the area of Alder Lake and La Grande Reservoir, water-surface elevations were replaced with approximations of lake-bed elevations. The bed elevation utilized for Alder Lake is based mostly on bathymetry data collected in 2010 and 2011 during the study of Czuba and others (2012). They estimated elevation uncertainty of about 0.25–1.4 m, and their point spacing varied for different parts of the lake. In areas of Alder Lake where no bathymetry data were collected, supplemental contours were added from the 1944 U.S. Geological Survey 1:62,500-scale Ohop Valley quadrangle map which depicts topography that predates the filling of Alder Lake reservoir. Additional inferred contours were drawn near Alder Dam so that the simulated dam has a base about 40 m wide and a crest about 5 m wide. A continuous elevation grid was interpolated from the bathymetry points and supplemental contours. Bed elevations of La Grande Reservoir were approximated by assuming parabolic cross sections orthogonal to a valley thalweg whose elevation decreases linearly from 275 to 230 meters (m).

In 2014, a new setback levee was constructed along the Puyallup River in Orting, and parts of an old levee were removed. These activities postdated the acquisition of the lidar data that provide the basis for our DEM in that area. We consequently modified the lidar topography at the construction and removal sites by conducting a ground-based Global Positioning System (GPS) survey of elevations along the new levee and by replacing elevations of removed sections of the old levee with elevations of the adjacent land surface as represented in a 2011 lidar terrain model.

Source Areas and Failure Surfaces

Our D-Claw simulations require use of prescribed landslide source area geometries, which we delineated using a four-step procedure. We first used the results of slope-stability calculations performed by Reid and others (2001) to identify the area on Mount Rainier's upper edifice that is most susceptible to gravitational failure (fig. 4). We then chose the volumes of the landslides we wished to simulate within this area. For our simulations, we chose two volumes: a large volume similar to that of the prehistoric Electron Mudflow at Mount Rainier (~260 Mm^3) and a smaller volume similar to that of the Mount Meager landslide and lahar of 2010 (~52 Mm^3). Next, we stipulated that these volumes were contained within landslide source areas with lateral boundaries that conform with existing topographic features. We then specified several longitudinal transects for each hypothetical slip surface (fig. 6), which had the form of logarithmic spirals—a commonly assumed shape for landslide slip surfaces in lieu of detailed data on the stratigraphy, structure, and geotechnical properties of the materials involved (see, for example, Jaboyedoff and others, 2020). Finally, we created continuous 3D slip surfaces by interpolating the transects using triangular facets. The transects and resulting slip surfaces were constrained by the specified landslide volumes enclosed above the slip surfaces and below the surface topography derived from the digital terrain model. For example, figure 6 shows the slip surfaces we used for landslides on the west side of Mount Rainier with volumes of approximately 260 Mm^3.

To generate the results presented in this report, we considered hypothetical landslide sources in two distinct locations on Mount Rainier's upper west edifice. These

locations, the Sunset Amphitheater and the Tahoma Glacier headwall, are to the north or south of Saint Andrews Rock, which forms a prominent topographic divide between the two (figs. 3, 6, and 7). The slope stability analysis of Reid and others (2001) identified the Tahoma Glacier headwall as the least stable sector of Mount Rainier's edifice, and the Sunset Amphitheater is the most probable source of the Electron Mudflow that occurred approximately 500 years ago. For each of the two landslide source areas, we constructed two landslide failure surfaces—one yielding a landslide volume of about 260 Mm^3 and the other yielding a volume of about 52 Mm^3. Finally, for each of the four hypothetical landslide surfaces, we performed simulations with two different values of the source material hydraulic permeability, k_0, which led to high-mobility (HM) lahars and relatively low-mobility (LM) ones.

In the sections below, we will refer to our eight distinct landslide and lahar scenarios using abbreviations that refer to their source location, volume, and mobility. We use "S" (for Sunset Amphitheater) to denote the source location on the north side of Saint Andrews Rock and "T" (for Tahoma Glacier headwall) to denote the source on the south side of Saint Andrews Rock (fig. 4). Landslide volume is denoted by "260" or "52," and mobility is denoted by "HM" (for high-mobility) or "LM" (for low-mobility). For example, S-260-HM refers to the 260 Mm^3 high-mobility lahar originating from Sunset Amphitheater and T-52-LM refers to the 52 Mm^3 low-mobility lahar originating from the Tahoma Glacier headwall (table 3).

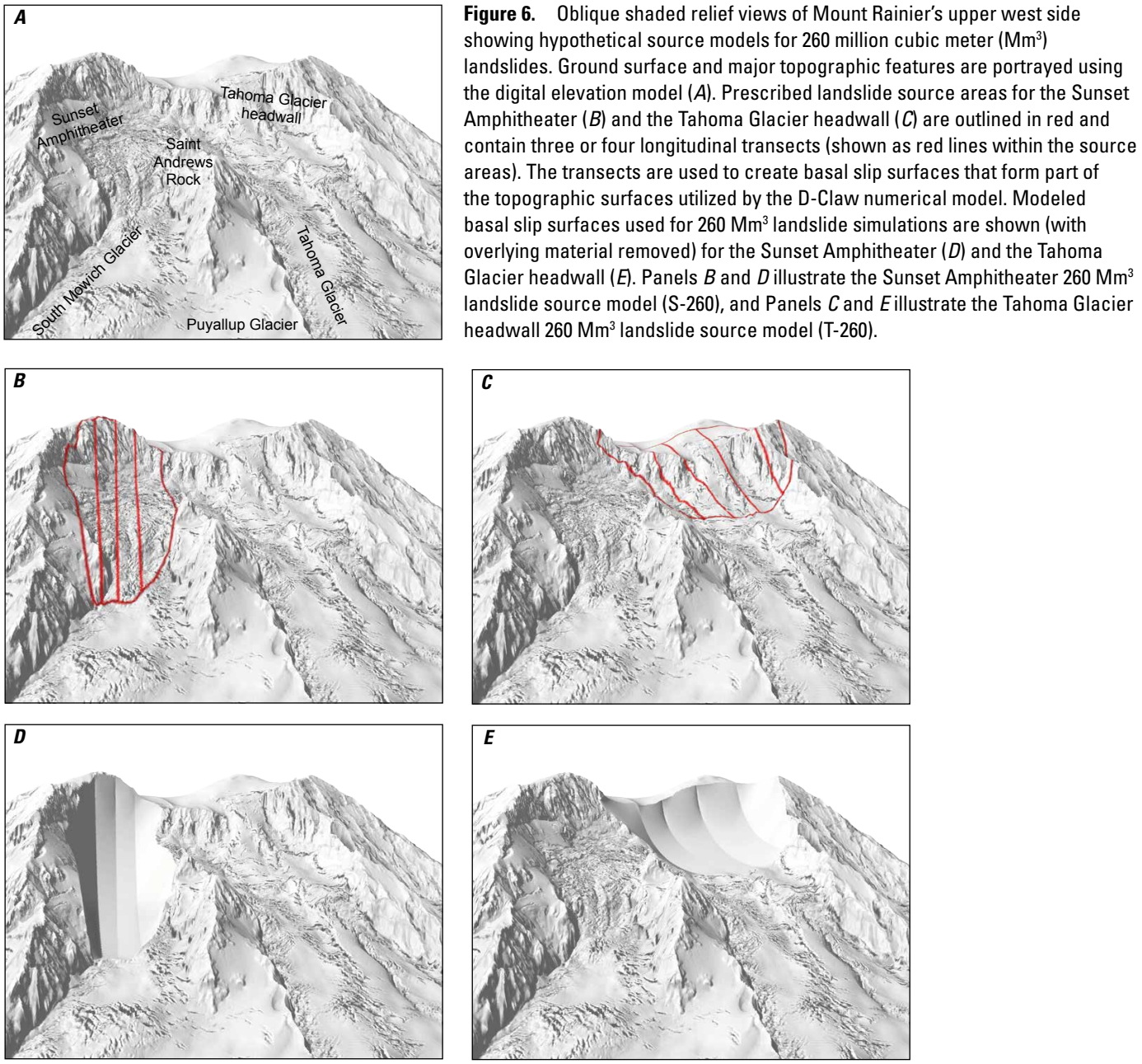

Figure 6. Oblique shaded relief views of Mount Rainier's upper west side showing hypothetical source models for 260 million cubic meter (Mm^3) landslides. Ground surface and major topographic features are portrayed using the digital elevation model (*A*). Prescribed landslide source areas for the Sunset Amphitheater (*B*) and the Tahoma Glacier headwall (*C*) are outlined in red and contain three or four longitudinal transects (shown as red lines within the source areas). The transects are used to create basal slip surfaces that form part of the topographic surfaces utilized by the D-Claw numerical model. Modeled basal slip surfaces used for 260 Mm^3 landslide simulations are shown (with overlying material removed) for the Sunset Amphitheater (*D*) and the Tahoma Glacier headwall (*E*). Panels *B* and *D* illustrate the Sunset Amphitheater 260 Mm^3 landslide source model (S-260), and Panels *C* and *E* illustrate the Tahoma Glacier headwall 260 Mm^3 landslide source model (T-260).

Base modified from U.S. Geological Survey National Elevation Dataset,1/9 arc-second resolution

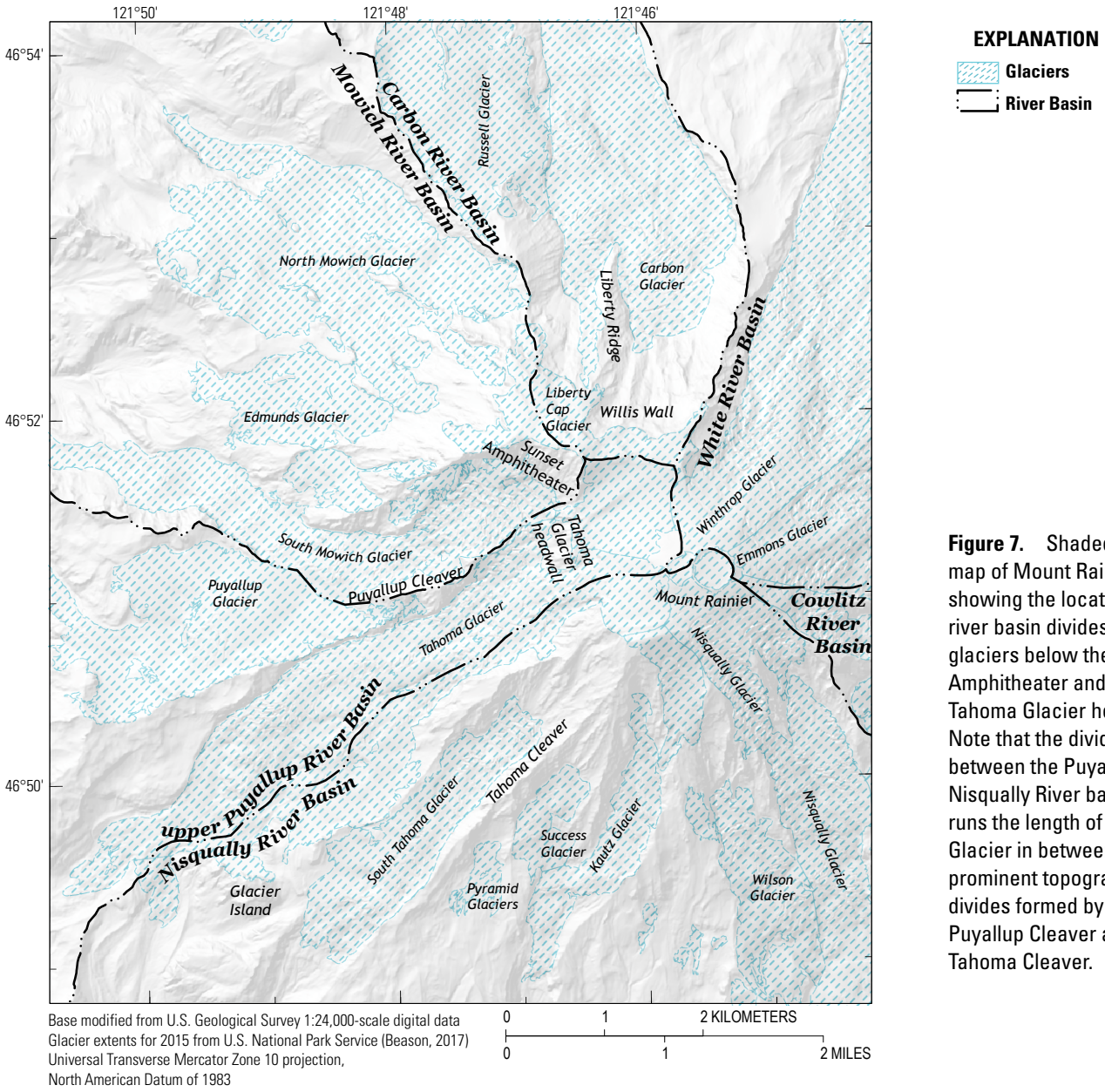

Base modified from U.S. Geological Survey 1:24,000-scale digital data
Glacier extents for 2015 from U.S. National Park Service (Beason, 2017)
Universal Transverse Mercator Zone 10 projection,
North American Datum of 1983

Figure 7. Shaded relief map of Mount Rainier showing the locations of river basin divides and glaciers below the Sunset Amphitheater and the Tahoma Glacier headwall. Note that the divide between the Puyallup and Nisqually River basins runs the length of Tahoma Glacier in between the more prominent topographic divides formed by the Puyallup Cleaver and the Tahoma Cleaver.

Table 3. Source locations, volumes, and initial source material permeabilities for the eight landslide-generated lahar scenarios considered in this report.

[HM, high-mobility; LM, low-mobility; S, Sunset Amphitheater is the source location; T, Tahoma Glacier headwall is the source location; Mm^3, million cubic meters; m^2, square meters]

Simulation	Source location	Volume (Mm^3)	Initial permeability, k_0 (m^2)
S-260-HM	Sunset Amphitheater	260	10^{-11}
T-260-HM	Tahoma Glacier headwall	260	10^{-11}
S-260-LM	Sunset Amphitheater	260	10^{-9}
T-260-LM	Tahoma Glacier headwall	260	10^{-9}
S-52-HM	Sunset Amphitheater	52	10^{-11}
T-52-HM	Tahoma Glacier headwall	52	10^{-11}
S-52-LM	Sunset Amphitheater	52	10^{-9}
T-52-LM	Tahoma Glacier headwall	52	10^{-9}

Hypothetical Lahars Originating on the West Side of Mount Rainier

The Electron Mudflow serves as a prototype guiding our simulation of hypothetical edifice failures on Mount Rainier for several reasons. First, it originated on the west side of Mount Rainier—the area considered most likely for future slope failures. Additionally, it is not associated with any known eruptive activity. In this report, we aim to characterize worst-case scenarios that could occur in the absence of precursory volcanic unrest. Although the nature of a triggering mechanism is not posited in this study, we have avoided scenarios that presuppose associated volcanism. However, our hypothetical scenarios do not preclude a volcanic trigger. Therefore, the large volume (an estimated ~260 Mm^3; Scott and others, 1995) of the Electron Mudflow acts as a logical upper bound for our worst-case source volume.

Another key property of the Electron Mudflow was its relatively high clay content—approximately 8 percent by dry sediment weight (Scott and others, 1995). The existence of this high percentage of clay-sized material in any lahar increases the hazards it poses, because clay can enhance a lahar's tendency to remain mobile on account of its ability to sustain elevated pore-fluid pressures (Iverson and others, 2010). Our simulations of worst-case events use parameter values that cause the modeled lahars to be almost entirely liquefied owing to persistently high pore-fluid pressure as they travel many tens of kilometers downstream. However, we stress that our scenarios do not represent an attempt to reproduce the source or the downstream dynamics of the Electron Mudflow.

Simulation Results

The results described in the following section focus largely on the two landslides with the largest volumes and greatest mobilities (S-260-HM and T-260-HM), which represent our worst-case scenarios of lahar generation. The source geometries for these landslides are depicted in figure 6. We also present results for smaller and less mobile lahars to help illuminate the potential for variability. The eight scenarios are introduced and described in the "Hypothetical Worst-Case Scenarios" and "Lahars of Smaller Volume and Lower Mobility" sections; further analysis and comparisons of the scenarios at selected locations are provided in the "Lahar Speeds, Depths, and Discharges at Selected Locations" section.

For each of the simulations, D-Claw is initialized with landslide material (table 1) filling the volume between the failure surface and ground surface, as represented by DEMs. Lakes are initialized with pure water (m_0=0) filling the volume beneath a specified lake-surface elevation and above lake-bottom bathymetry specified in the synthesized DEM.

The landslide failure process is initiated in D-Claw by user specification of the normalized basal pore-fluid pressure at t=0 or during a time interval, t, when $t_s \le t \le t$=0, where t_s is the start of the simulation and t=0 represents the onset of landslide motion. The normalized basal pore-fluid pressure is expressed as,

$$\text{Normalized basal pore-fluid pressure} = \frac{P_b}{\rho g h}, \qquad (2)$$

where

P_b is basal pore-fluid pressure;
ρ is the bulk density of the landslide source material;
h is its vertical thickness, which varies spatially; and
g is the magnitude of gravitational acceleration.

In simulations reported here, the normalized basal pore-fluid pressure is uniformly incremented to mimic rising fluid pressure owing to natural external sources such as rainfall, snowmelt, or hydrothermal activity prior to slope failure. Pore pressure increases until the frictional resistance to motion can no longer balance the effect of gravitational driving forces. In the scenarios presented, this threshold is crossed when basal fluid pressures are less than hydrostatic basal fluid pressure (that is, the static basal fluid pressure that exists in a completely saturated grain-fluid mixture at rest). The simulation then proceeds without further manipulation of the basal pore pressure or any other variable. After slope failure commences, landslides may transform into highly mobile debris flows, owing to granular contraction and liquefaction, or they may slump and stabilize if deformation of the source material is dilative (meaning that shearing leads to greater porosity). Our simulations include only cases in which contractive deformation drives up the basal pore pressure and leads to at least partial liquefaction.

Hypothetical Worst-Case Scenarios

S-260-HM Landslide and Lahar Inundation of the Puyallup River Valley

We first consider the worst-case scenario, modeled by simulation S-260-HM, arising from a 260 Mm^3 landslide that encompasses much of the Sunset Amphitheater (figs. 3, 6–8). After the onset of slope failure, the liquefying landslide quickly transforms into highly mobile flows as material descends the steep west side of Mount Rainier. Most of this material moves down the Puyallup Glacier north of Saint Andrews Rock to enter the Puyallup River headwaters, but a notable fraction of material travels farther south onto the Tahoma and South Tahoma Glaciers, some of which enters the headwaters of the Nisqually River. Additionally, some material travels farther north onto the South Mowich Glacier and enters the headwaters of the Mowich River, a tributary of the Puyallup River (figs. 6, 7, 9, and 10). The relatively small flow entering the Nisqually River system is shallow and forms deposits near the upstream reach of the valley, just outside the boundary of Mount Rainier National Park (figs. 1, 10, and 11). In contrast, the flow that enters the Puyallup River system from the north is large and fast moving. Near the terminus of Puyallup Glacier, this lahar bifurcates into the South Puyallup and North Puyallup River forks, as well as into the Mowich River farther to the north, before merging again at the confluences of these Puyallup River tributaries

within 5–10 minutes (fig. 10). The lahar then travels down a steep and narrow reach of the main fork of the Puyallup River valley (bottom panels of fig. 11), at speeds exceeding 50 m/s (110 mi/hr). Once it emerges from the narrow ravine upstream of Orting, the high-speed lahar slows and spreads across the wide valley bounded by the Puyallup River on the west and the Carbon River to the east.

At t≈30 minutes, the lahar continues down the Puyallup River valley toward Orting, reaching the outskirts of that community at t≈50 minutes (figs. 11 and 12). The maximum inundation depth, H, in the Orting area for the duration of the simulation (shown in figure 13) is defined as

$$H(x, y) = \max_{t\in[0,T]} h(x, y, t), \quad (3)$$

where

H is the maximum inundation depth;
x and y are spatial coordinates;
t is time;
T is the final simulation time (T=8 hours); and
h is the evolving flow depth.

The peak inundation depths range from 1 to more than 5 m, and inundation limits are constrained only by natural terrain boundaries. The quantity, H, depicted as the maximum lahar flow depth in figure 13 should not be confused with the thickness of static lahar deposits that are left after lahar passage. In the simulation, much of the material that causes the peak inundation continues downstream. Maximum inundation depths, H, increase beyond Orting as the lahar travels toward Sumner, particularly where the valley narrows (fig. 14).

Downstream from Orting, at the confluence of the Puyallup and White Rivers near the community of Sumner, the lahar bifurcates, sending some material upstream into the White River valley northward (at t≈3 hours; fig. 14). Lahar material also continues west down the Puyallup River valley but comes to rest at t≈5 hours in the low-elevation areas surrounding the communities of Sumner and Puyallup (fig. 14).

T-260-HM Landslide and Lahar Inundation of the Nisqually River and Alder Lake

We next consider the worst-case scenario, modeled by simulation T-260-HM, arising from a landslide above the Tahoma Glacier, which lies just south of Sunset Amphitheater on the west side of Mount Rainier (figs. 3 and 6). This is the location identified by Reid and others (2001) as the most gravitationally unstable sector on the upper edifice of Mount Rainier. We constructed a detailed hypothetical landslide geometry for this simulation in a manner analogous to that for our S-260-HM landslide simulation, by using the location and desired landslide volume to fit logarithmic spirals to a hypothetical basal slip surface. As in the S-260-HM simulation, initial slope failure in the T-260-HM simulation leads to high-speed flows on the steep sides of Mount Rainier that carry material into the Puyallup and Nisqually River valleys. However, compared to the S-260-HM simulation, a much greater fraction of the T-260-HM flow crosses the Tahoma and South Tahoma Glaciers and enters the Tahoma Creek and the Nisqually River valleys to the south (figs. 15–18), whereas the lahar that flows northward into the Puyallup River valley in the T-260-HM simulation, although substantial, is not as large or as rapidly flowing as the lahar produced in that watershed by the S-260-HM simulation. Consequently, this section focuses on the results of the T-260-HM simulation within the Nisqually River watershed (comparisons of the scenarios in each river basin are further described in the "Lahar Speeds, Depths, and Discharges at Selected Locations" section).

Within 10 minutes of the landslide onset, the lahar descends Tahoma Creek to the Nisqually River near the entrance to Mount Rainier National Park. It subsequently flows down the Nisqually River valley through the communities of Ashford and Elbe (figs. 15 and 18), and ultimately enters Alder Lake reservoir (fig. 18). The potential hazard associated with lahar inundation of Alder Lake reservoir is of particular interest because of the hydroelectric dam that impounds the reservoir. The 100-m high, 490-m long Alder Dam could potentially be overtopped by lahar-generated seiche waves or by rising lake levels caused by mass displacement of water.

Alder Lake reservoir spans approximately 11 km from the community of Elbe, near its eastern end, to Alder Dam, which was constructed in 1945 and is currently operated by Tacoma Power (fig. 19). The reservoir is at full capacity when the lake-surface elevation is 368 m above sea level (from the Tacoma Power website, available at www.mytpu.org), leaving little distance between the lake surface and the top of the dam. Alder Lake has a volume comparable to that of our T-260-HM lahar (~300 Mm^3 of water). However, its surface area at full capacity is about 12 Mm^2, implying that a lahar capable of displacing substantially less than 100 Mm^3 of lake water could instigate dam overtopping when the reservoir is near capacity. Because of seasonal variations, our simulations required a somewhat arbitrary selection for the lake-water level. We chose a near-full capacity lake surface elevation of 364 m, a choice that was partially influenced by available data from Czuba and others (2012), which aided in the bathymetric interpolation near the shoreline (see section "Mount Rainier Base Topography and Landslide Source Areas").

The simulated Nisqually River branch of the T-260-HM lahar reaches the head of Alder Lake at t≈50 minutes, after which the lahar displaces and mixes with water near its advancing front (figs. 20 and 21). This interaction does not generate high-amplitude waves like those caused by some landslide-generated tsunamis (for example, George and others, 2017), probably owing to the shallowness of Alder Lake at its upstream end and to the low gradient of the valley floor where the lahar enters the lake (resulting in relatively modest lahar speeds of ~10 m/s). Instead, the interaction primarily

causes a gradual lake level rise that advances progressively farther ahead of the mixing region (compare figs. 21 and 22) through the reservoir and toward the dam, eventually leading to overtopping of the dam about 20 minutes after the lahar reaches the lake (fig. 23). The lahar material itself does not reach the dam in substantial concentrations during this simulation, which is halted at *t*=2 hours (approximately 30 minutes after dam overtopping begins; figs. 21 and 23).

In the event of a lahar entering Alder Lake and displacing a considerable volume of water, the extent and duration of outflow over the dam would depend on many factors, including the initial lake stage and lahar dynamics. Assessment of the dam's resilience and any effects of dam overtopping downstream from Alder Lake are beyond the scope of this study, but our results imply that further investigation of these topics might be warranted.

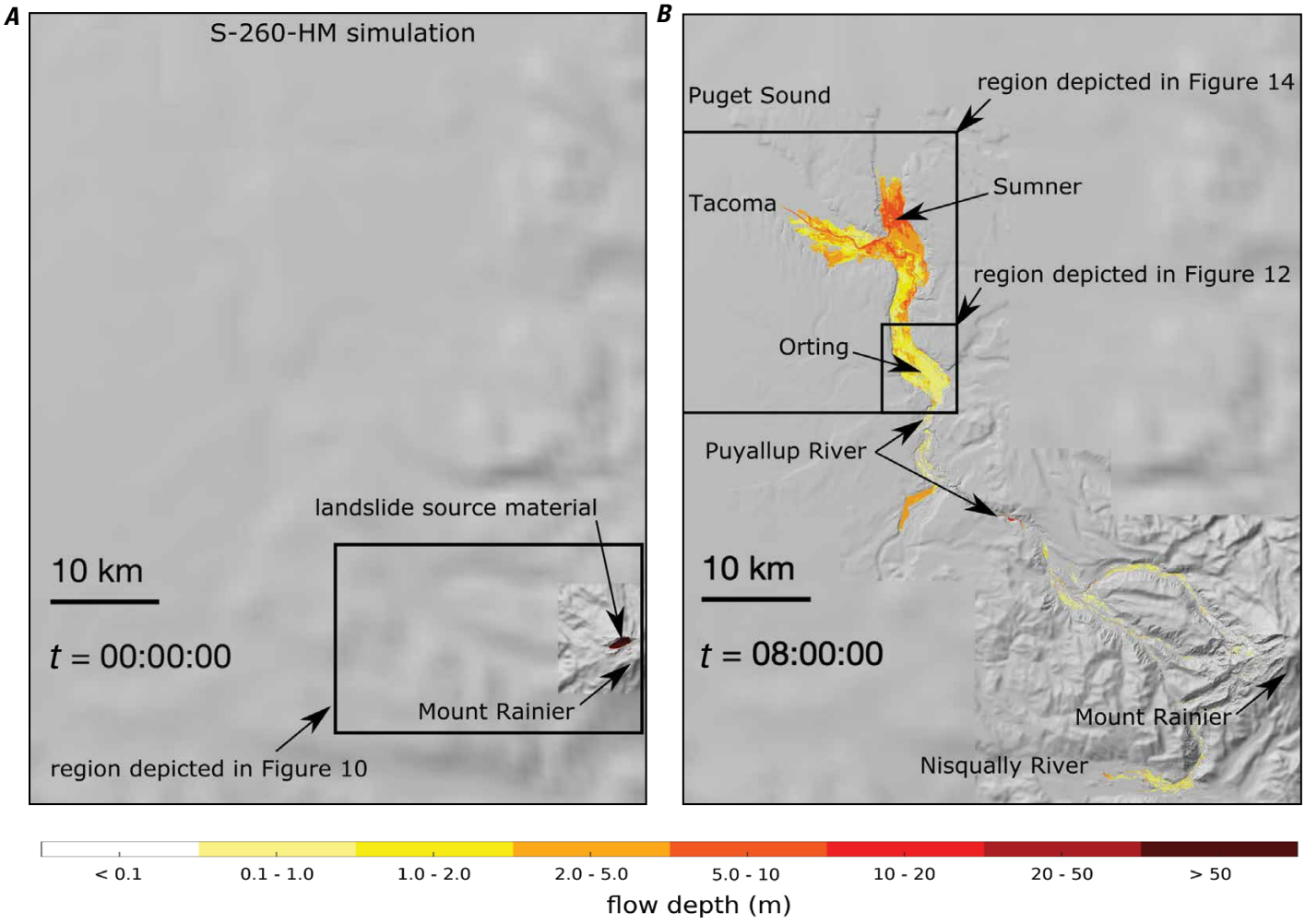

Figure 8. Shaded relief maps showing landslide and lahar flow depths of the S-260-HM simulation just before the onset of slope failure at time *t*=0 (*A*) and at the simulation's final computed time (*t*=8 hours; *B*). The simulation area extends from just southeast of Mount Rainier's summit (lower right corner of maps *A*, *B*) to Puget Sound near Tacoma (upper left corner of maps *A*, *B*). Color shading indicates landslide and lahar flow depths in meters (m). Imagery appears blurry in parts of the simulation area where lahar material is absent because D-Claw's adaptive mesh refinement (AMR) employs very coarse resolution in those areas. Black boxes enclose areas for which enlarged views are provided in figures 10, 12, and 14. Time (*t*) is indicated in hours:minutes:seconds. km, kilometers.

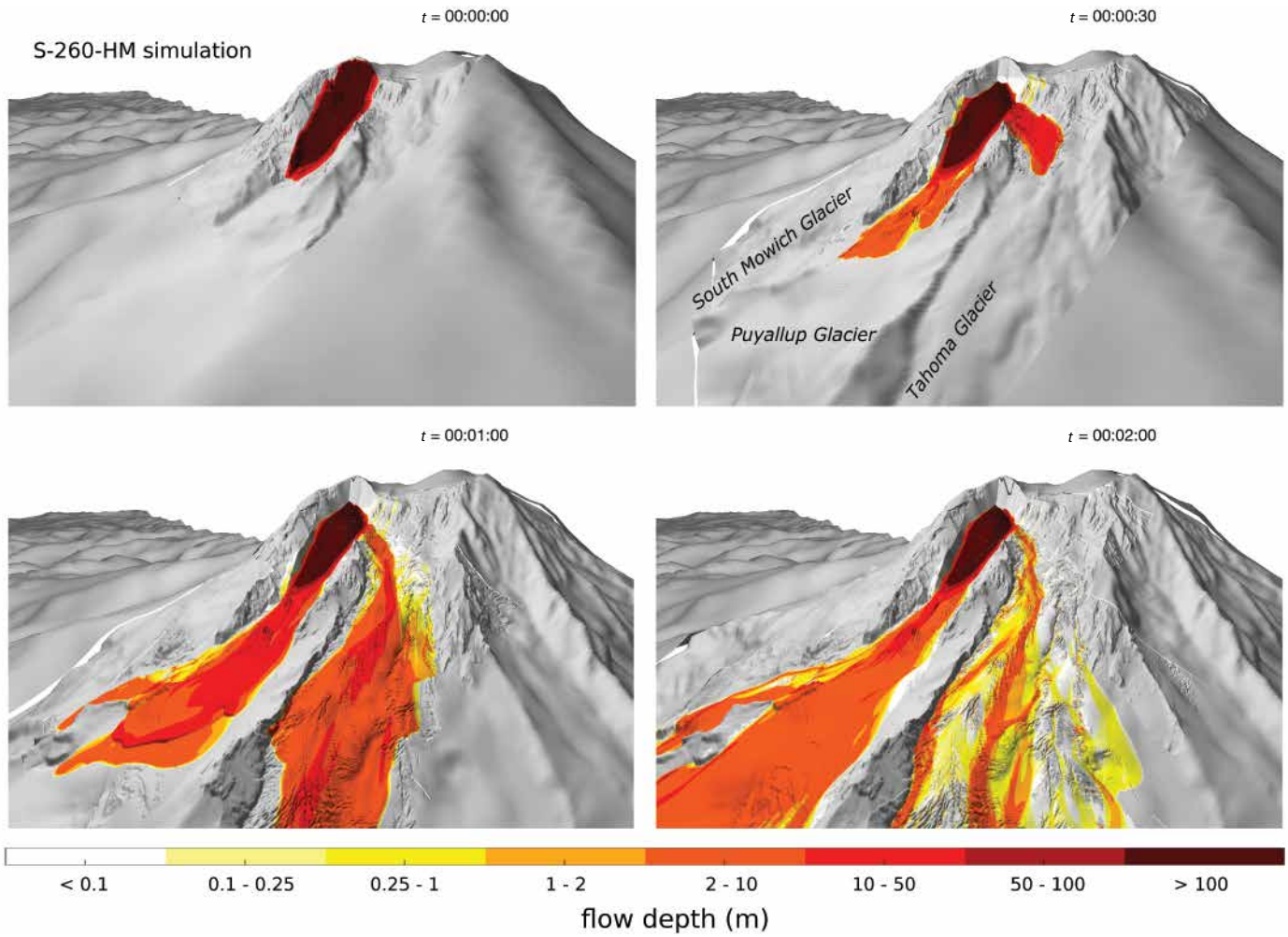

Figure 9. Close-up oblique views of Mount Rainier's west side showing landslide and lahar flow depths of the S-260-HM simulation at selected times during the first 2 minutes of lahar motion. The landslide originates from the Sunset Amphitheater near the summit of Mount Rainier and subsequently transforms into highly mobile flows on the South Mowich, Puyallup, Tahoma, and South Tahoma Glaciers. Most of the flows enter headwaters of the Puyallup River valley (including the Mowich River farthest to the north). The fraction of landslide material farthest to the south, on the south edge of the Tahoma Glacier and South Tahoma Glacier, ultimately flows into tributaries of the Nisqually River (the Puyallup-Nisqually drainage boundary bisects the Tahoma Glacier, as illustrated in fig. 7). Color shading indicates landslide and lahar flow depths in meters (m). Imagery appears blurry where lahar material is absent because D-Claw's adaptive mesh refinement (AMR) employs very coarse resolution in those areas. Time (*t*) is indicated in hours:minutes:seconds. Supplemental animation available at https://doi.org/10.3133/ofr20211118.

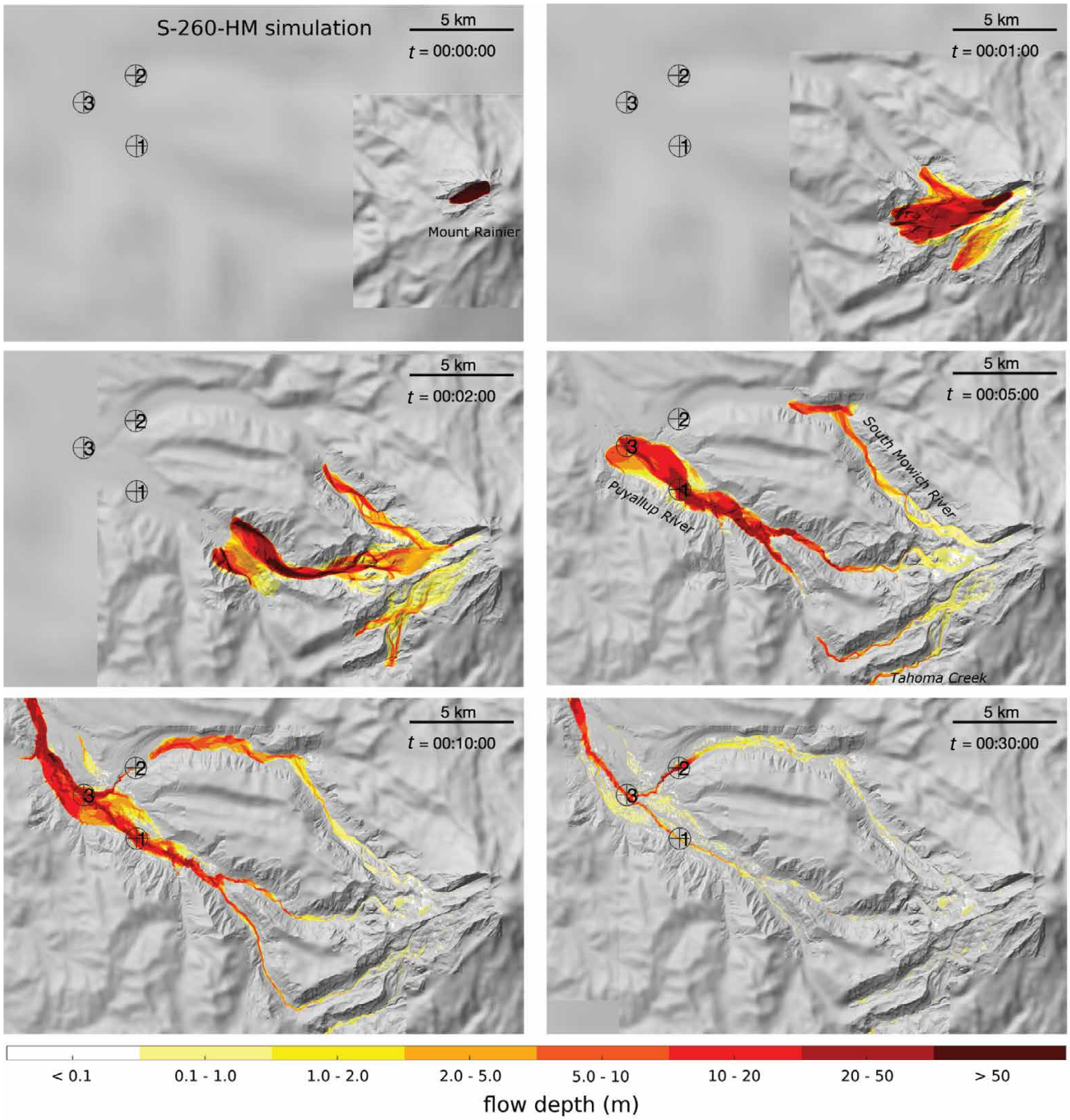

Figure 10. Shaded relief maps showing landslide and lahar flow depths of the S-260-HM simulation at selected times during the first 30 minutes of lahar motion. Imagery appears blurry where lahar material is absent because D-Claw's adaptive mesh refinement (AMR) employs very coarse resolution in those areas. Successive frames show that landslide material travels primarily into the Puyallup River valley from the South Mowich, Puyallup, and Tahoma Glaciers (though a small fraction of material spills onto the Tahoma and South Tahoma Glaciers, as well, and the southernmost part of this flow enters Tahoma Creek, a tributary of the Nisqually River south of Mount Rainier). Color shading indicates landslide and lahar flow depths in meters (m). Circled numbers are reference points for computed time series described in the "Lahar Speeds, Depths, and Discharges at Selected Locations" section. Time (*t*) is indicated in hours:minutes:seconds. km, kilometers.

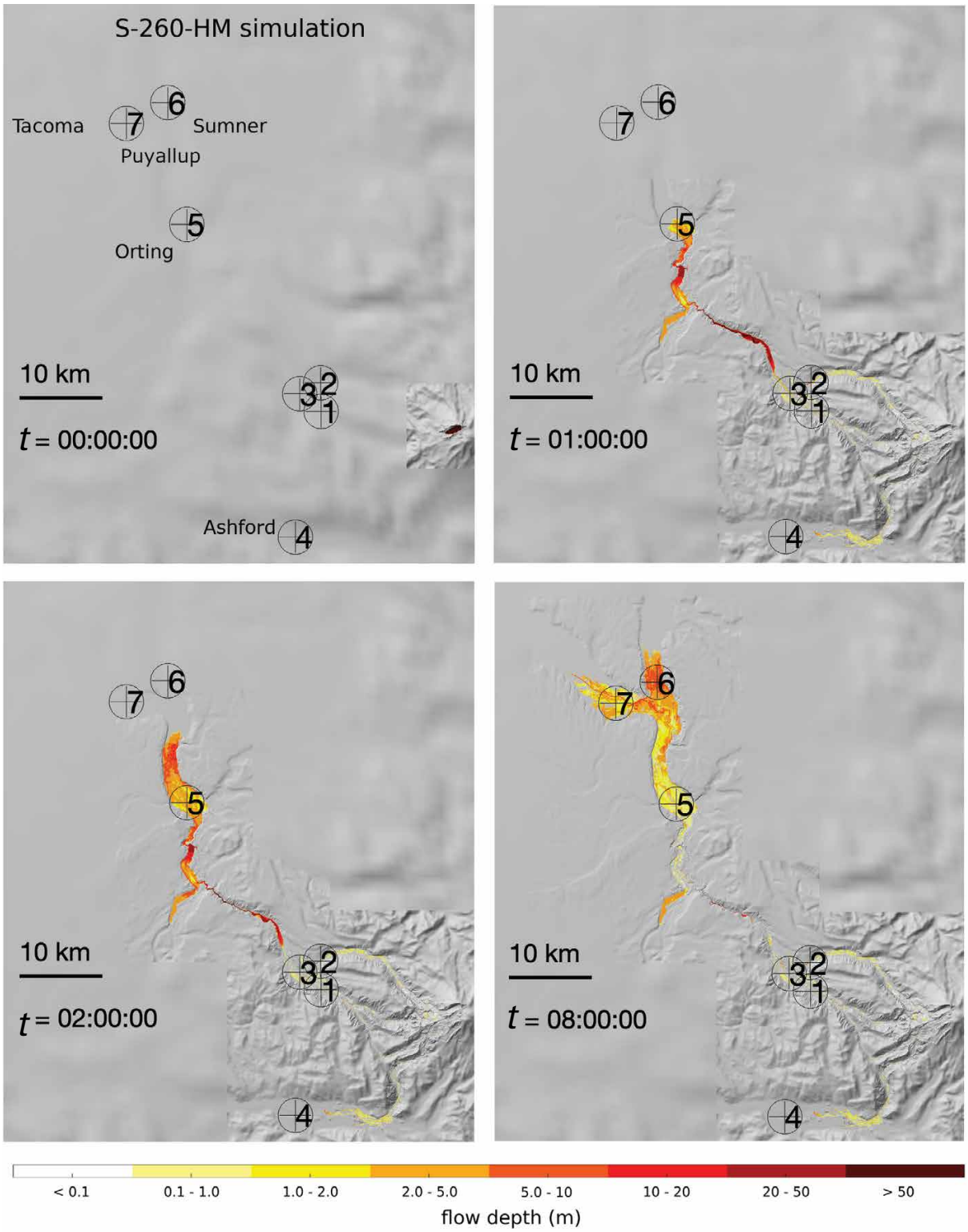

Figure 11. Shaded relief maps showing landslide and lahar flow depths of the S-260-HM simulation at selected times during the first 8 hours of lahar motion. Imagery appears blurry where lahar material is absent because D-Claw's adaptive mesh refinement (AMR) employs very coarse resolution in those areas. The lahar primarily affects the Puyallup River valley northwest of Mount Rainier toward Puget Sound. The lahar slows considerably along the wide, low-gradient valley floor surrounding and beyond Orting. The lahar comes to rest at time $t \approx 5$ hours in the low areas in the Puyallup River valley surrounding Sumner and Puyallup, upstream from Port of Tacoma and Puget Sound. Color shading indicates landslide and lahar flow depths in meters (m). Circled numbers are reference points for computed time series described in the "Lahar Speeds, Depths, and Discharges at Selected Locations" section. Time (*t*) is indicated in hours:minutes:seconds. km, kilometers. Supplemental animation available at https://doi.org/10.3133/ofr20211118.

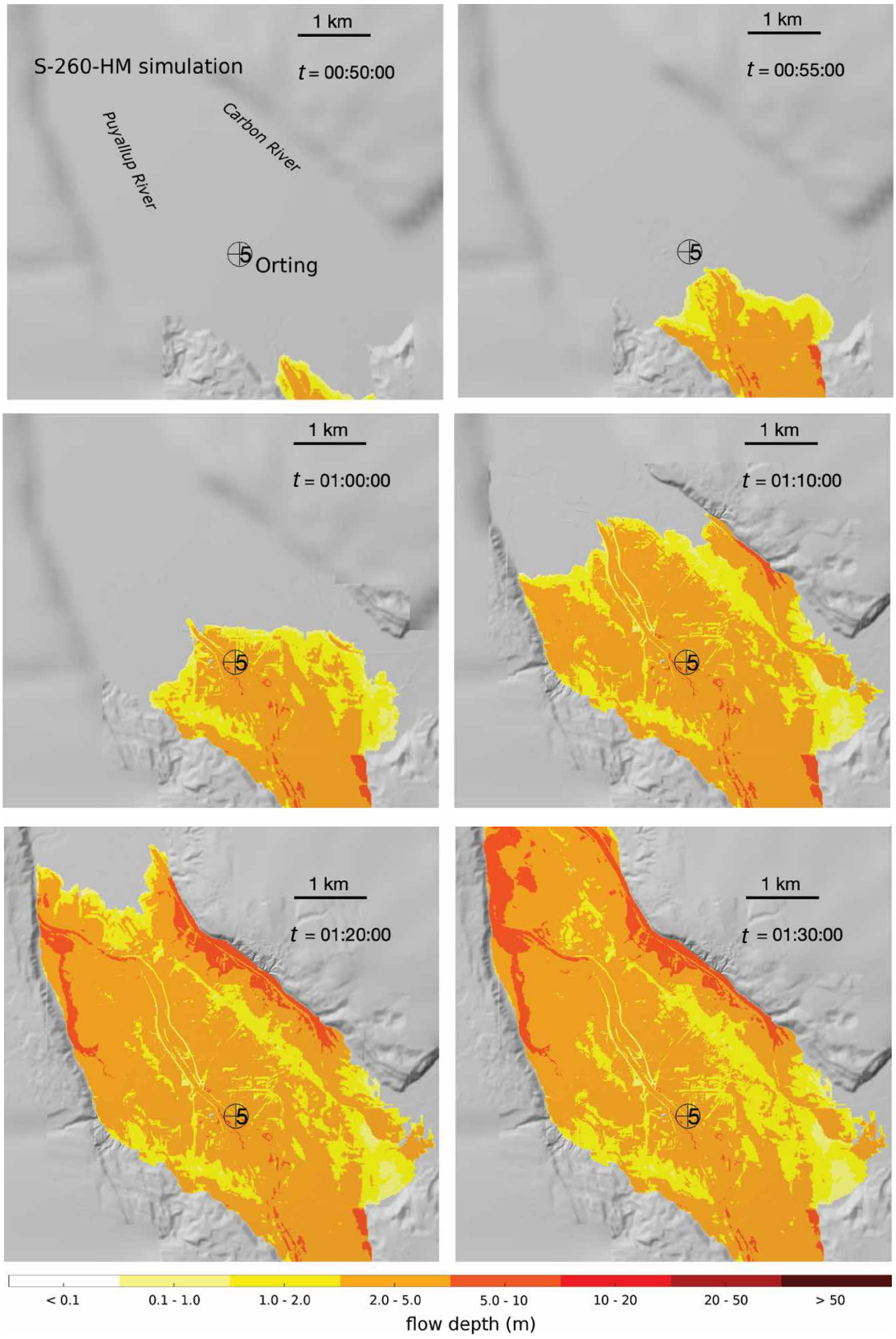

Figure 12. Shaded relief maps showing lahar flow depths of the S-260-HM simulation at selected times, focused on the valley bottom surrounding Orting. Imagery appears blurry where lahar material is absent because D-Claw's adaptive mesh refinement (AMR) employs very coarse resolution in those areas. The simulated lahar inundates the entire valley surrounding Orting, confined by the benches west of the Puyallup River and east of the Carbon River, which rise about 100 meters above the valley floor. Color shading indicates lahar flow depths in meters (m) at the respective time. Time (*t*) is indicated in hours:minutes:seconds. km, kilometers. Supplemental animation available at https://doi.org/10.3133/ofr20211118.

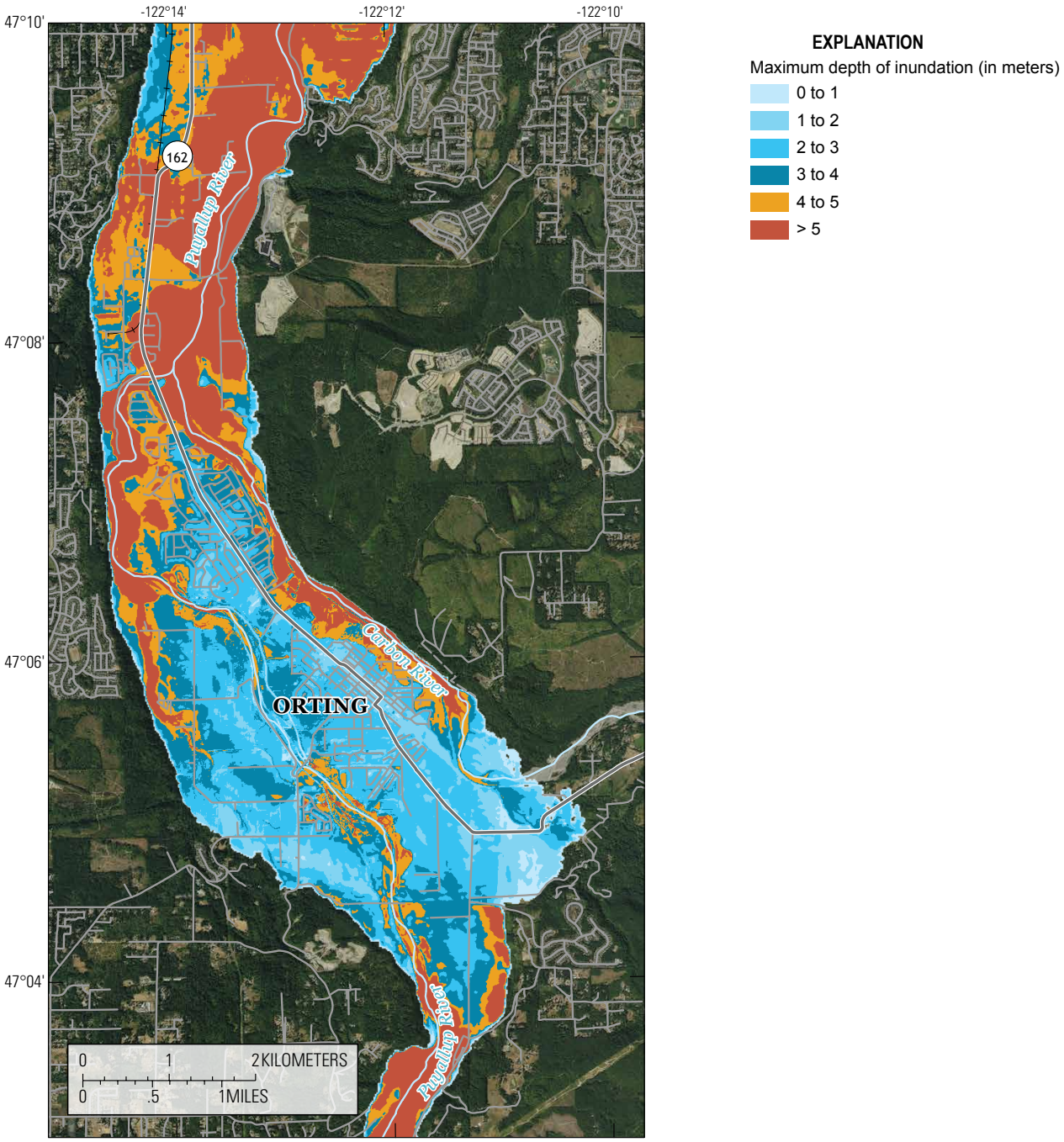

Base from U.S Department of Agriculture orthophotograph, 2017, and U.S. Geological Survey 1:24,000 scale vector digital data
Universal Transverse Mercator Zone 10 projection, North American Datum of 1983

Figure 13. Map showing maximum depths of lahar inundation in Orting and the surrounding valley. The colors represent the maximum depth of inundation, H, computed in the simulation for all times $t>0$. The maximum inundation depth is transitory and should not be confused with the thickness of static lahar deposits that are left after lahar passage.

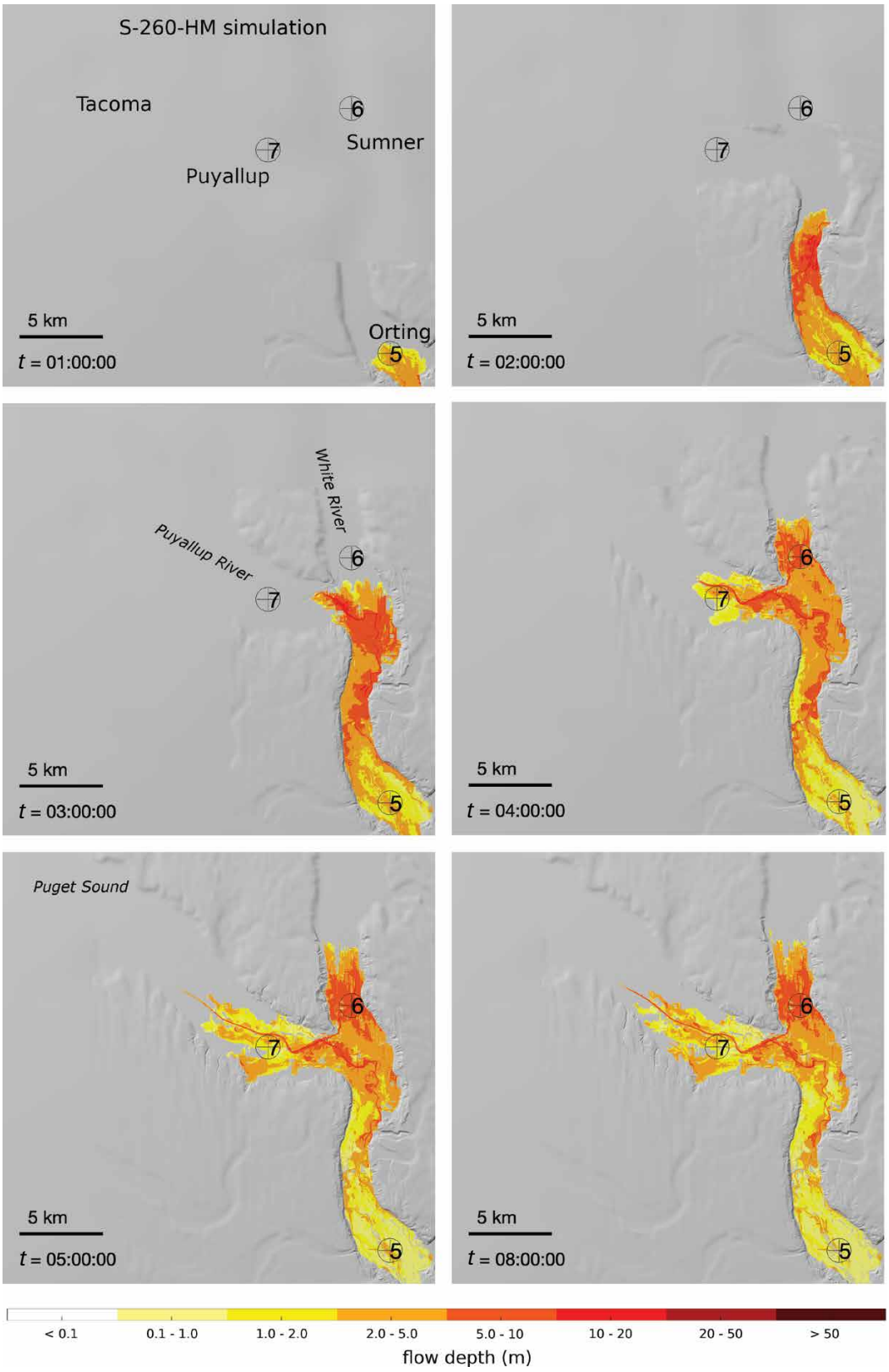

Figure 14. Shaded relief maps showing lahar flow depths of the S-260-HM simulation at selected times $t \geq 1$ hour, focused on the Puyallup River valley between Orting and the Port of Tacoma. Imagery appears blurry where lahar material is absent because D-Claw's adaptive mesh refinement (AMR) employs very coarse resolution in those areas. The flow proceeds slowly down the Puyallup River downstream from Orting, coming to rest at time $t \approx 5$ hours upstream from Puget Sound. Color shading indicates lahar flow depths in meters (m) at the respective time. Circled numbers are reference points for computed times series described in the "Lahar Speeds, Depths, and Discharges at Selected Locations" section. Time (t) is indicated in hours:minutes:seconds. km, kilometers. Supplemental animation available at https://doi.org/10.3133/ofr20211118.

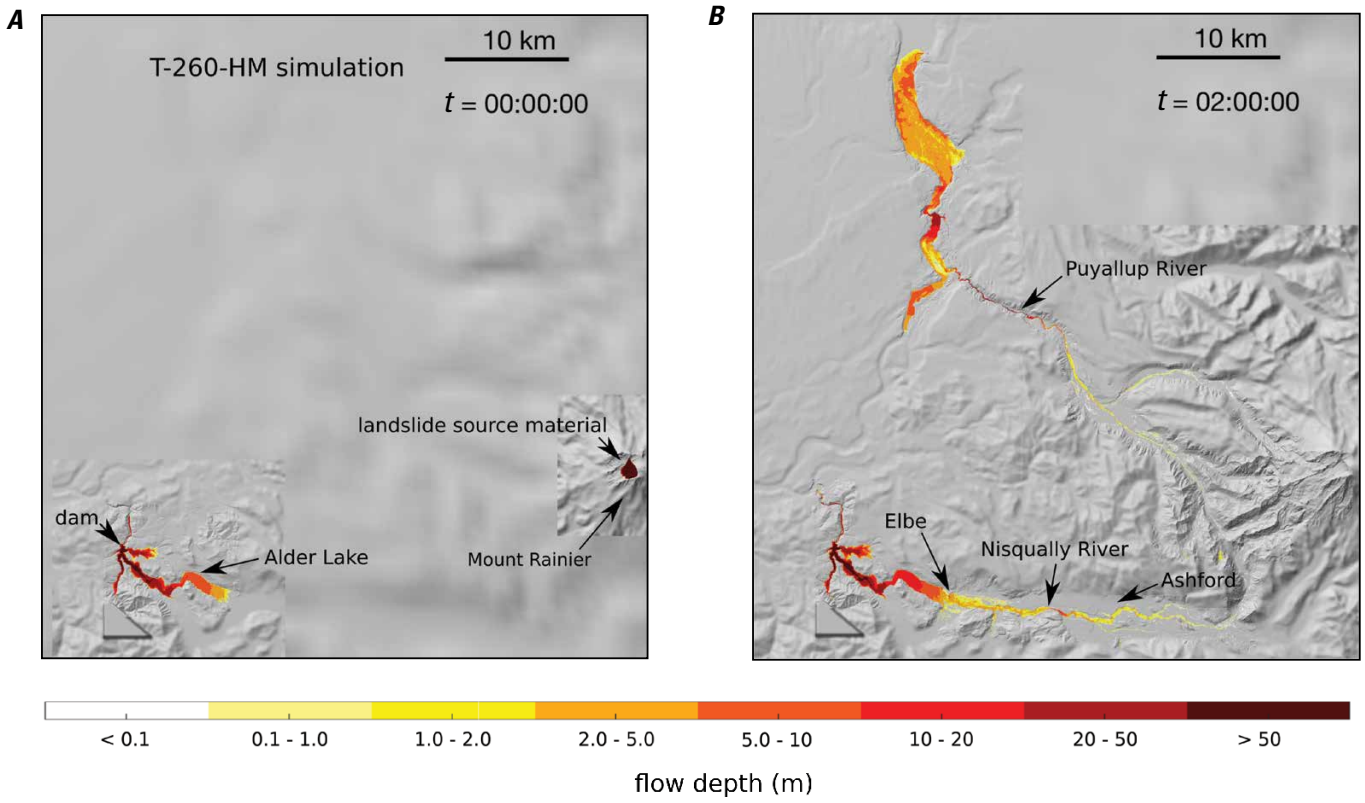

Figure 15. Shaded relief maps showing landslide and lahar flow depths of the T-260-HM simulation just before the onset of slope failure at time *t*=0 (*A*) and at the simulation's final computed time (*t*=2 hours; *B*). Imagery appears blurry where lahar material or lake water are absent because D-Claw's adaptive mesh refinement (AMR) employs very coarse resolution in those areas. The maps show the full extent of the simulation area. At *t*=2 hours (*B*), the material in both the Nisqually and Puyallup River basins has largely drained from the upper watersheds. Alder Lake reservoir is visible near the southwest corner of the simulation area. Color shading indicates landslide and lahar flow depths (as well as water depths in Alder Lake) in meters (m). Time (*t*) is indicated in hours:minutes:seconds. km, kilometers.

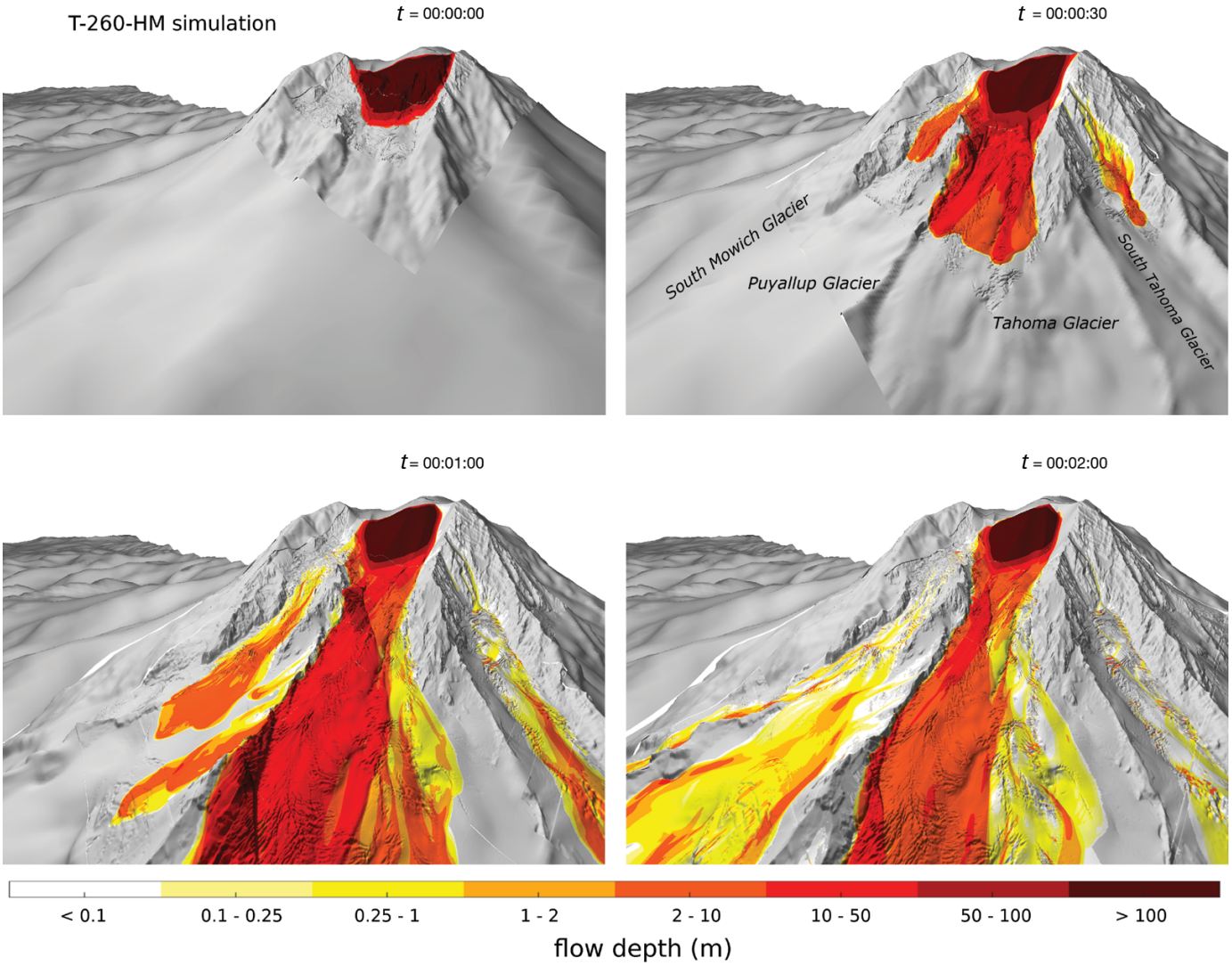

Figure 16. Close-up oblique views of Mount Rainier's west side showing landslide and lahar flow depths of the T-260-HM simulation at selected times during the first 2 minutes of lahar motion. Imagery appears blurry where lahar material is absent because D-Claw's adaptive mesh refinement (AMR) employs very coarse resolution in those areas. The landslide transforms into highly mobile flows, which enter both the Puyallup River valley (heading from the South Mowich, Puyallup, and Tahoma Glaciers) and the Nisqually River valley (heading from the Tahoma and South Tahoma Glaciers). Color shading indicates landslide and lahar flow depths in meters (m). Time (*t*) is indicated in hours:minutes:seconds. Supplemental animation available at https://doi.org/10.3133/ofr20211118.

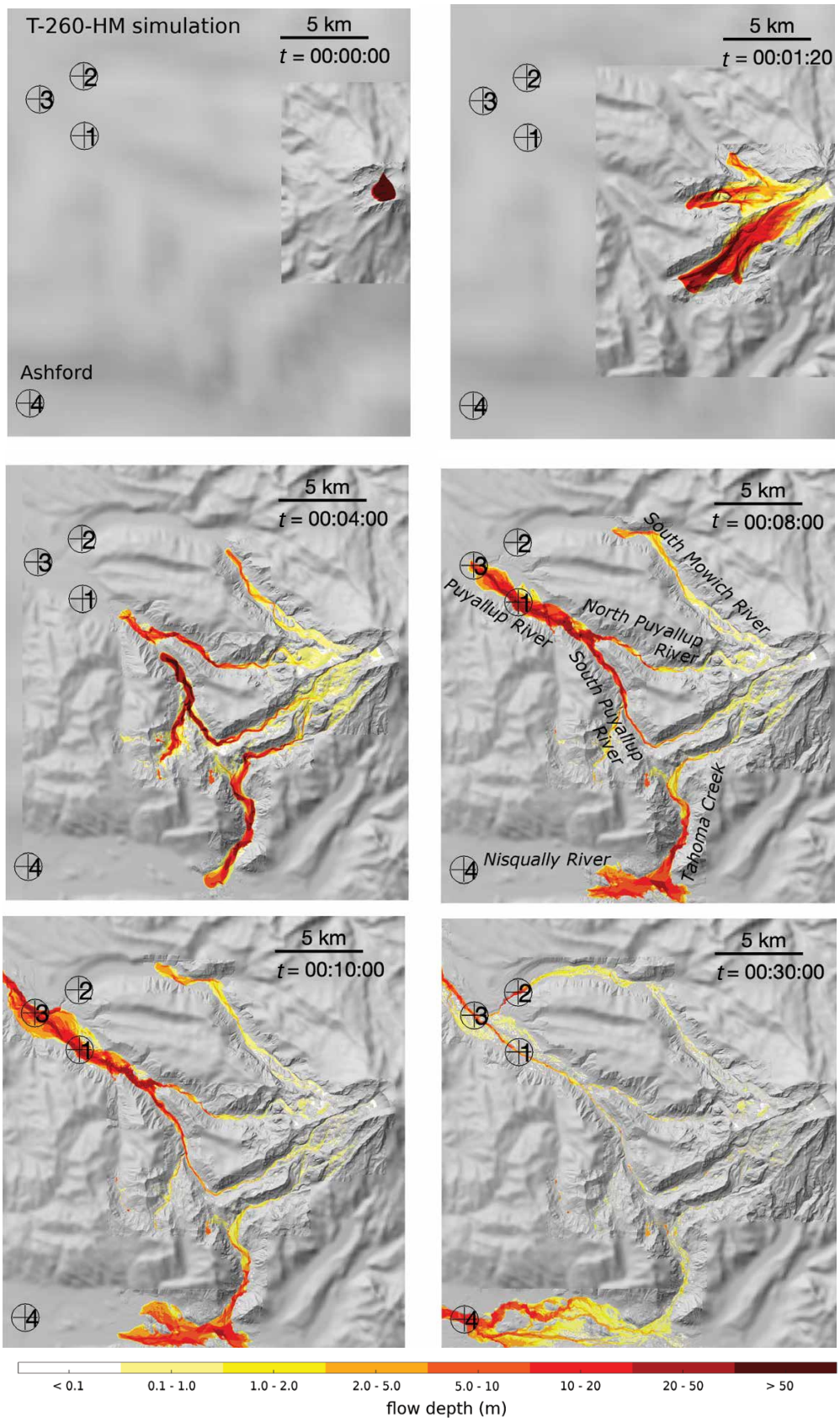

Figure 17. Shaded relief maps showing landslide and lahar flow depths of the T-260-HM simulation at selected times during the first 30 minutes of lahar motion. Imagery appears blurry where lahar material is absent because D-Claw's adaptive mesh refinement (AMR) employs very coarse resolution in those areas. Successive frames show the landslide source area and the downstream flows, which descend into the Nisqually and Puyallup River valleys. The southernmost flow in the Tahoma Creek tributary reaches the Mount Rainier National Park boundary about 10 minutes after the onset of motion, and it slows considerably as it reaches the broad Nisqually River floodplain upstream of the community of Ashford. Color shading indicates landslide and lahar flow depths in meters (m). Circled numbers are reference points for computed times series described in the "Lahar Speeds, Depths, and Discharges at Selected Locations" section. Time (*t*) is indicated in hours:minutes:seconds. km, kilometers.

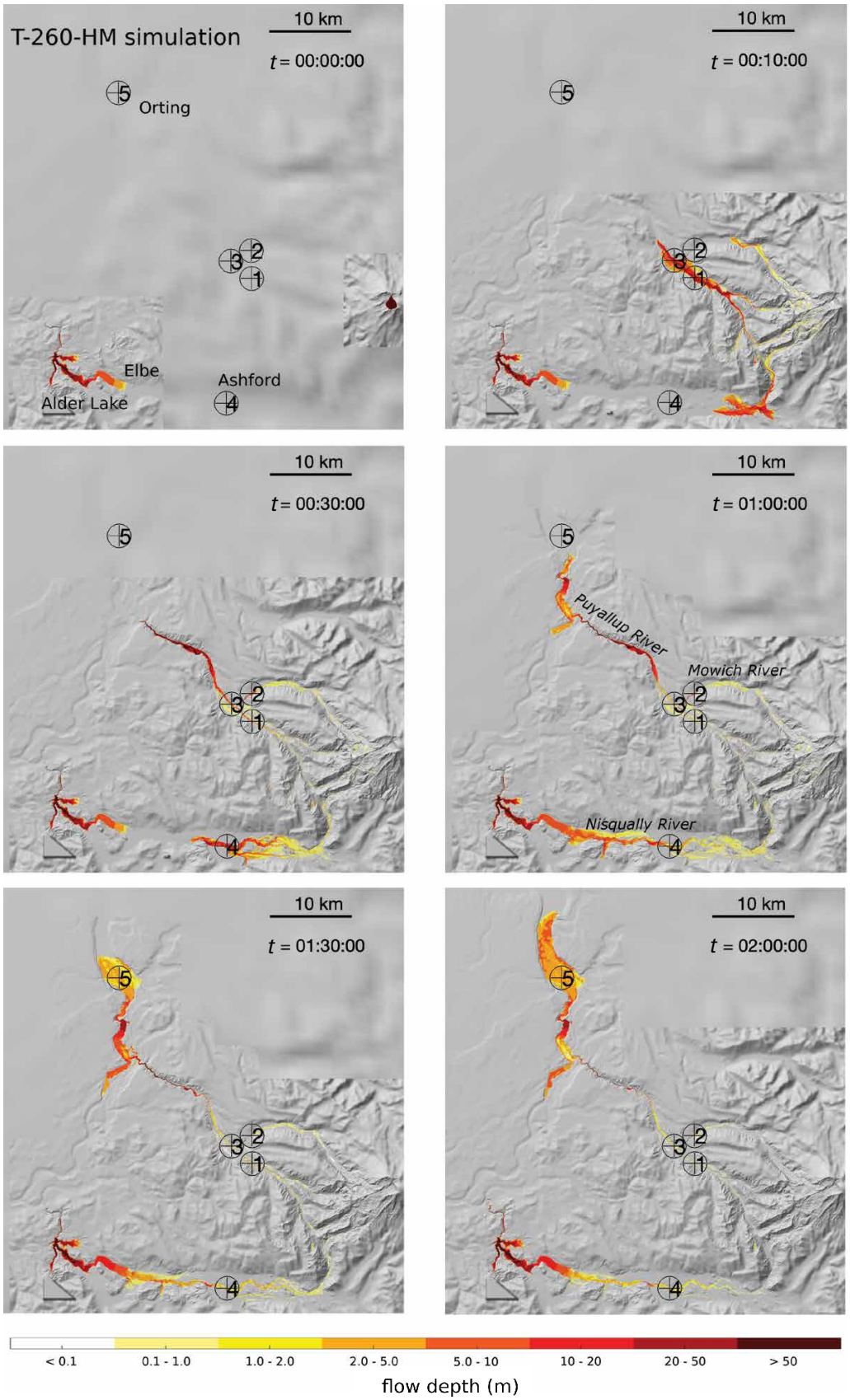

Figure 18. Shaded relief maps showing landslide and lahar flow depths of the T-260-HM simulation at selected times during the first 2 hours of lahar motion. Imagery appears blurry where lahar material is absent because D-Claw's adaptive mesh refinement (AMR) employs very coarse resolution in those areas. Color shading indicates landslide and lahar flow depths (as well as water depths in Alder Lake) in meters (m). Circled numbers are reference points for computed times series described in the "Lahar Speeds, Depths, and Discharges at Selected Locations" section. Time (*t*) is indicated in hours:minutes:seconds. km, kilometers. Supplemental animation available at https://doi.org/10.3133/ofr20211118.

Figure 19. Photograph showing Alder Dam, a 100-meter-high concrete dam on the Nisqually River, 40 kilometers downstream from Mount Rainier's summit. U.S. Geological Survey photograph by Richard Iverson, taken April 18, 2018.

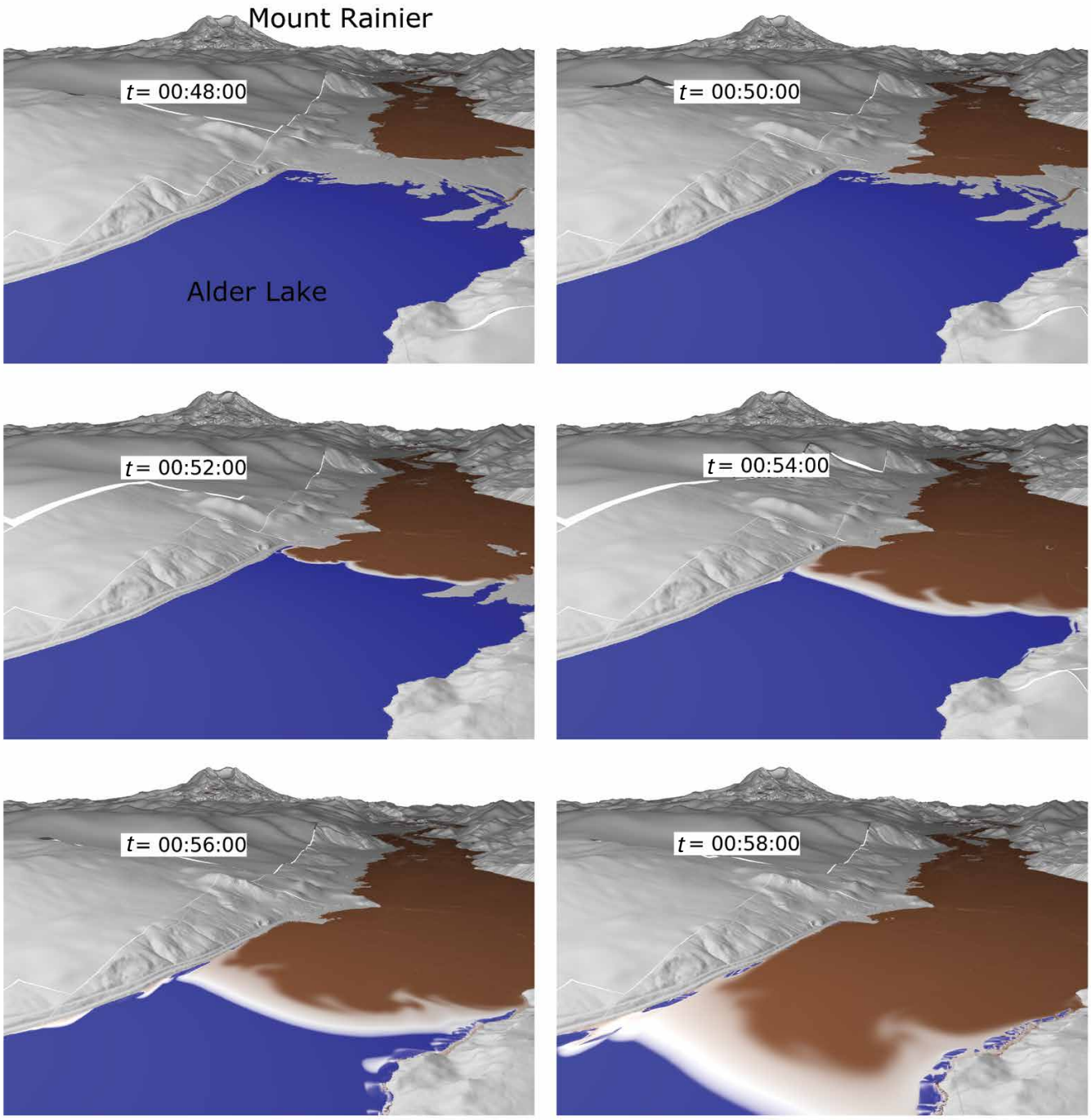

Figure 20. Oblique views of the T-260-HM simulation at selected times showing the lahar approaching and entering Alder Lake reservoir. The perspective is looking east in the upstream direction of the Nisqually River valley; Mount Rainier is visible on the horizon. As the lahar enters Alder Lake, mixing of the sediment-rich lahar (brown) and the lake water (blue) can be seen near the propagating interface between the two. Lighter colors are intermediate and reveal regions with varying degrees of sediment concentrations. Time (*t*) is indicated in hours:minutes:seconds. Supplemental animation available at https://doi.org/10.3133/ofr20211118.

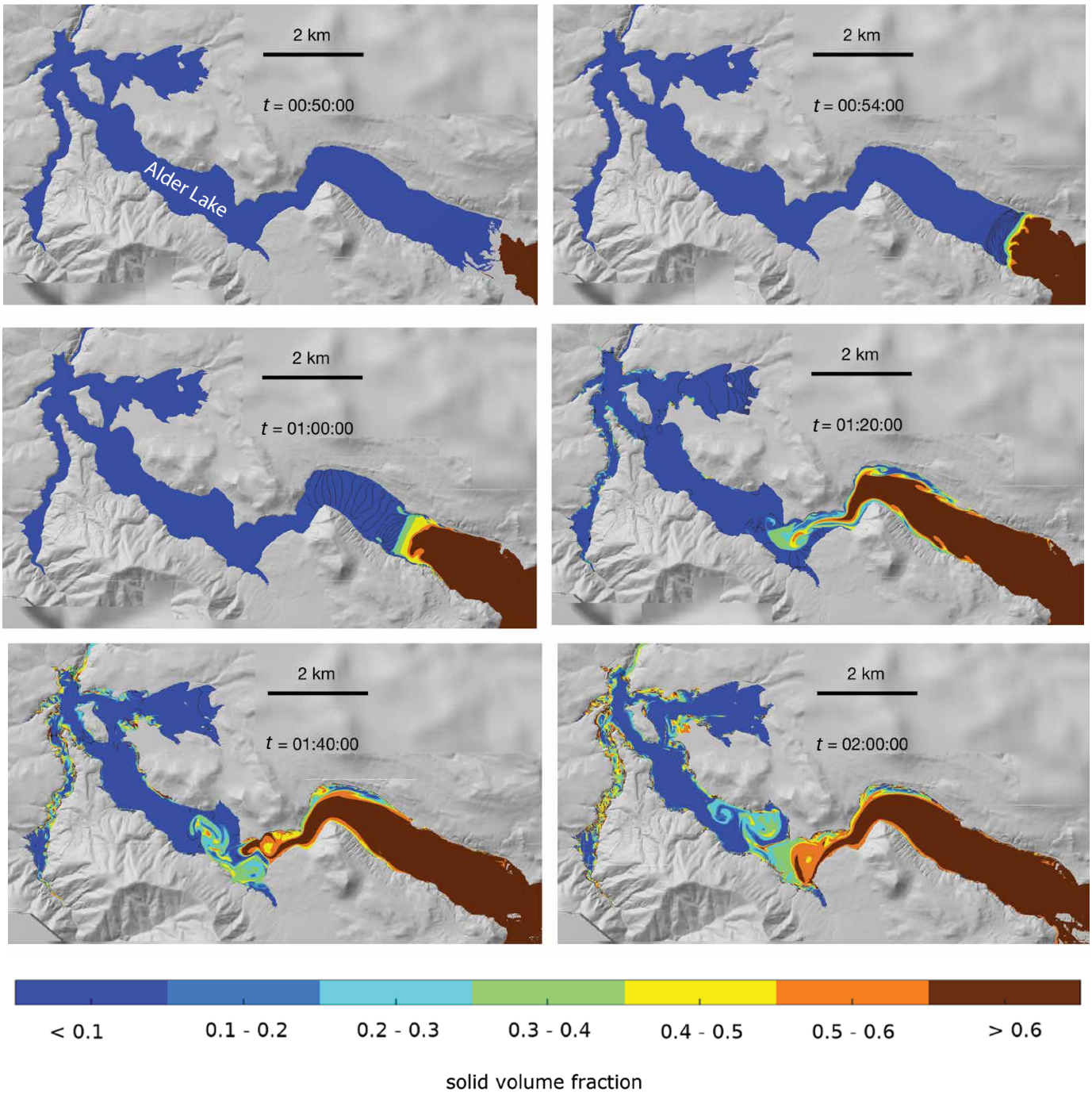

Figure 21. Shaded relief maps showing solid volume fractions (that is, volumetric sediment concentrations) of the T-260-HM simulation at selected times as the lahar enters Alder Lake reservoir and mixes with lake water. Color scale indicates the solid-volume fraction (m). As lahar material ($m \approx 0.6$) enters the lake, a region of mixing near the interface of the lahar and pure lake water propagates into the reservoir. Time is indicated by t in hours:minutes:seconds. km, kilometers. Supplemental animation available at https://doi.org/10.3133/ofr20211118.

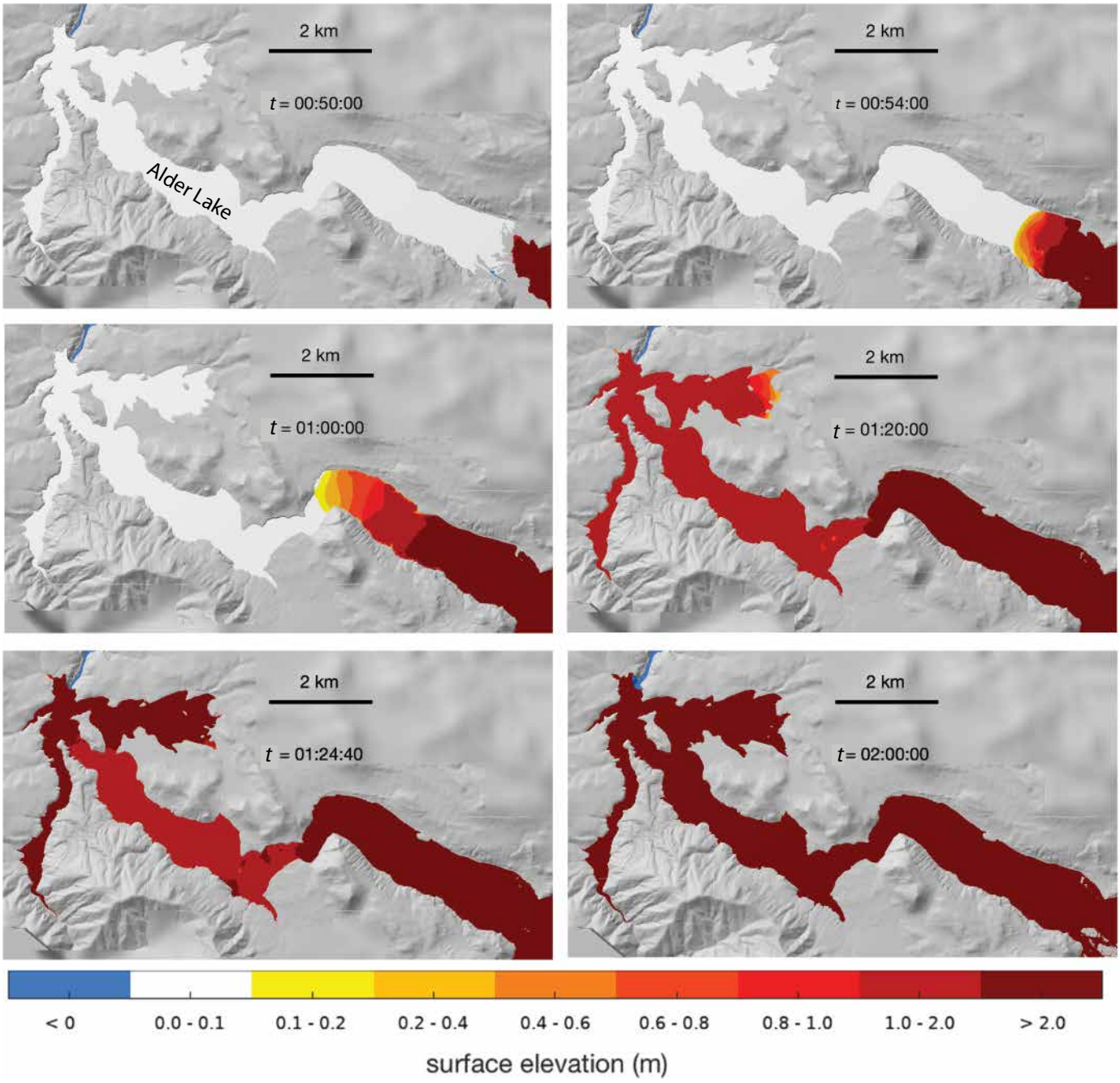

Figure 22. Shaded relief maps showing surface elevations of the T-260-HM simulation at selected times as the lahar enters Alder Lake reservoir and causes water levels to rise. The color scale indicates surface elevations in meters (m) relative to the undisturbed lake surface elevation (364 m above sea level in this simulation). The rising water level advances in front of the mixing region and travels faster than the solid lahar material—behavior that is revealed by comparing figures 21 and 22. Time (*t*) is indicated in hours:minutes:seconds. km, kilometers. Supplemental animation available at https://doi.org/10.3133/ofr20211118.

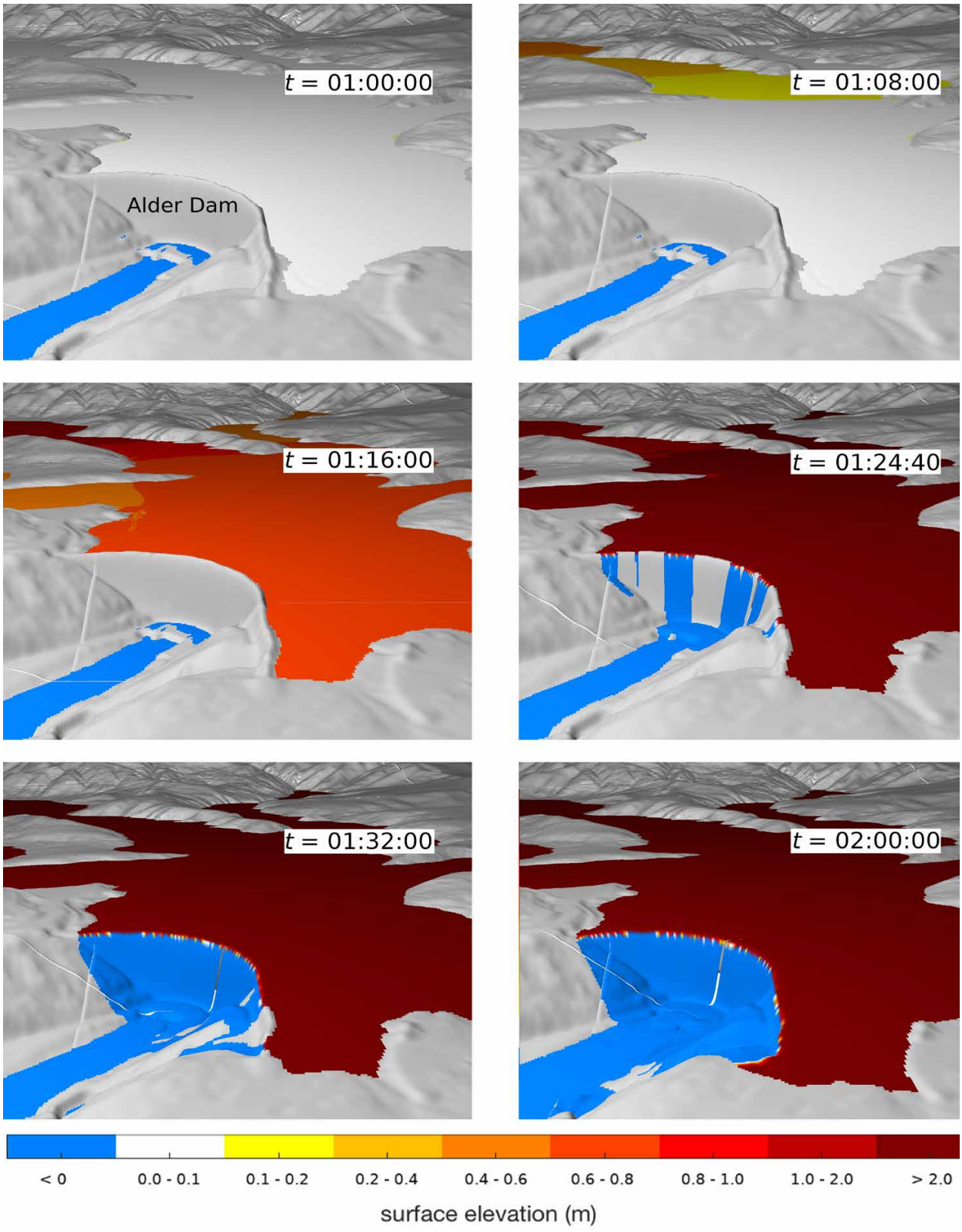

Figure 23. Oblique views of the T-260-HM simulation at selected times showing water surface elevations relative to the undisturbed lake surface elevation as a swell of lahar-displaced water approaches and eventually overtops Alder Dam. The perspective is looking south toward Alder Dam and Alder Lake. The color scale indicates surface elevations in meters (m) relative to the undisturbed lake surface elevation (364 m above sea level in this simulation). Just prior to time *t*=01:24:00, rising water levels and incoming waves cause dam overtopping, which continues until the simulation ends at *t*=2 hours. Time (*t*) is indicated in hours:minutes:seconds. Supplemental animation available at https://doi.org/10.3133/ofr20211118.

Lahars of Smaller Volume and Lower Mobility

Low-Mobility 260 Mm^3 Lahars

The landslide sources described above for our worst-case scenarios were also modeled with material having greater initial hydraulic permeability, k_0 (table 1). Greater permeability diminishes simulated landslide and lahar mobility by reducing the propensity and persistence of liquefaction and consequently increasing the effects of friction. The resulting landslides, initialized in the same fashion as the high-mobility landslides (that is, by increasing the basal pore-fluid pressure until the onset of slope failure), produced low-mobility lahars that we refer to as S-260-LM and T-260-LM. Just downslope from the source region, the geometry and location of these landslides led to flow paths like those of the high-mobility lahars. However, decaying pore pressure and higher basal friction prevented the low-mobility lahars from proceeding far enough downstream to enter the low-lying valleys and communities along the Puyallup and Nisqually Rivers.

The low-mobility lahars we consider here represent behavior that is transitional between that of fully liquefied debris flows and partially liquefied debris avalanches. A prominent example of a partially liquefied debris avalanche was the 2.3 billion m^3 rockslide-debris avalanche that removed the summit of Mount St. Helens, Washington, in 1980 and buried an approximately 23 km reach of the North Fork Toutle River valley. A more mobile lahar, representing approximately 10 percent of the volume of the debris avalanche, issued from the distal end of the avalanche deposit and traveled much farther downstream. Our simulations do not explicitly address such hybrid events. However, our simulations of low-mobility lahars predict a limited extent of inundation that contrasts with the more widespread inundation from highly liquefied flows.

The simulated S-260-LM lahar initially moves rapidly down the sides of Mount Rainier and into the headwaters of the Puyallup and Mowich Rivers (fig. 24). However, the northernmost branch of the lahar in the South Mowich River stalls upstream of the confluence between the Mowich and Puyallup Rivers. The lahar that bifurcated into the South Puyallup and North Puyallup Rivers merges downstream at their confluence, but attenuates and forms deposits just downstream of the confluence with the Mowich River. As shown in figure 24, the flows begin to form deposits after about 10 minutes because the pore-fluid pressure in the material decreases much more quickly than in the high-mobility scenario (S-260-HM).

The simulated T-260-LM flow arising from the Tahoma Glacier headwall bifurcates and enters the headwaters of the Puyallup and Nisqually Rivers (fig. 25). Each of the two flow branches attenuates and forms deposits after approximately 10 minutes, soon after entering the flatter upstream reaches of the Puyallup and Nisqually River valleys.

These results indicate that, even given identical landslide source geometries, variability in lahar composition (represented by differing values of hydraulic permeability; see table 1) greatly affects the downstream flow mobility, arrival times, extent of lowland inundation, and associated hazards.

High-Mobility 52 Mm^3 Lahars

We also constructed smaller hypothetical landslide source areas located within the regions of the 260 Mm^3 sources but commensurate with 52 Mm^3 landslides. For these smaller landslides, we first consider the high-mobility, mostly liquefied flows resulting from a debris permeability value of $k_0=10^{-11}$ m^2 (scenarios S-52-HM and T-52-HM; fig. 26).

The initial flow paths of the simulated S-52-HM and T-52-HM lahars are like those in the previously described scenarios, in that both source regions produce substantial volumes of material flowing into the Puyallup River valley (fig. 27). For both the S-52-HM and T-52-HM scenarios, the flows in the south that reach the Nisqually River via Tahoma Creek stall in the broad valley between Ashford and Alder Lake. Comparison with the T-260-HM lahar's inundation of Alder Lake shows that the smaller volume (52 Mm^3) of material is insufficient to generate a far-traveling liquefied lahar within the broad valley, even though the material itself has high mobility owing to its low permeability (table 1). The 52 Mm^3 lahars traveling into the Puyallup River valley, however, exhibit more sustained motion as they descend the narrow Puyallup River canyon above the broader lowland areas near Orting and beyond (lower panels of figs. 27 and 28). The extent of inundation in the valley surrounding Orting, although less than that from the 260 Mm^3 lahars, is substantial enough to warrant attention as a considerable hazard. The reduced speed of these smaller lahars is notable because of the resulting delay in their arrival at Orting relative to the 260 Mm^3 lahars (~2 hours vs. ~50 minutes; see the section "Lahar Speeds, Depths, and Discharges at Selected Locations").

Low-Mobility 52 Mm^3 Lahars

We next consider the smaller volume landslide sources with a higher initial permeability and the consequent lower mobility (simulations S-52-LM and T-52-LM). Unsurprisingly, these simulations result in the most limited downstream inundation among the considered scenarios. Like the larger low-mobility flows (S-260-LM and T-260-LM), the lahars attenuate quickly, forming deposits within several minutes after the onset of slope failure (figs. 29 and 30). Because of the low mobility and relatively small volume of lahar material, the flows do not extend far beyond the steep drainages on the sides of Mount Rainier.

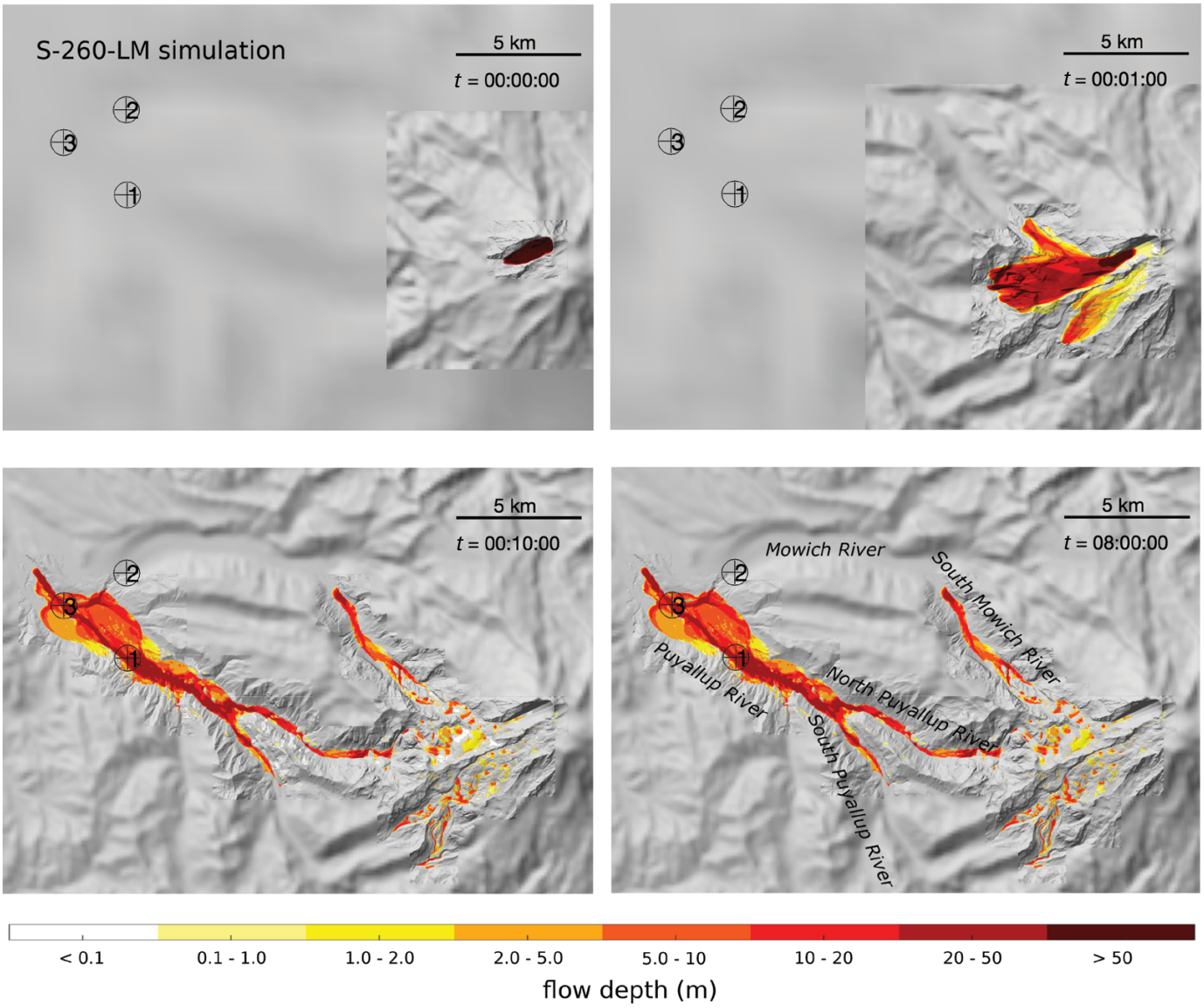

Figure 24. Shaded relief maps showing landslide and lahar flow depths of the S-260-LM simulation at selected times. Imagery appears blurry where lahar material is absent because D-Claw's adaptive mesh refinement (AMR) employs very coarse resolution in those areas. The lahar proceeds into the Puyallup River headwaters and eventually the main fork of the Puyallup River, where it stalls near the confluence of the Puyallup and Mowich Rivers about 25–30 kilometers upstream of Orting. Color shading indicates landslide and lahar flow depths in meters (m). Circled numbers are reference points for computed times series described in the "Lahar Speeds, Depths, and Discharges at Selected Locations" section. Time (*t*) is indicated in hours:minutes:seconds. km, kilometers. Supplemental animation available at https://doi.org/10.3133/ofr20211118.

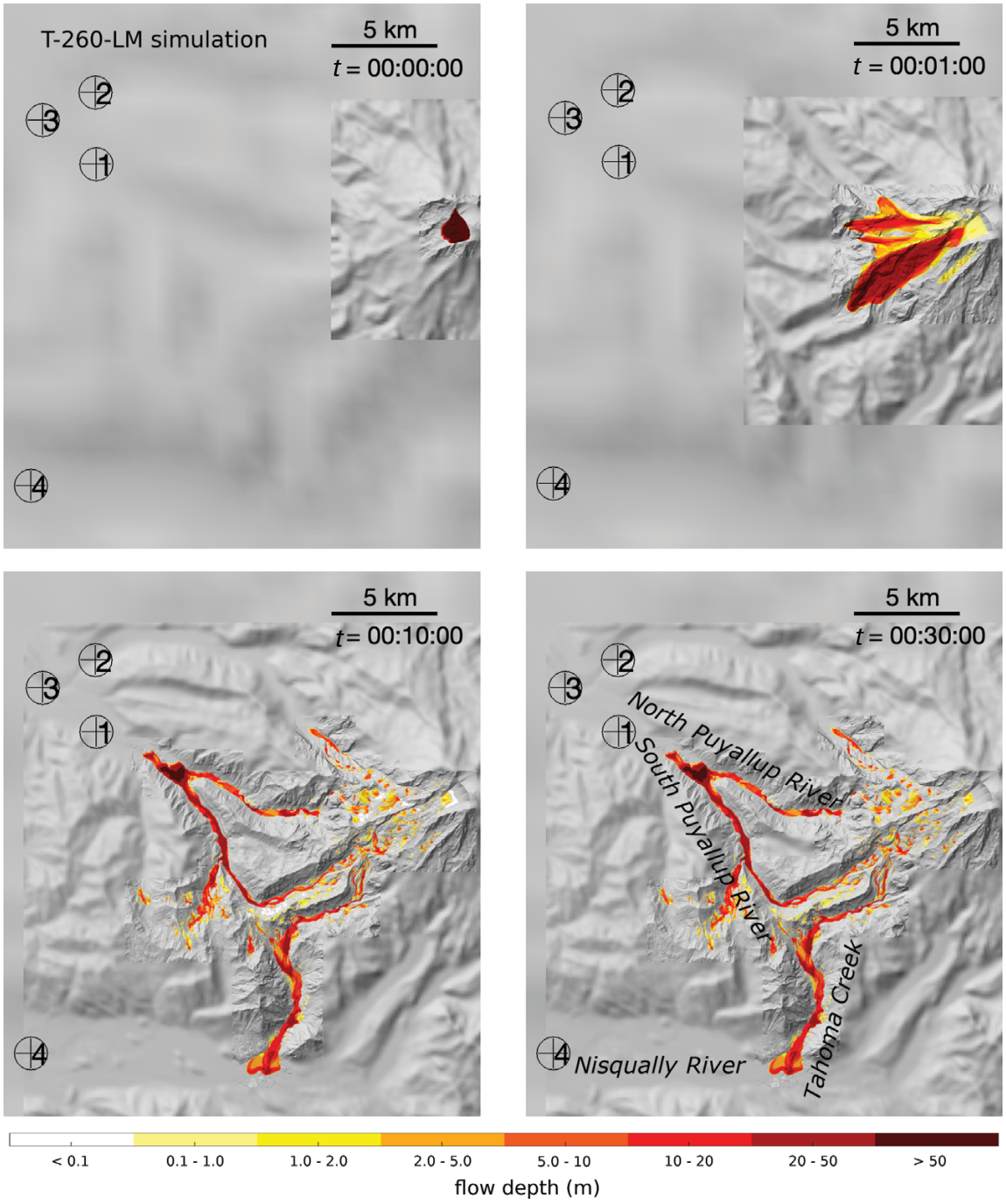

Figure 25. Shaded relief maps showing landslide and lahar flow depths of the T-260-LM simulation at selected times. Imagery appears blurry where lahar material is absent because D-Claw's adaptive mesh refinement (AMR) employs very coarse resolution in those areas. Substantial fractions of the landslide material descend into the Puyallup and Nisqually River drainages, yet both lahars stall a relatively short distance downstream from the steep west side of Mount Rainier. Color shading indicates landslide and lahar flow depths in meters (m). Circled numbers are reference points for computed times series described in the "Lahar Speeds, Depths, and Discharges at Selected Locations" section. Time (*t*) is indicated in hours:minutes:seconds. km, kilometers. Supplemental animation available at https://doi.org/10.3133/ofr20211118.

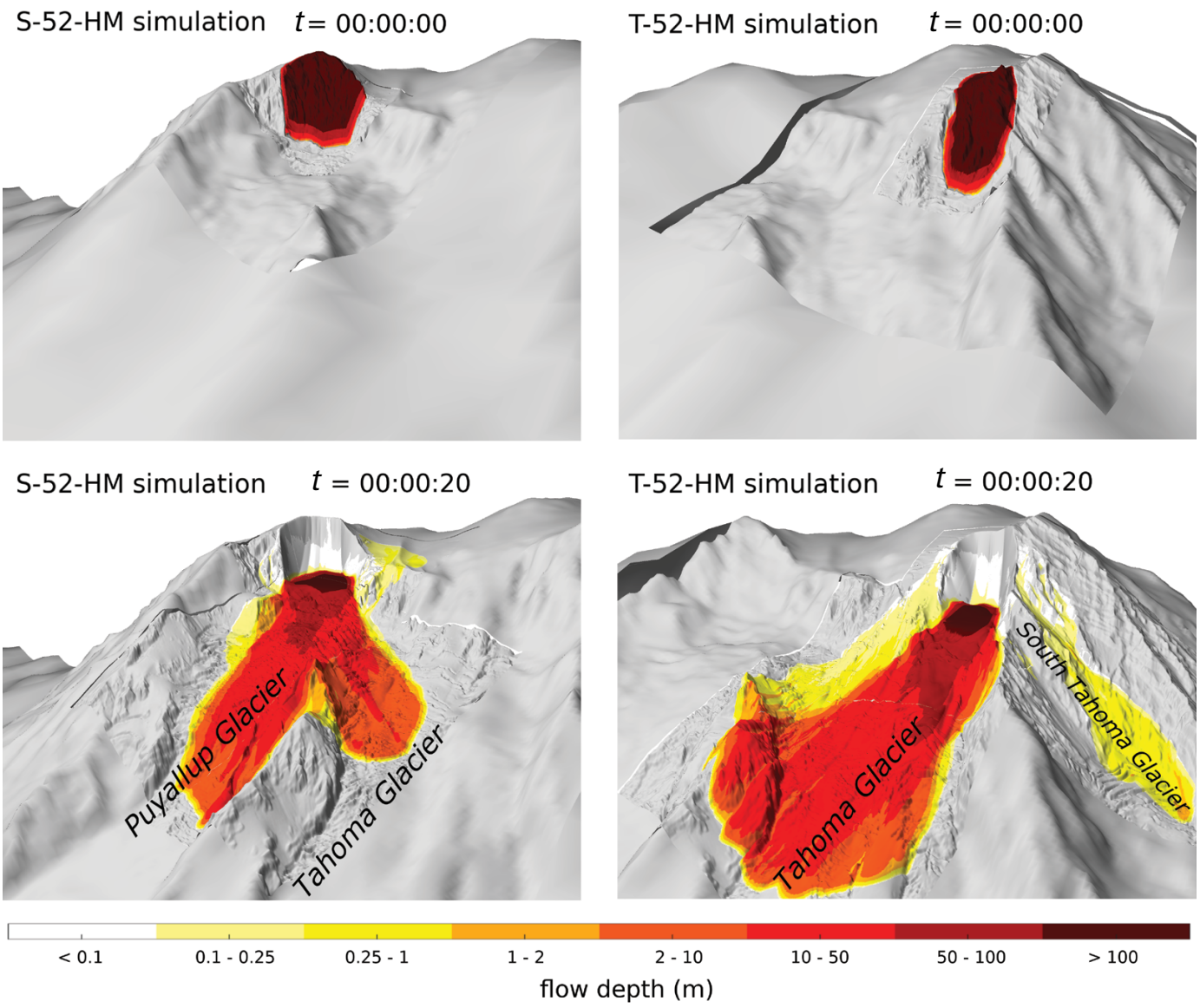

Figure 26. Close-up oblique views of Mount Rainier's upper west side showing landslide and lahar flow depths of the small-volume, high-mobility lahar simulations S-52-HM (*left*) and T-52-HM (*right*) before (*top*) and 20 seconds after (*bottom*) the onset of slope failure. Color shading indicates landslide and lahar flow depths in meters (m). Time (*t*) is indicated in hours:minutes:seconds. Supplemental animation available at https://doi.org/10.3133/ofr20211118.

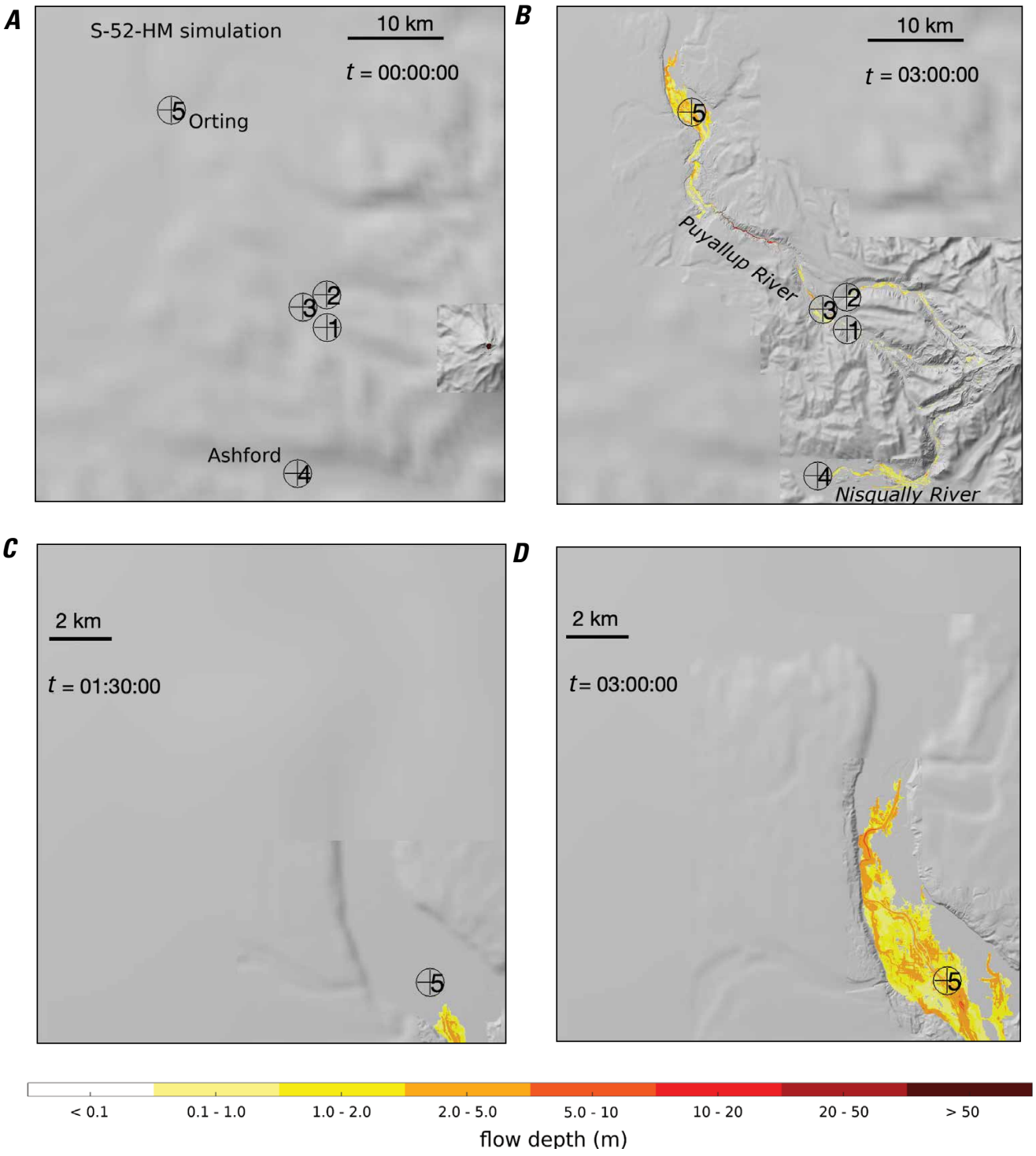

Figure 27. Shaded relief maps showing landslide and lahar flow depths of the S-52-HM simulation at selected times for the full spatial extent of the simulation (*A*, *B*) and focused on the valley bottom surrounding Orting (*C*, *D*). Imagery appears blurry where lahar material is absent because D-Claw's adaptive mesh refinement (AMR) employs very coarse resolution in those areas. The high mobility of the lahars leads to substantial inundation near Orting (centered near gauge 5 marked with a circle and crosshairs). However, the arrival time in Orting of these volumetrically smaller lahars, relative to those with 260-million-cubic-meter sources, is delayed. Color shading indicates landslide and lahar flow depths in meters (m). Circled numbers are reference points for computed times series described in the "Lahar Speeds, Depths, and Discharges at Selected Locations" section. Time (*t*) is indicated in hours:minutes:seconds. km, kilometers. Supplemental animation available at https://doi.org/10.3133/ofr20211118.

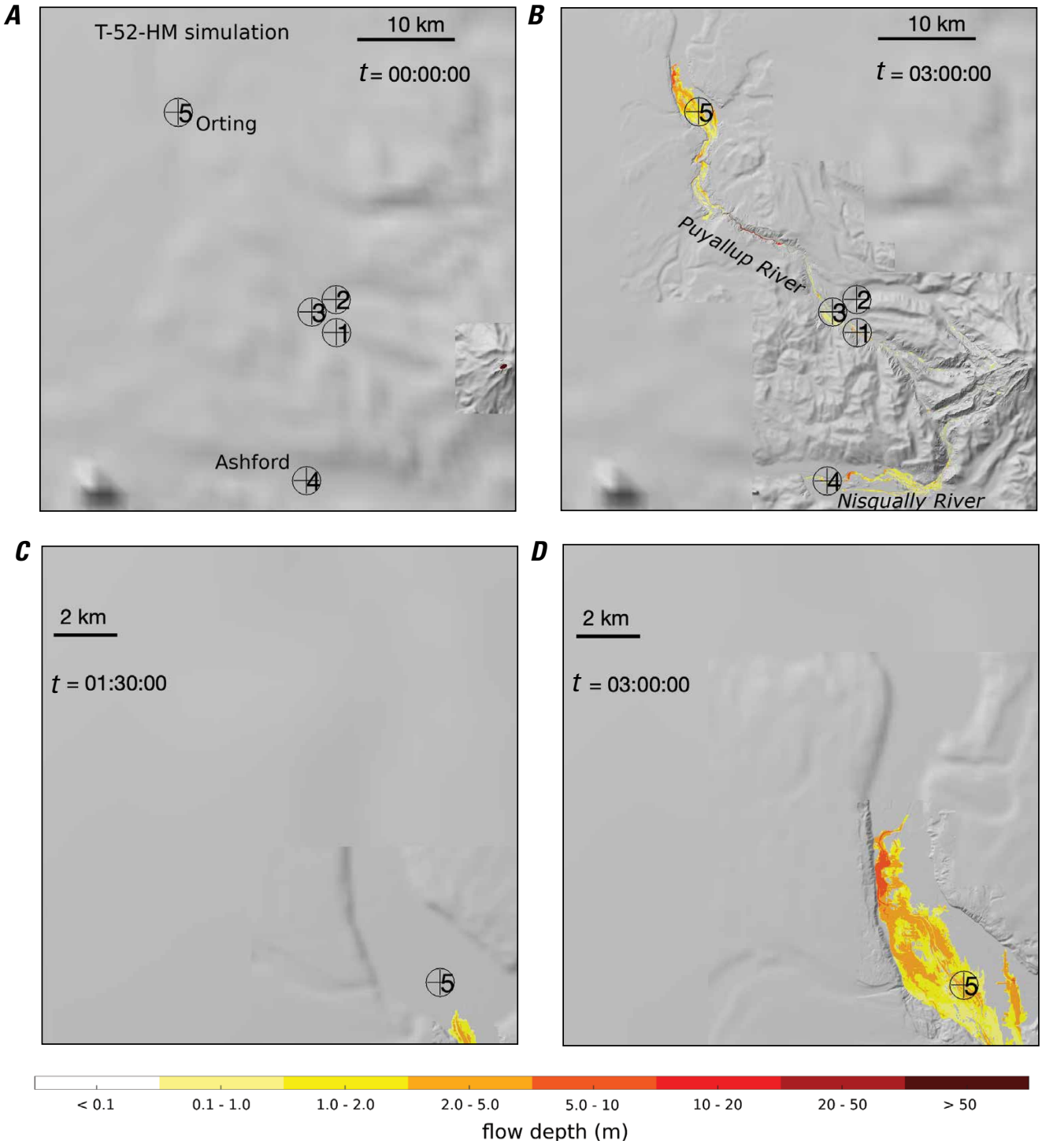

Figure 28. Shaded relief maps showing landslide and lahar flow depths of the T-52-HM simulation at selected times for the full spatial extent of the simulation (*A*, *B*) and focused on the valley bottom surrounding Orting (*C*, *D*). Imagery appears blurry where lahar material is absent because D-Claw's adaptive mesh refinement (AMR) employs very coarse resolution in those areas. The T-52-HM simulation produces a lahar in the Orting area (*C*, *D*) similar to that of the S-52-HM simulation (shown in fig. 27). Color shading indicates landslide and lahar flow depths in meters (m). Circled numbers are reference points for computed times series described in the "Lahar Speeds, Depths, and Discharges at Selected Locations" section. Time (*t*) is indicated in hours:minutes:seconds. km, kilometers. Supplemental animation available at https://doi.org/10.3133/ofr20211118.

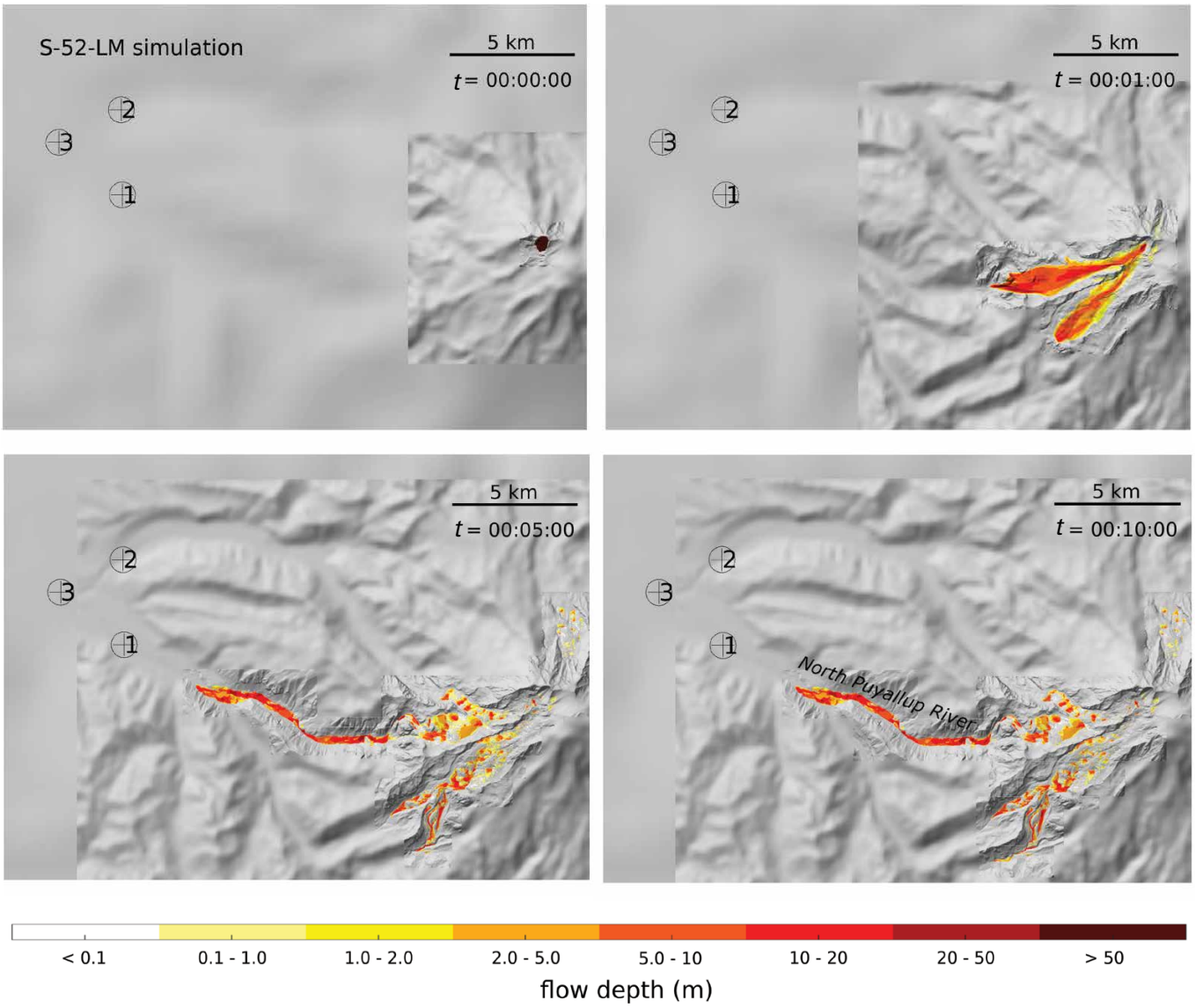

Figure 29. Shaded relief maps showing landslide and lahar flow depths of the S-52-LM simulation at selected times. Imagery appears blurry where lahar material is absent because D-Claw's adaptive mesh refinement (AMR) employs very coarse resolution in those areas. The flow stalls and begins to form deposits after several minutes. Color shading indicates landslide and lahar flow depths in meters (m). Circled numbers are reference points for computed times series described in the "Lahar Speeds, Depths, and Discharges at Selected Locations" section. Time (*t*) is indicated in hours:minutes:seconds. km, kilometers.

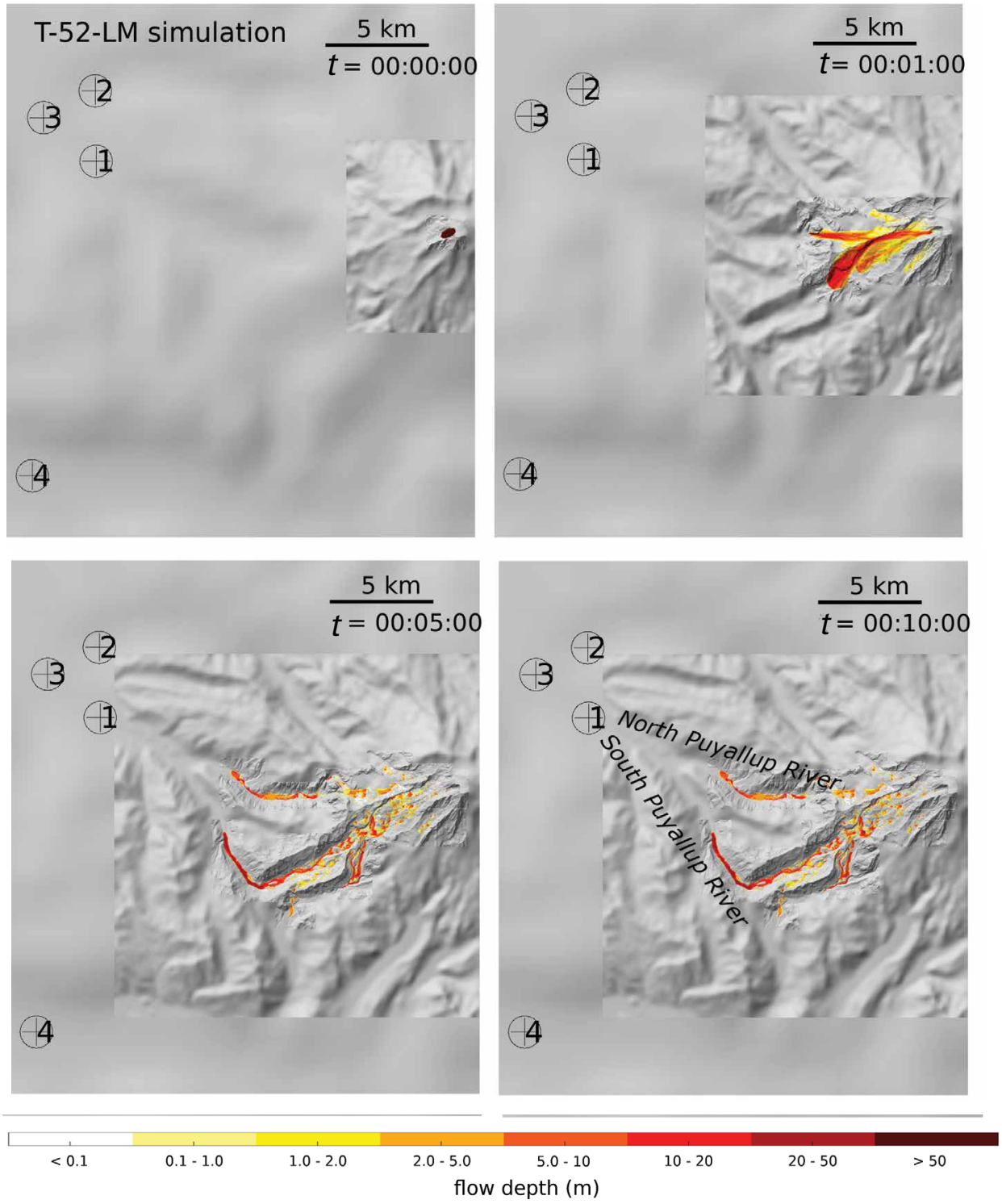

Figure 30. Shaded relief maps showing landslide and lahar flow depths of the T-52-LM simulation at selected times. Imagery appears blurry where lahar material is absent because D-Claw's adaptive mesh refinement (AMR) employs very coarse resolution in those areas. The flow stalls and begins to form deposits after several minutes. Color shading indicates landslide and lahar flow depths in meters (m). Circled numbers are reference points for computed times series described in the "Lahar Speeds, Depths, and Discharges at Selected Locations" section. Time (*t*) is indicated in hours:minutes:seconds. km, kilometers.

Lahar Speeds, Depths, and Discharges at Selected Locations

We augment the simulation results by presenting time series output of the simulations to reveal and compare the evolving lahar dynamics in greater detail at selected locations. We refer to these locations as gauges, numbered 1–8, although no measuring stations are actually present at these locations in the field (fig. 31 and table 4). We also present the flow discharges (volume fluxes) and cumulative volumes that pass through cross-flow transects in order to compare the different scenarios in each river valley. These quantities are computed at transect locations denoted by Γ (fig. 31 and table 5).

S-260-HM Simulation

Although the simulated S-260-HM lahar primarily affects the Puyallup River valley, it produces a multi-branched flow with some material descending into the Nisqually River system via Tahoma Creek. However, the discharge and volume through transects Γ_{Nisq} and Γ_{Puy} (fig. 31) illustrate that the Nisqually River branch constitutes a negligible fraction of the total flow volume (fig. 32). In fact, nearly 200 of the 260 Mm^3 of source material reaches the main fork of the Puyallup River, crossing transect Γ_{Puy} downstream from gauge 3. At this location, the total peak discharge approaches 250,000 cubic meters per second (m^3/s) within 15 minutes after the onset of slope failure, not long after the leading flow-front arrives. To place this value in perspective, it is approximately 30 times larger than the typical discharge of the Columbia River in Vancouver, Washington.

Below several confluences of major Puyallup River tributaries, separate flow branches from the S-260-HM source merge into a deep and fast moving lahar in the main fork of the Puyallup River valley, with a leading flow front exceeding 50 m deep and traveling at about 60 m/s (~130 mi/hr) at gauge 3 (fig. 33). Comparing values of $||hv||$ (the magnitude of the depth, h, multiplied by the flow velocity, v, which is equivalent to the depth-integrated volume-flux density—the discharge per unit width) at gauges 1–3 reveals that most of the material arriving at gauge 3 followed the main Puyallup River fork from upstream (gauge 1), with less flow coming from the Mowich River valley (gauge 2).

After rapidly flowing down the upper Puyallup River valley to emerge on the broader, low-gradient valley floor, the lahar slows considerably (to speeds less than 5 m/s [10 mi/hr]) (gauges 5–7; fig. 34). After arriving in the Orting area, a slow-moving flow several meters thick persists for several hours (t≈1–5 hours) before decelerating and halting at t≈5 hours, leaving an approximately 2.5-m-thick deposit at gauge 5 (fig. 34). The slowly progressing flow front arrives farther downstream at the communities of Sumner and Puyallup (gauges 6–7) at t≈3–4 hours, with greatly reduced speeds ($||v||$ <1 m/s). However, inundation depths increase downstream of Orting in the slightly narrowed Puyallup River valley directly to the north, with maximum depths observed farther north upstream into the White River valley at Sumner (h≈8 m, gauge 6; fig. 34). The greater flow depths result in part from the accumulation of material arriving behind the slowed flow front, as well as from backwater effects as the lahar deceleration extends upvalley. The gradual influx of material from the south leads to a sustained increase in depth (pooling) with negligible flow velocity and discharge over approximately 1.5 hours

Table 4. Gauge locations for time series output.

Gauge	Location coordinates[1] in meters (east, north)	Description
1	(576388, 5192400)	Puyallup River, upstream of Mowich River confluence
2	(576345, 5195800)	Mowich River, upstream of Puyallup River confluence
3	(573850, 5194500)	Puyallup River, downstream of Mowich River confluence
4	(573300, 5177200)	Nisqually River, upstream of Alder Lake
5	(560200, 5215000)	Orting, Washington
6	(557900, 5229700)	Sumner, Washington
7	(552900, 5227200)	Puyallup, Washington
8	(546400, 5231370)	Alder Lake, upstream of Alder Dam

[1]Universal Transverse Mercator zone 10, North American Datum of 1983 (see section "Digital Elevation Models").

Table 5. Cross-flow transect locations for time series output.

Transect	Endpoint coordinates[1] in meters (east, north)—(east, north)	Description
Γ_{Puy}	(569600, 5200000)—(569600, 5202000)	Puyallup River, downstream of Mowich River confluence
Γ_{Nisq}	(584500, 5178000)—(585500, 5177000)	Tahoma Creek-Nisqually River confluence
Γ_{Alder}	(561500, 5178000)—(561500, 5180000)	Nisqually River, head of Alder Lake
$\Gamma_{AboveDam}$	(552400, 5183500)—(552800, 5183300)	Alder Lake, above Alder Dam[2]
$\Gamma_{BelowDam}$	(552500, 5183650)—(552900, 5183300)	Nisqually River, below Alder Dam[2]

[1]Universal Transverse Mercator zone 10, North American Datum of 1983 (see section "Digital Elevation Models").

[2]Not shown on figure 31.

(within the interval t≈3–5 hours, gauge 6; fig. 34). Lahar material also extends farther down the Puyallup River valley and turns west toward the community of Puyallup. However, the attenuating downstream momentum results in slow spreading in the surrounding valley, with the lahar material halting quickly after its arrival (t≈4–5 hours) and leaving approximately 2-m-thick deposits at gauge 7 (fig. 34).

It is noteworthy that lahar deposition occurs almost contemporaneously (at t≈4–5 hours; fig. 34) in the downstream valleys surrounding Orting, Sumner, and Puyallup rather than at times that are consistent with the differing downstream distances from the steep source areas and which simple momentum considerations might suggest. Deposition of the simulated lahar occurs when the material, which remained liquefied for many (~5) hours because of its low permeability and consequently long timescale of pore-fluid pressure relaxation, begins to lose pore-fluid pressure and hence mobility.

The advance of the lahar upstream into the White River valley near Sumner, as well as its slow spreading into the valleys around Puyallup, should be viewed with a degree of caution because depositional processes such as particle settling and fluid drainage are neglected in the D-Claw simulations. Generally, model results for low-velocity flows on low-gradient terrain that proceed for many hours are subject to considerable uncertainty owing to their sensitivity to model parameter values. Deposits of similar-sized prehistoric lahars (for example, the Electron Mudflow) are absent downstream of Sumner (Vallance and Scott, 1997; Sisson and Vallance, 2009), although the absence of preserved lahar deposits in a location does not necessarily imply an absence of past flows.

T-260-HM Simulation

Unlike the S-260-HM simulation, which results in most of the flow entering the Puyallup River valley, the simulated T-260-HM lahar originating from the Tahoma Glacier headwall leads to substantial fractions of material in both the Puyallup and Nisqually River valleys (~130 and ~80 Mm^3, respectively; fig. 35). In fact, it is the only scenario considered that results in substantial flow in the Nisqually River valley downstream of Tahoma Creek, leading to debris entering Alder Lake. The Nisqually River branch of the T-260-HM flow reaches the Mount Rainier National Park Nisqually entrance and Ashford in less than 20 minutes (fig. 36).

The Nisqually branch of the T-260-HM lahar has somewhat greater depths and speeds in the Nisqually River valley (gauge 4; fig. 36) than those of the S-260-HM lahar in the lower Puyallup River valley (fig. 34). Furthermore, the peak discharge rate of the T-260-HM flow entering the Nisqually River valley (~300,000 m^3/s at Γ_{Nisq}; fig. 35) exceeds that of the S-260-HM flow on the main fork of the Puyallup River (~250,000 m^3/s at Γ_{Puy}). However, the cumulative discharge or total volume is considerably greater for the latter case (~200 Mm^3 vs. ~80 Mm^3; fig. 35). These results are not surprising given the relative proximities of the transect locations Γ_{Nisq} and Γ_{Puy} to the landslide sources and steep slopes of Mount Rainier, which lead to a more sharply peaked but less sustained pulse of flow entering the Nisqually River for simulation T-260-HM.

As lahar material enters Alder Lake, it generates waves and subsequently continues to displace water, creating a slow rise in the lake level (fig. 37). Leading waves cause dam overtopping after t≈84 minutes (figs. 22, 23). However, it is clear from figure 37 that the lahar does not generate a substantial tsunami wave or seiche, but primarily contributes to a more gradual lake level rise as it displaces water at the upstream end of the lake. The simulated lake-surface elevation rises from its initial level (364 m elevation) to the simulated dam-crest elevation (~368 m, based on lidar DEM) over the course of about 35 minutes (from t≈70 to 105 minutes).

A calculation based on the approximately 12 Mm^2 surface area of Alder Lake implies that about 48 Mm^3 of lahar material enters the lake prior to dam overtopping in this simulation. The total discharge (volume flux) and cumulative discharge (total volume) of flow entering the lake at its head (Γ_{Alder}; fig. 31, tables 4 and 5) and above and below the dam ($\Gamma_{AboveDam}$ and $\Gamma_{BelowDam}$; table 4 and 5) are shown in figures 38 and 39. The volume differential of flow entering the lake versus overtopping the dam of course depends on the reserve capacity of the reservoir—determined by the initial surface elevation of the lake and the minimum dam-crest elevation. As noted previously, a detailed analysis of the dam overtopping process, dam resilience, and downstream effects are beyond the scope of this study. A full assessment would require a more detailed representation of the dam, adjacent terrain, and detailed flow features near the dam.

Comparison of Lahars at Selected Locations

Finally, we directly compare the different high-mobility flow simulations at several locations. The total discharge and flow volumes in each basin for the two worst-case scenarios are compared in figures 40 and 41. Only the T-260-HM scenario leads to substantial flow into the Nisqually River valley below Tahoma Creek, as described above. Comparisons of the high-mobility scenarios in the Puyallup River valley are shown in figures 42 and 43.

Although the larger sources of the 260 Mm^3 landslides generate larger and faster flows, all of the high-mobility scenarios (HM) cause substantial inundation in the Puyallup River valley near Orting (figs. 42 and 43). However, the smaller 52 Mm^3 scenarios do not fill the valley to the same extent as the 260 Mm^3 scenarios. The effect of these lower volume scenarios closer to Puget Sound are not addressed in this study owing to larger relative uncertainties associated with the slower depositional phase, including the interaction with river water. Note that in all cases illustrated in figures 30 and 31, lahars originating on the Tahoma Glacier headwall area travel more slowly down the Puyallup River valley than do their counterpart lahars originating on the Sunset Amphitheater. This difference arises in part because a substantial fraction of the lahar volume from the Tahoma Glacier headwall source is diverted into the Nisqually River valley via Tahoma Creek (figs. 40 and 41).

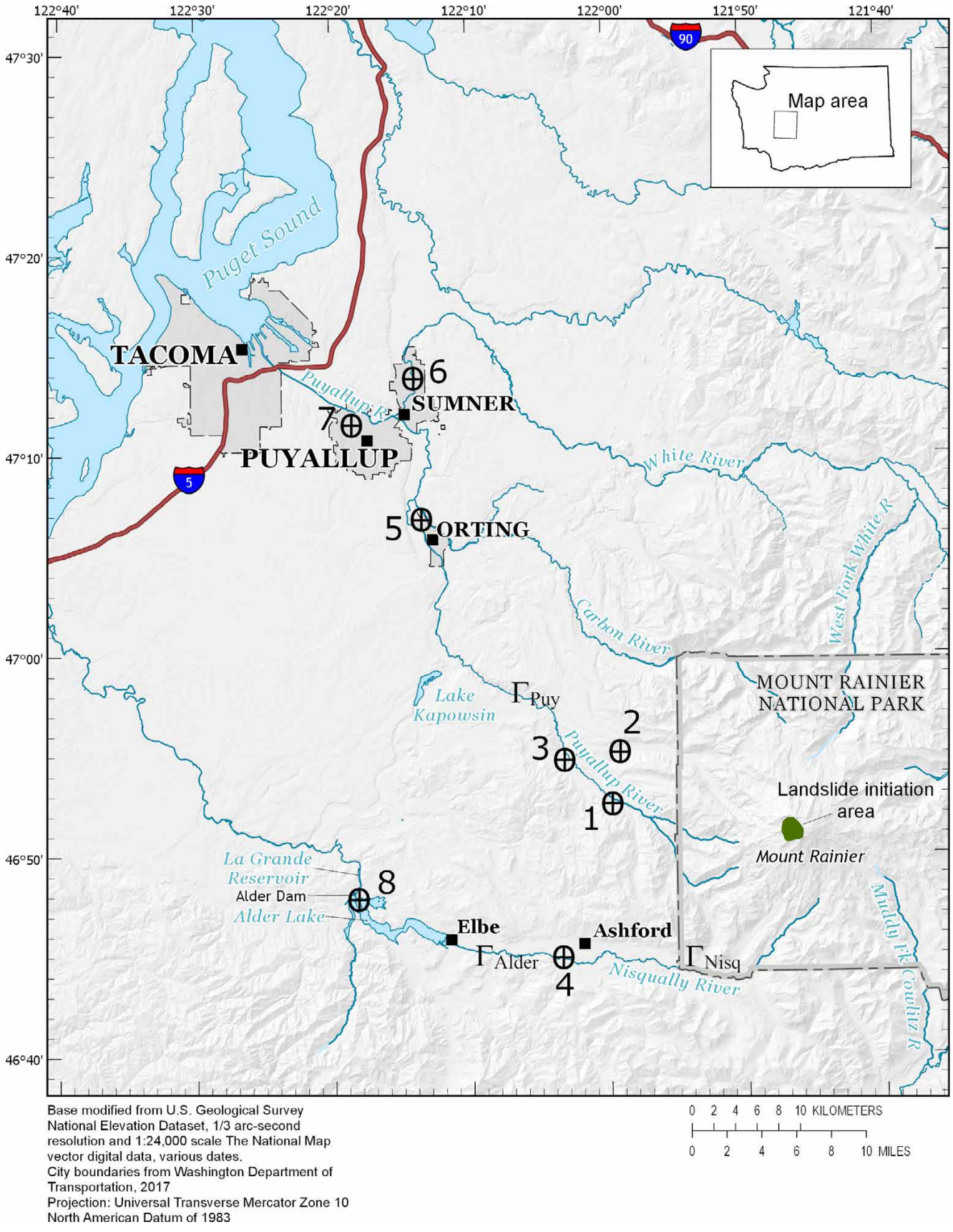

Figure 31. Shaded relief map of Mount Rainier and the surrounding area showing the location of time series output gauges and cross-flow transects. Gauges are denoted by circled crosshairs and numbered 1–8. Cross-flow transects are denoted by Γ. Location coordinates of gauges and transects are provided in tables 4 and 5.

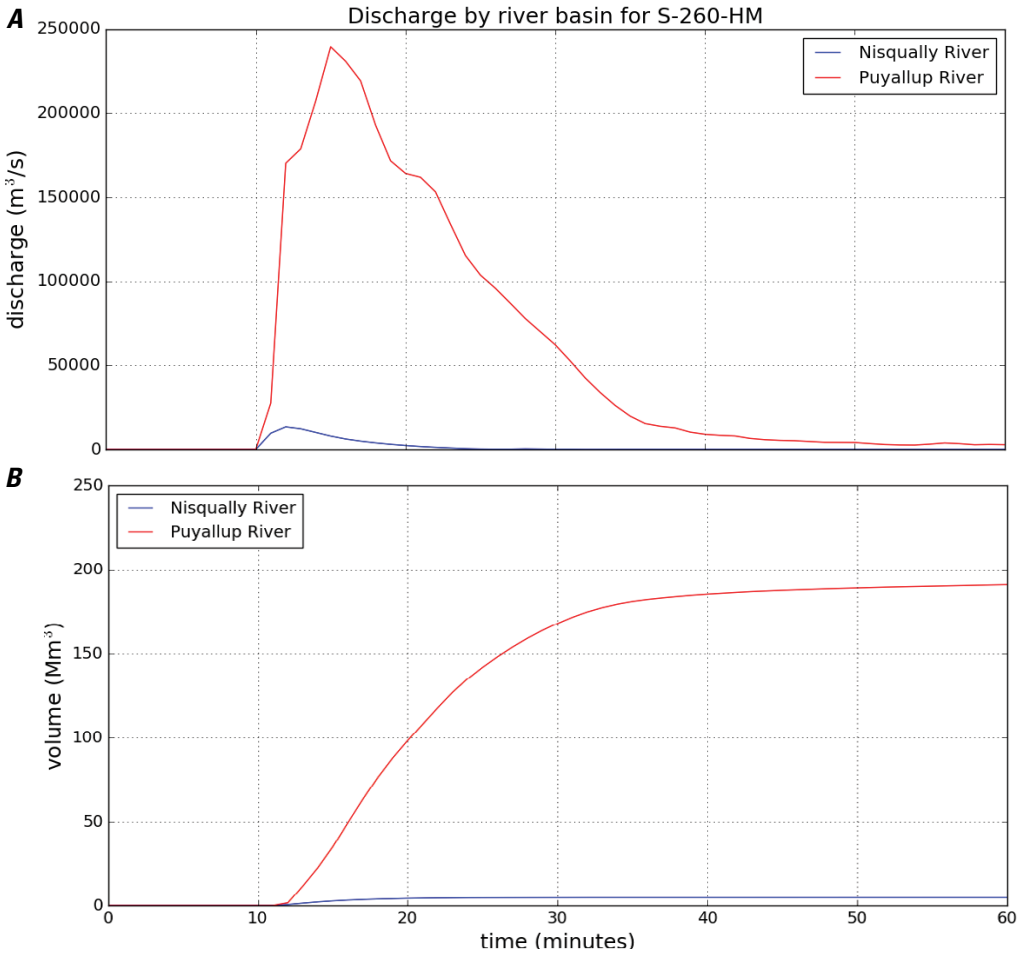

Figure 32. Graphs of time series output for the S-260-HM simulation lahar showing total flow discharge and total flow volume in the Puyallup and Nisqually River valleys. *A*, Total flow discharge (volume flux) in cubic meters per second (m^3/s) through transects Γ_{Puy} and Γ_{Nisq} (located along the Puyallup and Nisqually River valleys, respectively; see fig. 31). *B*, Cumulative (temporally integrated) discharge or total flow volume through the same transects. Mm^3, million cubic meters.

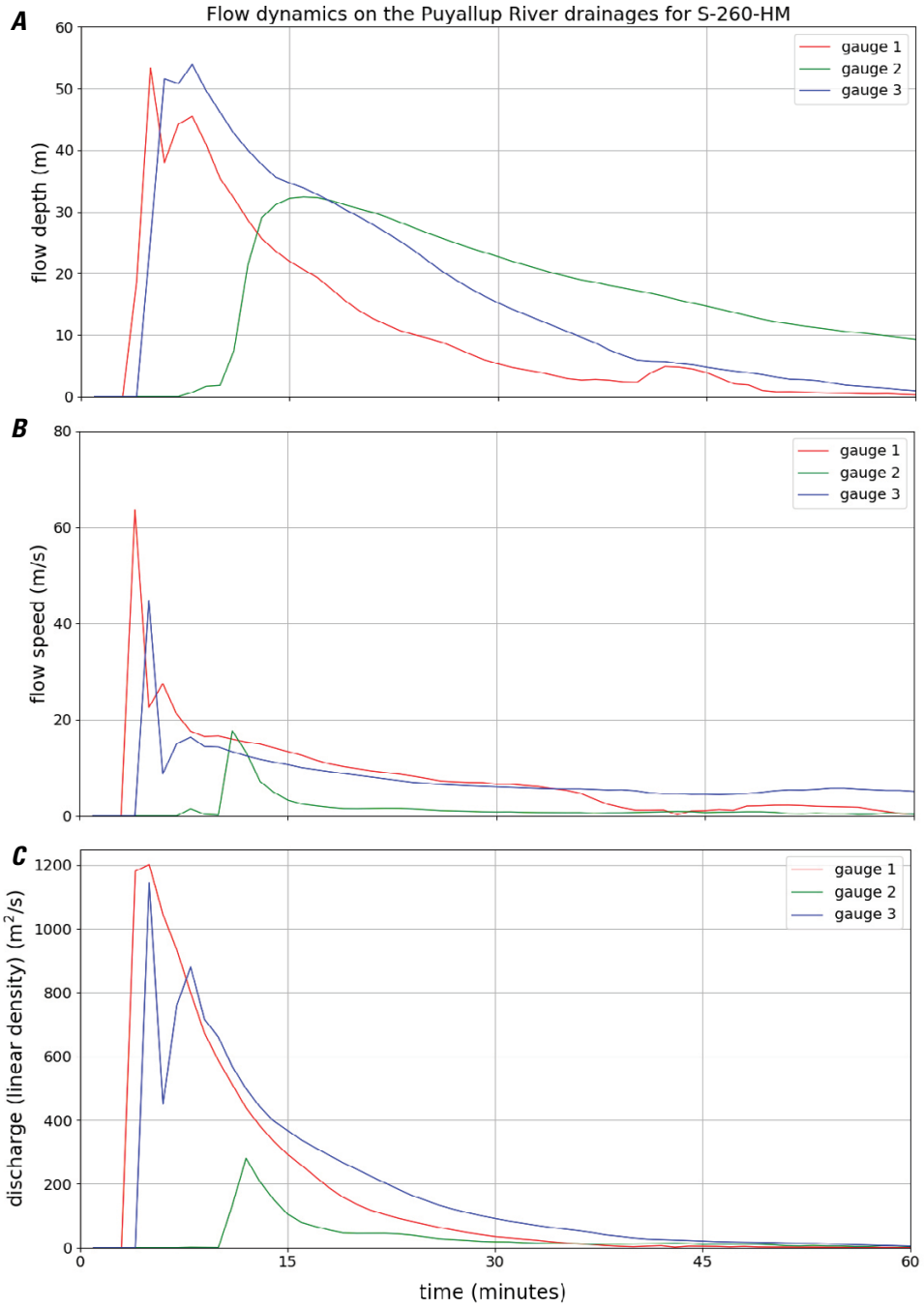

Figure 33. Graphs of time series output for the S-260-HM simulation showing the evolution of lahar flow dynamics at gauges 1–3 in the Puyallup River and Mowich River valleys. *A*, Flow depth, *h*, in meters (m). *B*, Flow speed, $||v||$, in meters per second (m/s). *C*, Discharge per unit valley width, $||hv||$, in square meters per second (m^2/s). The latter quantity ($||hv||$) is a point value or linear density (total discharge per unit width perpendicular to the local flow direction). Gauge locations are shown in figure 31.

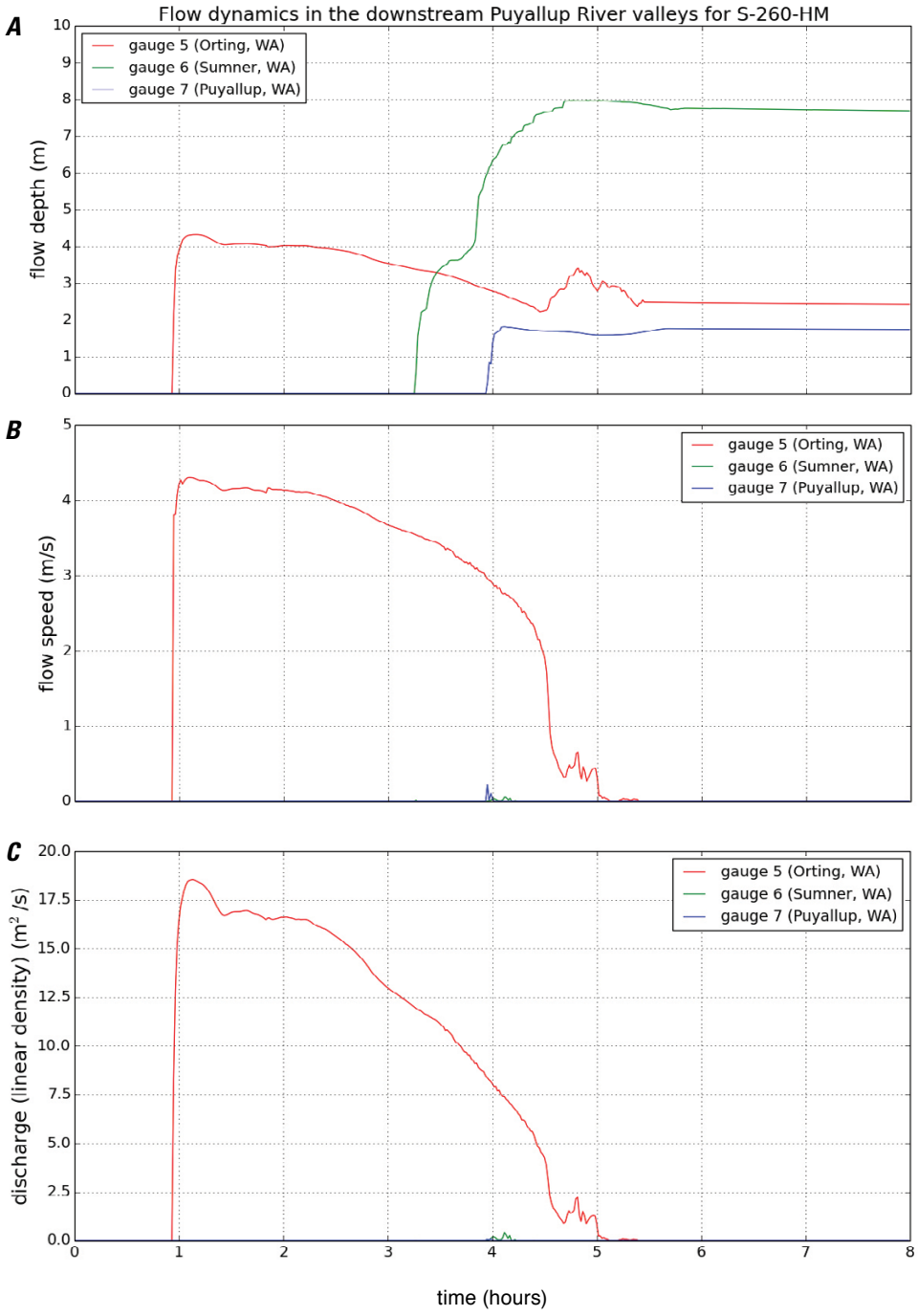

Figure 34. Graph of time series output for the S-260-HM simulation showing the evolution of lahar flow dynamics at gauges 5–7, located near the communities of Orting, Sumner, and Puyallup in the Puyallup River valley. *A*, Flow depth, h, in meters (m). *B*, Flow speed, $||v||$, in meters per second (m/s). *C*, Discharge per unit valley width, $||hv||$, in square meters per second (m^2/s). The latter quantity ($||hv||$) is a point value or linear density (total discharge per unit width perpendicular to the local flow direction). Flow speeds and discharges at Sumner and Puyallup are small and nearly indiscernable. Gauge locations are shown in figure 31.

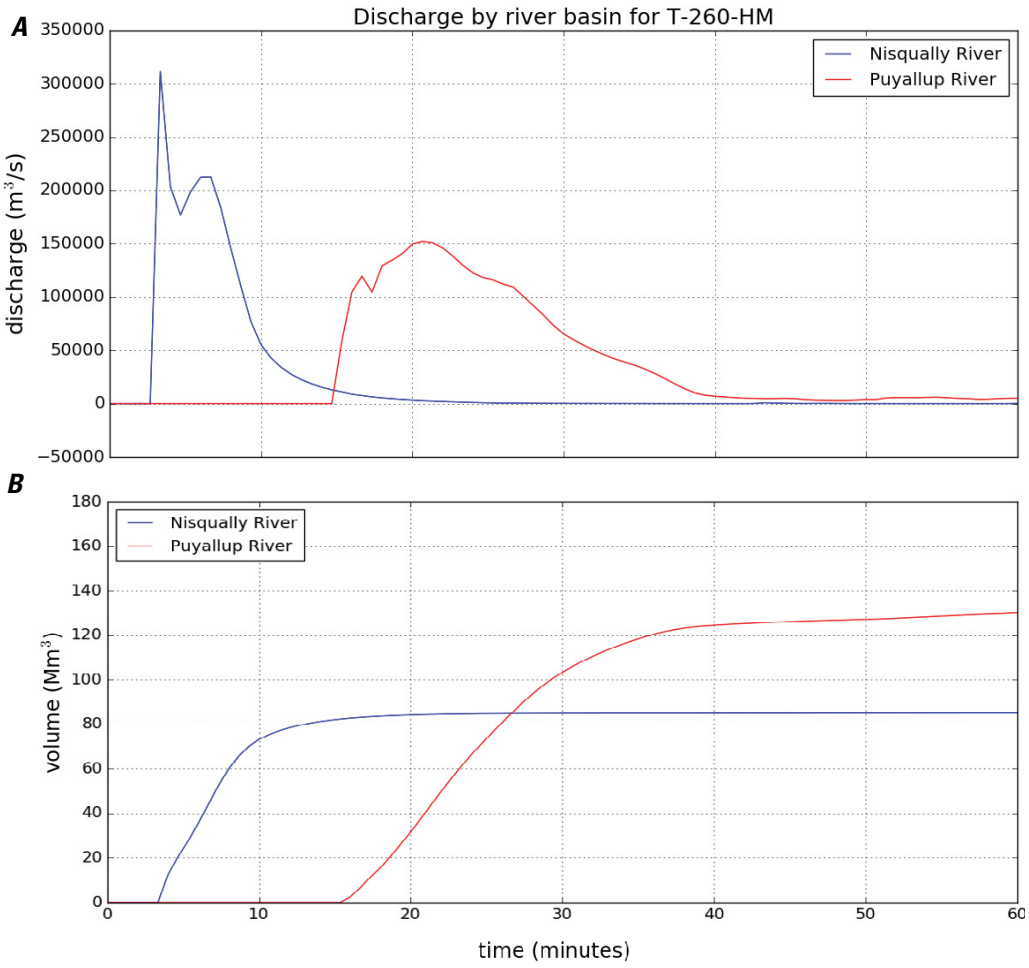

Figure 35. Graphs of time series output for the T-260-HM simulation lahar showing total flow discharge and total flow volume in the Puyallup and Nisqually River valleys. *A*, Total flow discharge (volume flux) in cubic meters per second (m^3/s) through transects Γ_{Puy} and Γ_{Nisq} (located along the Puyallup and Nisqually River valleys, respectively; see fig. 31). *B*, Cumulative (temporally integrated) discharge or total flow volume through the same transects. Mm^3, million cubic meters.

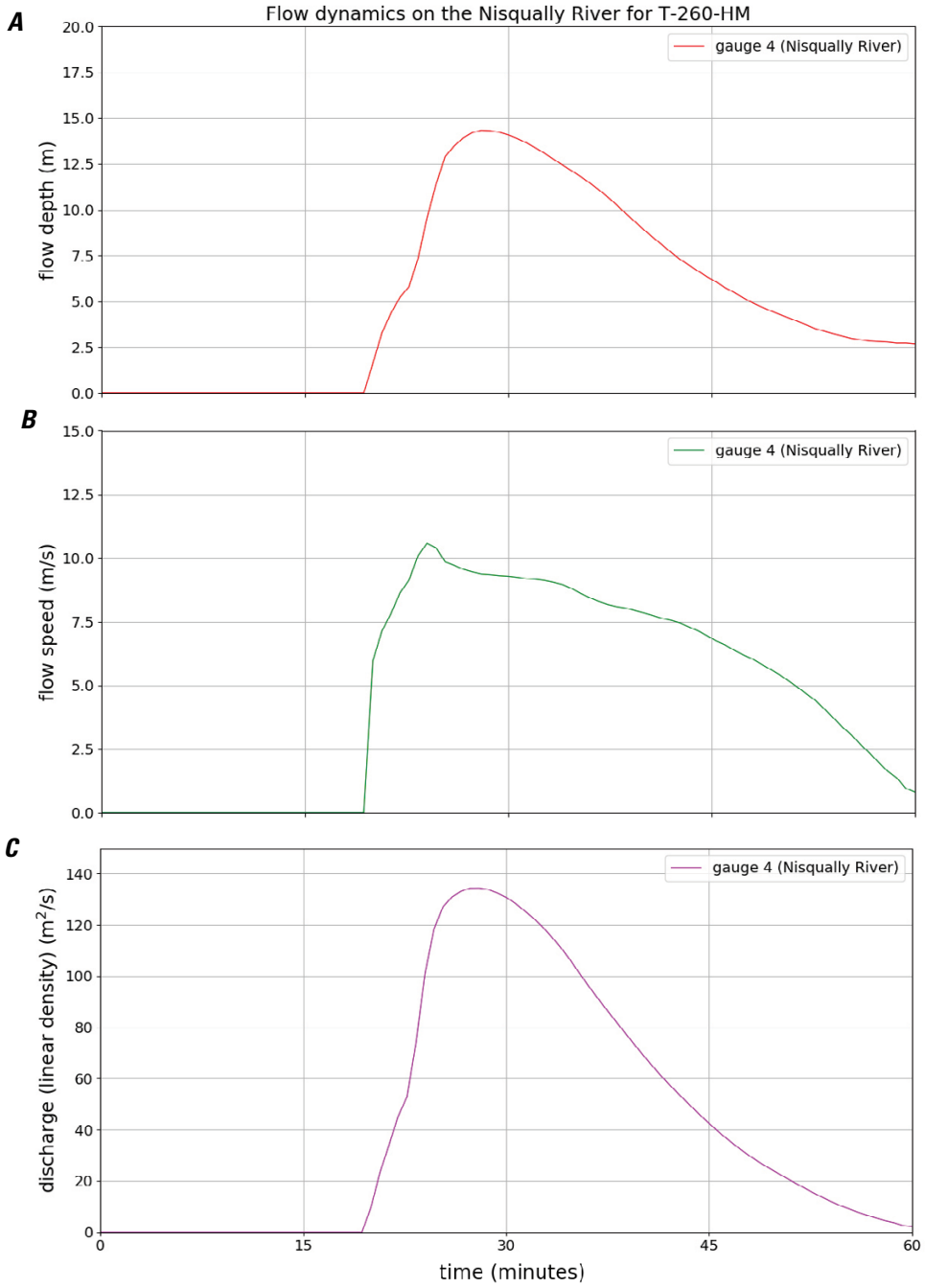

Figure 36. Graphs of time series output for the T-260-HM simulation showing the evolution of lahar flow dynamics at gauge 4, located on the Nisqually River upstream of Alder Lake, near Ashford. *A*, Flow depth, h, in meters (m). *B*, Flow speed, $||v||$, in meters per second (m/s). *C*, Discharge per unit valley width, $||hv||$, in square meters per second (m^2/s). The latter quantity ($||hv||$) is a point value or linear density (total discharge per unit width perpendicular to the local flow direction). Gauge 4 location is shown in figure 31.

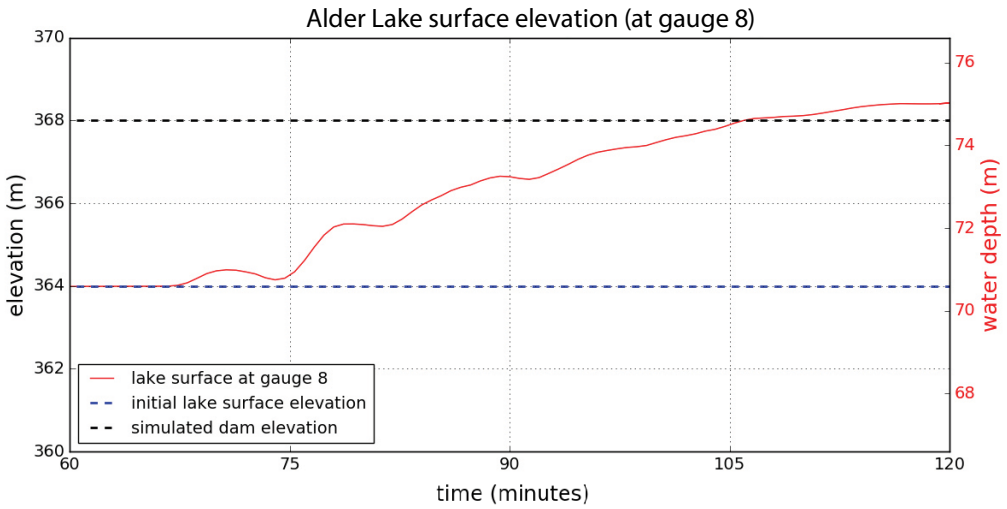

Figure 37. Graph of time series output for the T-260-HM simulation showing the water surface elevation in meters (m) at gauge 8, located in Alder Lake just upstream from Alder Dam. The rising lake surface exceeds the elevation of the simulated dam after time $t \approx 105$ minutes. The simulated lake surface elevation and simulated dam crest elevation were 364 m and about 368 m, respectively.

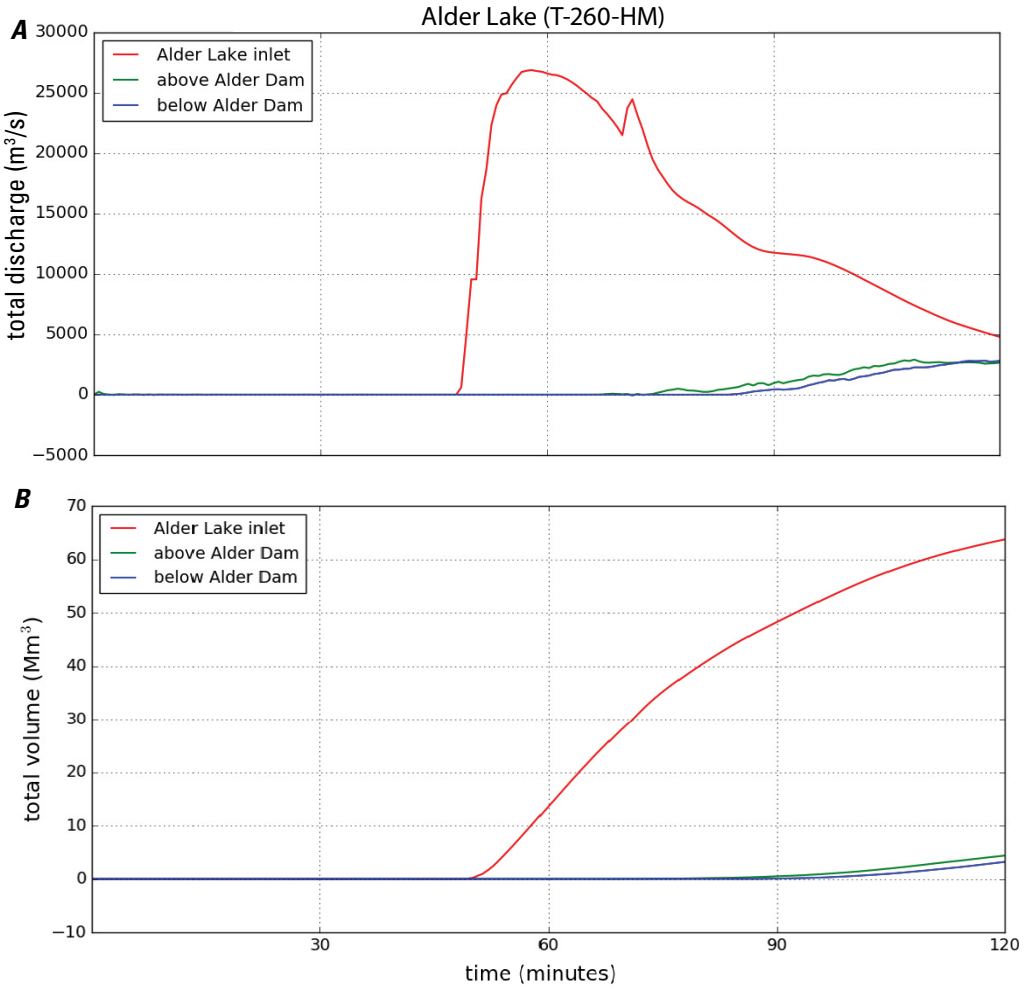

Figure 38. Graphs of time series output for the T-260-HM simulation lahar comparing the total discharge and total volume of flow through transect Γ_{Alder} at the head (inlet) of Alder Lake to the total discharge and total volume of flow through transects $\Gamma_{AboveDam}$ and $\Gamma_{BelowDam}$, located just above and below Alder Dam. *A*, Total flow discharge (volume flux) in cubic meters per second (m^3/s) through transects Γ_{Alder}, $\Gamma_{AboveDam}$, and $\Gamma_{BelowDam}$ (for transect locations, see fig. 31, tables 4 and 5). *B*, Cumulative (temporally integrated) discharge or total flow volume through the same transects. The total volume discrepancy represents the reserve capacity of the lake given the assumed initial lake surface elevation and our model representation of the dam. At time t=120 minutes, the lake approaches a steady mass balance between inflow and outflow, marking the end of the simulation. Mm^3, million cubic meters.

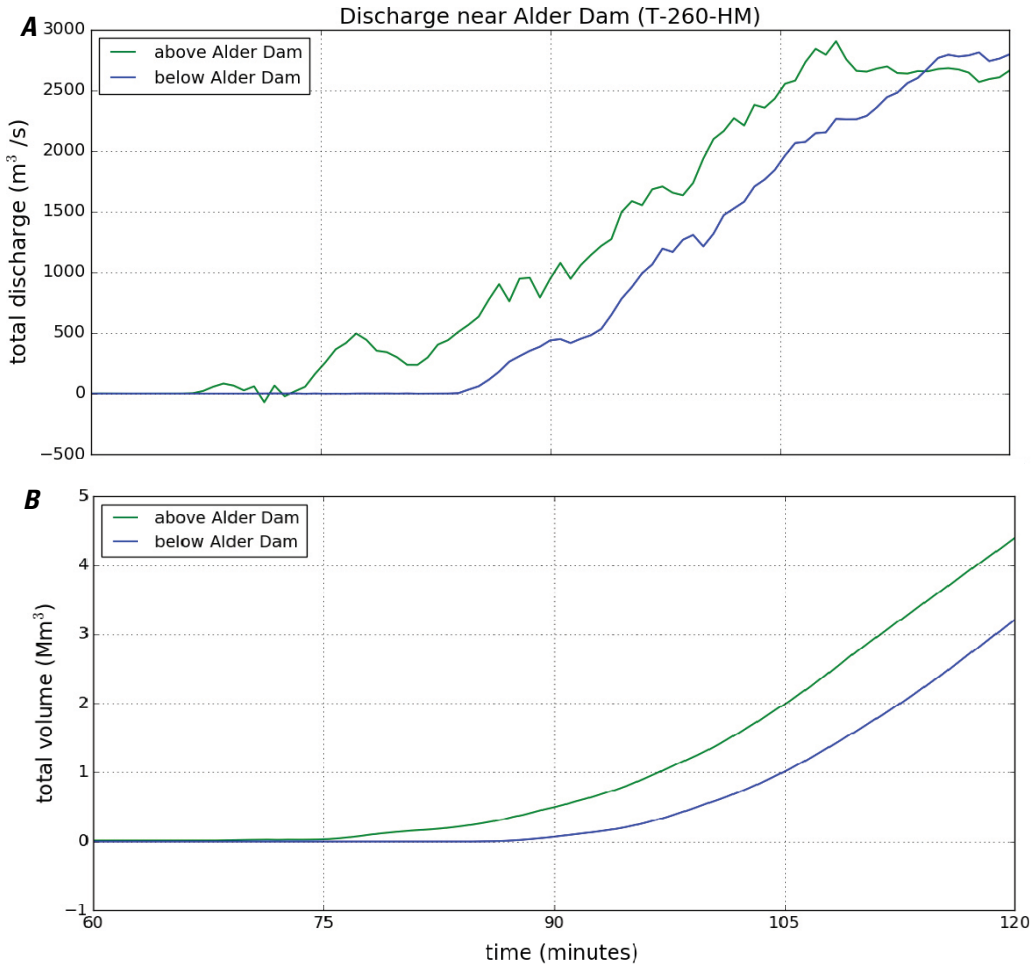

Figure 39. Graphs of time series output for the T-260-HM simulation lahar showing total flow discharge and total flow volume above and below Alder Dam. *A*, Total flow discharge (volume flux) in cubic meters per second (m^3/s) through transects $\Gamma_{AboveDam}$ and $\Gamma_{BelowDam}$ (see tables 4 and 5). *B*, Cumulative (temporally integrated) discharge or total flow volume through the same transects. Mm^3, million cubic meters.

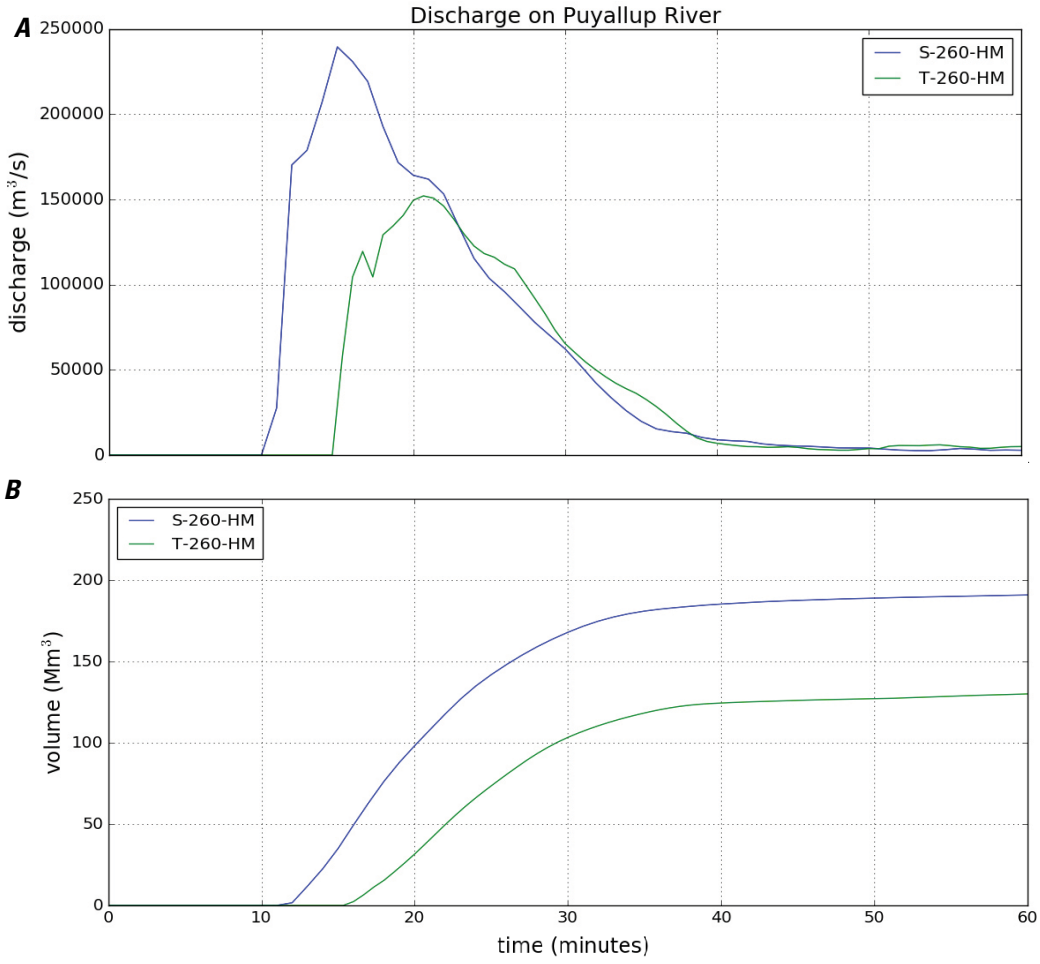

Figure 40. Graphs of time series output for the two worst-case scenario simulations T-260-HM and S-260-HM showing total flow discharge and total flow volume of the simulated lahars in the Puyallup River valley at gauge 3. *A*, Total flow discharge (volume flux) in cubic meters per second (m^3/s) at gauge 3 (see fig. 31). *B*, Cumulative (temporally integrated) discharge or total flow volume at gauge 3. Mm^3, million cubic meters.

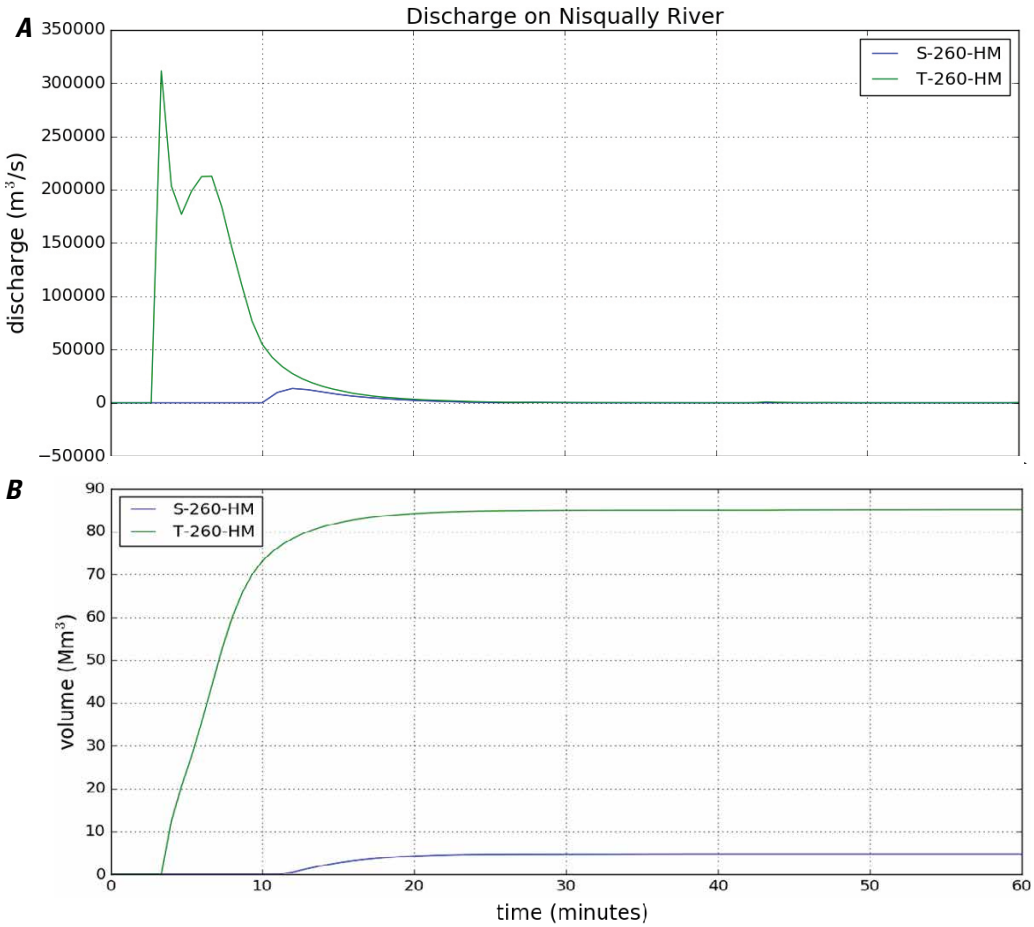

Figure 41. Graphs of time series output for the two worst-case scenario simulations T-260-HM and S-260-HM showing total flow discharge and total flow volume of the simulated lahars in the Nisqually River valley at gauge 4. *A*, Total flow discharge (volume flux) in cubic meters per second (m^3/s) at gauge 4 (see fig. 31). *B*, Cumulative (temporally integrated) discharge or total flow volume at gauge 4. Mm^3, million cubic meters.

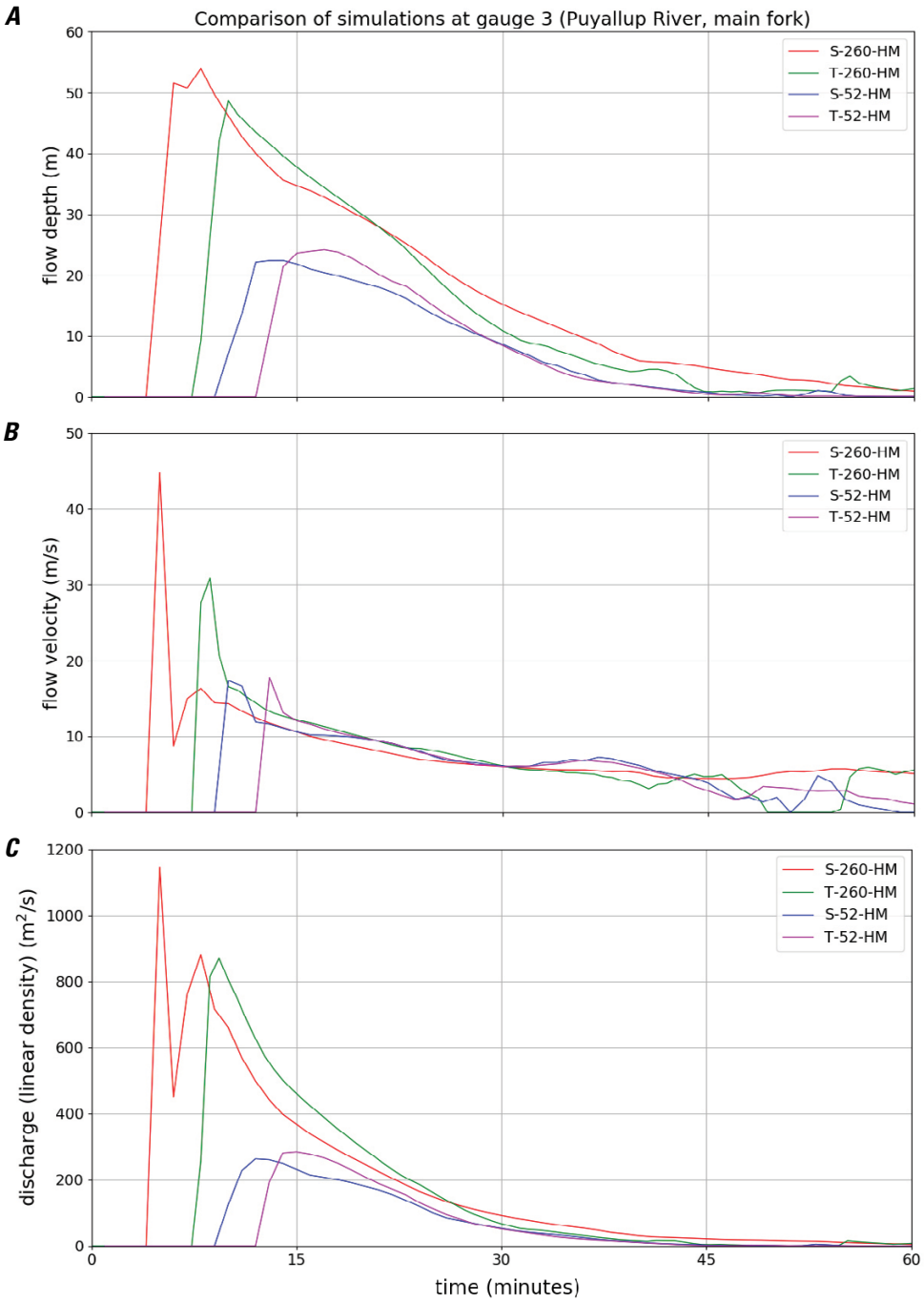

Figure 42. Graphs of time series output for the four high-mobility (HM) lahar simulations showing comparisons of lahar flow dynamics at gauge 3 on the Puyallup River. *A*, Flow depth, h, in meters (m). *B*, Flow speed, $||v||$, in meters per second (m/s). *C*, Discharge per unit valley width, $||hv||$, in square meters per second (m^2/s). The latter quantity ($||hv||$) is a point value or linear density (total discharge per unit width perpendicular to the local flow direction). All high-mobility lahar simulations produce substantial lahar flows at this location. The larger (260 million cubic meter) high-mobility lahars produce the largest and fastest flows. Gauge 3 location is shown in figure 31.

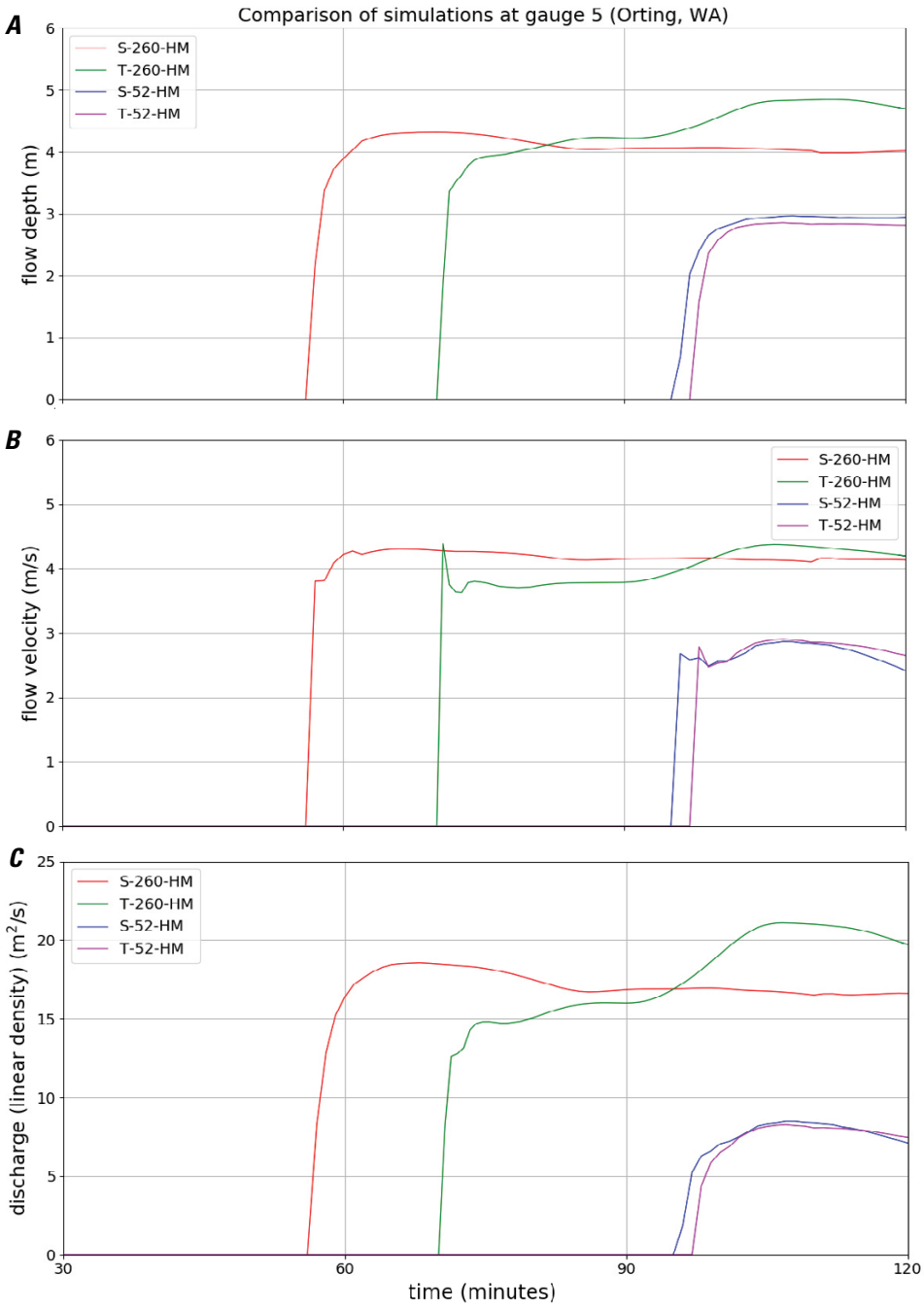

Figure 43. Graphs of time series output for the four high-mobility (HM) lahar simulations showing comparisons of lahar flow dynamics at gauge 5 near Orting. *A*, Flow depth, *h*, in meters (m). *B*, Flow speed, $||v||$, in meters per second (m/s). *C*, Discharge per unit valley width, $||hv||$, in square meters per second (m^2/s). The latter quantity ($||hv||$) is a point value or linear density (total discharge per unit width perpendicular to the local flow direction). All simulated high-mobility lahars produce substantial inundation at gauge 5. The smaller (52 million cubic meter) lahars arrive notably later (~100 minutes after slope failure vs. ~50 minutes for large volume lahars) and produce smaller inundation depths. Gauge 5 location is shown in figure 31.

Discussion

The geologic record of past lahars originating on the west side of Mount Rainier provides important information about the scope of hazards posed by potential future lahars. However, the information is incomplete because of the limited number of past lahars, imperfect geologic preservation and exposure of their deposits, and an absence of real-time observations. Our numerical simulations of potential lahars originating on the west side of Mount Rainier are not intended to reproduce the behavior of specific past events but rather to expand the knowledge base for anticipating the behavior of a wide range of future events. In particular, the simulations provide information about potential lahar speeds, depths, and inundation limits, which depend on the initial landslide volume, source-area location, and material properties that influence lahar mobility.

In the simulations described herein, each of the high-mobility (HM) lahars (S-260-HM, S-52-HM, T-260-HM, and T-52-HM) led to substantial inundation along the Puyallup River valley and in the community of Orting. None of the low-mobility (LM) lahars (S-260-LM, S-52-LM, T-260-LM, and T-52-LM), which differed from the high-mobility lahars only in the value of their initial hydraulic permeability (table 1), led to substantial lahar inundation far downstream from the steep slopes of Mount Rainier. Additionally, because the hydraulic permeability ultimately affects the time scale of pore-pressure relaxation (see for example, George and Iverson, 2014; Iverson and George, 2014, 2016), and has less of an influence on the initial degree of liquefaction, mobility during the early stages of motion is not always a robust predictor of downstream mobility and ultimate inundation extent. These findings imply that the composition of lahar material may be as important as the initial landslide volume, location, and upstream dynamics for assessing downstream effects. Therefore, reducing uncertainties about subsurface rock and sediment properties that affect lahar mobility is of critical importance for refining hazard assessments.

As noted previously, confidence in the accuracy of our simulation results decreases with flow duration and distance from the initial source location because of compounding effects of multiple uncertainties. Furthermore, model results are more prone to error in low-gradient terrain where topographic forcing is less dominant and frictional resistance (which increases as pore-fluid pressure decreases) exerts more influence on spreading rates and inundation limits. Our simulations do not account for possible effects of pre-event river water or loss of lahar fluid into permeable substrates, and they omit the effects of erosional and depositional processes (particle entrainment or settling). These model limitations further elevate uncertainties in predictions of the downstream reaches of the lahars. Thus, the results for the S-260-HM scenario should be viewed with a degree of skepticism that increases with distance downstream from Orting.

Although the worst-case lahar scenarios presented in this study produce inundation limits that extend somewhat farther downstream along the Puyallup River valley than do the documented deposits from the prehistoric Electron Mudflow, the high mobilities of the lahars in these scenarios were intentionally chosen to provide estimates of worst-case scenario inundation limits for lahars with specified volumes. Their mobilities are realistic for some historical lahars that have occurred elsewhere.

The T-260-HM scenario predicted inundation and displacement of reservoir water in Alder Lake that caused considerable overtopping of Alder Dam. However, this result may be particularly sensitive to lahar mobility and should be interpreted in the context of uncertainties and seasonal variability in the water depth above Alder Dam. Even slightly reduced mobility of a similar lahar might cause it to deposit more material above the head of the reservoir, leading to little if any dam overtopping. Documented geological evidence of prehistoric lahar deposits downstream from the location of the current reservoir is lacking (Scott and others, 1995; Vallance and Scott, 1997; and Sisson and Vallance, 2009).

Final Remarks

This report presents and analyzes results generated by a depth-averaged numerical model (D-Claw) for eight hypothetical lahar scenarios on the west side of Mount Rainier. The simulated lahars begin as landslides high on the volcano's west side, and they originate from two distinct landslide source areas. For each source area the simulations consider two landslide volumes and landslide material with two hydraulic permeabilities. The differing permeabilities lead to differing lahar mobilities and consequently to differing inundation speeds and patterns as the simulated lahars descend the river valleys below. These scenarios are designed to characterize potential lahar hazards that can result from volcano edifice collapses even in the absence of eruptive activity or precursory indications of slope failures. However, these scenarios could apply to similarly sized lahars occurring during volcanic eruptions or precursory volcanic unrest as well.

Although our simulations are informed by the geologic record of lahars and by investigations of slope stability on the west side of Mount Rainier, the modeled scenarios are not predictions of anticipated events. Nevertheless, the simulations provide some quantitative indication of downstream inundation extents and travel times if such landslides were to occur. Furthermore, animations of the simulations (available at https://doi.org/10.3133/ofr20211118) illustrate some key qualitative aspects of lahar behavior.

The landslide material properties used in our simulations are constrained within reasonable bounds based on other landslide studies and experimental tests (for example, Iverson and others, 2010, 2015; Iverson and George, 2016), but they are not constrained by site-specific studies at Mount Rainier. The material properties used in the simulations lead to relatively mobile landslides that are prone to liquefaction as downslope motion begins, and the properties used in the high-mobility (HM) simulations cause liquefaction to persist

as lahars travel farther downstream. In low-mobility (LM) simulations, however, the initial liquefaction does not persist, and the consequent downstream flows do not travel far enough to enter highly populated lowland areas. The behavior of these low-mobility flows is similar to that of many volcanic debris avalanches.

Modeling physically complex events such as landslides and lahars involves a large degree of uncertainty and potential error. Quantification of relevant uncertainty and error remains challenging owing to a paucity of relevant data, and it is beyond the scope of this report. Model verification and validation of D-Claw is ongoing and is not addressed in this report. Results that address D-Claw model verification and validation can be found in previous reports by Iverson and George (2014), George and Iverson (2014), Iverson and others (2015), Iverson and George (2016), Iverson and others (2016), and George and others (2017).

Acknowledgments

We thank James Vallance and William Scott (USGS) for their technical reviews, which helped improve this document. Their scientific knowledge, judgement, and advice were valuable resources and are greatly appreciated. We also thank Tami Christianson (USGS) for her expertise and assistance in the field, which was instrumental in the preparation of digital elevation models used in this study.

References Cited

Allstadt, K., 2013, Extracting source characteristics and dynamics of the August 2010 Mount Meager landslide from broadband seismograms: Journal of Geophysical Research, v. 118, no. 3, p. 1472–1490, https://doi.org/10.1002/jgrf.20110.

Berger, M.J., and Colella, P., 1989, Local adaptive mesh refinement for shock hydrodynamics: Journal of Computational Physics, v. 82, no. 1, p. 64–84, https://doi.org/10.1016/0021-9991(89)90035-1.

Berger, M.J., and Oliger, J., 1984, Adaptive mesh refinement for hyperbolic partial differential equations: Journal of Computational Physics, v. 53, no. 3, p. 484–512, https://doi.org/10.1016/0021-9991(84)90073-1.

Berger, M.J., George, D.L., LeVeque, R.J., and Mandli, K.T., 2011, The GeoClaw software for depth-averaged flows with adaptive refinement: Advances in Water Resources, v. 34, no. 9, p. 1195–1206, https://doi.org/10.1016/j.advwatres.2011.02.016.

Crandell, D.R., and Waldron, H.H., 1956, A recent volcanic mudflow of exceptional dimensions from Mount Rainier, Washington: American Journal of Science, v. 254, p. 349–362, https://doi.org/10.2475/ajs.254.6.349.

Crandell, D.R., 1971, Postglacial lahars from Mount Rainier volcano, Washington: U.S. Geological Survey Professional Paper 677, 75 p., https://doi.org/10.3133/pp677.

Czuba, J.A., Olsen, T.D., Czuba, C.R., Magirl, C.S., and Gish, C.C., 2012, Changes in sediment volume in Alder Lake, Nisqually River Basin, Washington, 1945–2011: U.S. Geological Survey Open-File Report 2012–1068, 30 p., https://doi.org/10.3133/ofr20121068.

Finn, C.A., Sisson, T.W., and Deszcz-Pan, M., 2001, Aerogeophysical measurements of collapse-prone hydrothermally altered zones at Mount Rainier volcano: Nature, v. 409, p. 600–609, https://doi.org/10.1038/35054533.

George, D.L., 2006, Finite volume methods and adaptive refinement for tsunami propagation and inundation: Seattle, University of Washington, Ph.D. dissertation, 167 p.

George, D.L., 2008, Augmented Riemann solvers for the shallow water equations over variable topography with steady states and inundation: Journal of Computational Physics, v. 227, no. 6, p. 3089–3113, https://doi.org/10.1016/j.jcp.2007.10.027.

George, D.L., 2011, Adaptive finite volume methods with well-balanced Riemann solvers for modeling floods in rugged terrain—Application to the Malpasset dam-break flood (France, 1959): International Journal for Numerical Methods in Fluids, v. 66, no. 8, p. 1000–1018, https://doi.org/10.1002/fld.2298.

George, D.L. and Iverson, R.M., 2014, A depth-averaged debris-flow model that includes the effects of evolving dilatancy—II. Numerical predictions and experimental tests: Proceedings of the Royal Society A, v. 470, no. 2170, 31 p., https://doi.org/10.1098/rspa.2013.0820.

George, D.L., Iverson, R.M., and Cannon, C.M., 2017, New methodology for computing tsunami generation by subaerial landslides—Application to the 2015 Tyndall Glacier landslide, Alaska: Geophysical Research Letters, v. 44, no. 14, p. 7276–7284, https://doi.org/10.1002/2017GL074341.

Guthrie, R.H., Friele, P., Allstadt, K., Roberts, N., Evans, S.G., Delaney, K.B., Roche, D., and Clague, J.J., 2012, The 6 August 2010 Mount Meager rock slide-debris flow, Coast Mountains, British Columbia—Characteristics, dynamics, and implications for hazard and risk assessment: Natural Hazards and Earth System Sciences, v. 12, no. 5, p. 1277–1294, https://doi.org/10.5194/nhess-12-1277-2012.

Hoblitt, R.P., Walder, J.S., Driedger, C.L., Scott, K.M., Pringle, P.T., and Vallance, J.W., 1998, Volcano hazards from Mount Rainier, Washington, revised 1998: U.S. Geological Survey Open-File Report 98–428, 11 p., https://doi.org/10.3133/ofr98428.

Iverson, R.M., and George, D.L., 2014, A depth-averaged debris-flow model that includes the effects of evolving dilatancy—I. Physical basis: Proceedings of the Royal Society A, v. 470, no. 2170, 31 p., https://doi.org/10.1098/rspa.2013.0819.

Iverson, R.M., and George, D.L., 2016, Modelling landslide liquefaction, mobility bifurcation and the dynamics of the 2014 Oso disaster: Geotechnique, v. 66, no. 3, p. 175–187, https://doi.org/10.1680/jgeot.15.LM.004.

Iverson, R.M., George, D.L., Allstadt, K., Reid, M.E., Collins, B.D., Vallance, J.W., Schilling, S.P., Godt, J.W., Cannon, C.M., Magirl, C.S., Baum, R.L., Coe, J.A., Schulz, W.H., and Bower, J.B., 2015, Landslide mobility and hazards—Implications of the 2014 Oso disaster: Earth and Planetary Science Letters, v. 412, p. 197–208, https://doi.org/10.1016/j.epsl.2014.12.020.

Iverson, R.M., Logan, M., LaHusen, R.G., and Berti, M., 2010, The perfect debris flow?—Aggregated results from 28 large-scale experiments: Journal of Geophysical Research Earth Surface, v. 115, no. F3, article F03005, 29 p., https://doi.org/10.1029/2009JF001514.

Iverson, R.M., Schilling, S.P., and Vallance, J.W., 1998, Objective delineation of lahar-inundation hazard zones: Geological Society of America Bulletin, v. 110, no. 8, p. 972–984, https://doi.org/10.1130/0016-7606(1998)110%3C0972:ODOLIH%3E2.3.CO;2.

Iverson, R.M., George, D.L., and Logan, M., 2016, Debris flow runup on vertical barriers and adverse slopes: Journal of Geophysical Research Earth Surface, v. 121, no. 12, p. 2333–2357, https://doi.org/10.1002/2016JF003933.

Jaboyedoff, M., Carrea, D., Derron, M.H., Oppikofer, T., Penna, I.M., and Rudaz, B., 2020, A review of methods used to estimate initial landslide failure surface depths and volumes: Engineering Geology, v. 267, article 105478, 18 p., https://doi.org/10.1016/j.enggeo.2020.105478.

Jefferies, M., and Been, K., 2016, Soil liquefaction—A critical state approach (2d ed.): Boca Raton, Fla., CRC Press, 712 p.

LeVeque, R.J., 2002, Finite volume methods for hyperbolic problems: Cambridge Texts in Applied Mathematics, v. 31, 558 p., https://doi.org/10.1017/CBO9780511791253.

LeVeque, R.J., George, D.L., and Berger, M.J., 2011, Tsunami modelling with adaptively refined finite volume methods: Acta Numerica, v. 20, p. 211–289, https://doi.org/10.1017/S0962492911000043.

Major, J.J., Iverson, R.M., McTigue, D.F., Macias, S., and Fiedorowicz, B.K., 1997, Geotechnical properties of debris-flow sediments and slurries, in Chen, Cheng-lung, ed., Debris-flow hazards mitigation—Mechanics, prediction, and assessment—Proceedings of First International Conference, San Francisco, Calif., August 7–9, 1997: New York, American Society of Civil Engineers, p. 249–259.

Mandli, K.T., Ahmadia, A.J., Berger, M.J., Calhoun, D., George, D.L., Hadjimichael, Y., Ketcheson, D.I., Lemoine, G.I., and LeVeque, R.J., 2016, Clawpack—Building an open source ecosystem for solving hyperbolic PDEs: PeerJ Computer Science, v. 2, 27 p., https://doi.org/10.7717/peerj-cs.68.

Moretti, L., Allstadt, K., Mangeney, A., Capdeville, Y., Stutzmann, E., and Bouchut, F., 2015, Numerical modeling of the Mount Meager landslide constrained by its force history derived from seismic data: Journal of Geophysical Research Solid Earth, v. 120, no. 4, p. 2579–2599, https://doi.org/10.1002/2014JB011426.

Pierson, T.C., and Scott, K.M., 1985, Downstream dilution of a lahar—Transition from debris flow to hyperconcentrated streamflow: Water Resources Research, v. 21, no. 10, p. 1511–1524, https://doi.org/10.1029/WR021i010p01511.

Reid, M.E., Christian, S.B., Brien, D.L., and Henderson, S.T., 2015, Scoops3D—Software to analyze 3D slope stability throughout a digital landscape: U.S. Geological Survey Techniques and Methods, book 14, chap. A1, 218 p., https://doi.org/10.3133/tm14A1.

Reid, M.E., Sisson, T.W., and Brien, D.L., 2001, Volcano collapse promoted by hydrothermal alteration and edifice shape, Mount Rainer, Washington: Geology, v. 29, no. 9, p. 779–782, https://doi.org/10.1130/0091-7613(2001)029%3C0779:VCPBHA%3E2.0.CO;2.

Roberti, G., Friele, P., van Wyk de Vries, B., Ward, B., Clague, J.J., Perotti, L., and Giardino, M., 2017, Rheological evolution of the Mount Meager 2010 debris avalanche, southwestern British Columbia: Geosphere, v. 13, no. 2, p. 369–390, https://doi.org/10.1130/GES01389.1.

Schilling, S.P., 1998, LAHARZ—GIS programs for automated mapping of lahar-inundation hazard zones: U.S. Geological Survey Open-File Report 98-638, 80 p., https://doi.org/10.3133/ofr98638.

Scott, K.M., Vallance, J.W., and Pringle, P.T., 1995, Sedimentology, behavior, and hazards of debris flows at Mount Rainier, Washington: U.S. Geological Survey Professional Paper 1547, 56 p., https://doi.org/10.3133/pp1547.

Sisson, T.W., and Vallance, J.W., 2009, Frequent eruptions of Mount Rainier over the last ~2,600 years: Bulletin of Volcanology, v. 71, p. 595–618, https://doi.org/10.1007/s00445-008-0245-7.

Vallance, J.W., and Scott, K.M., 1997, The Osceola Mudflow from Mount Rainier—Sedimentology and hazard implications of a huge clay-rich debris flow: Geological Society of America Bulletin, v. 109, no. 2, p. 143–163, https://doi.org/10.1130/0016-7606(1997)109%3C0143:TOMFMR%3E2.3.CO;2.

Moffett Field Publishing Service Center, California
Manuscript approved for publication December 3, 2021
Edited by Tim Herold
Layout and design by Kimber Petersen

ISSN 2331-1258 (online)
https://doi.org/10.3133/ofr20211118